Star clusters in the Whirlpool Galaxy

Remco Scheepmaker

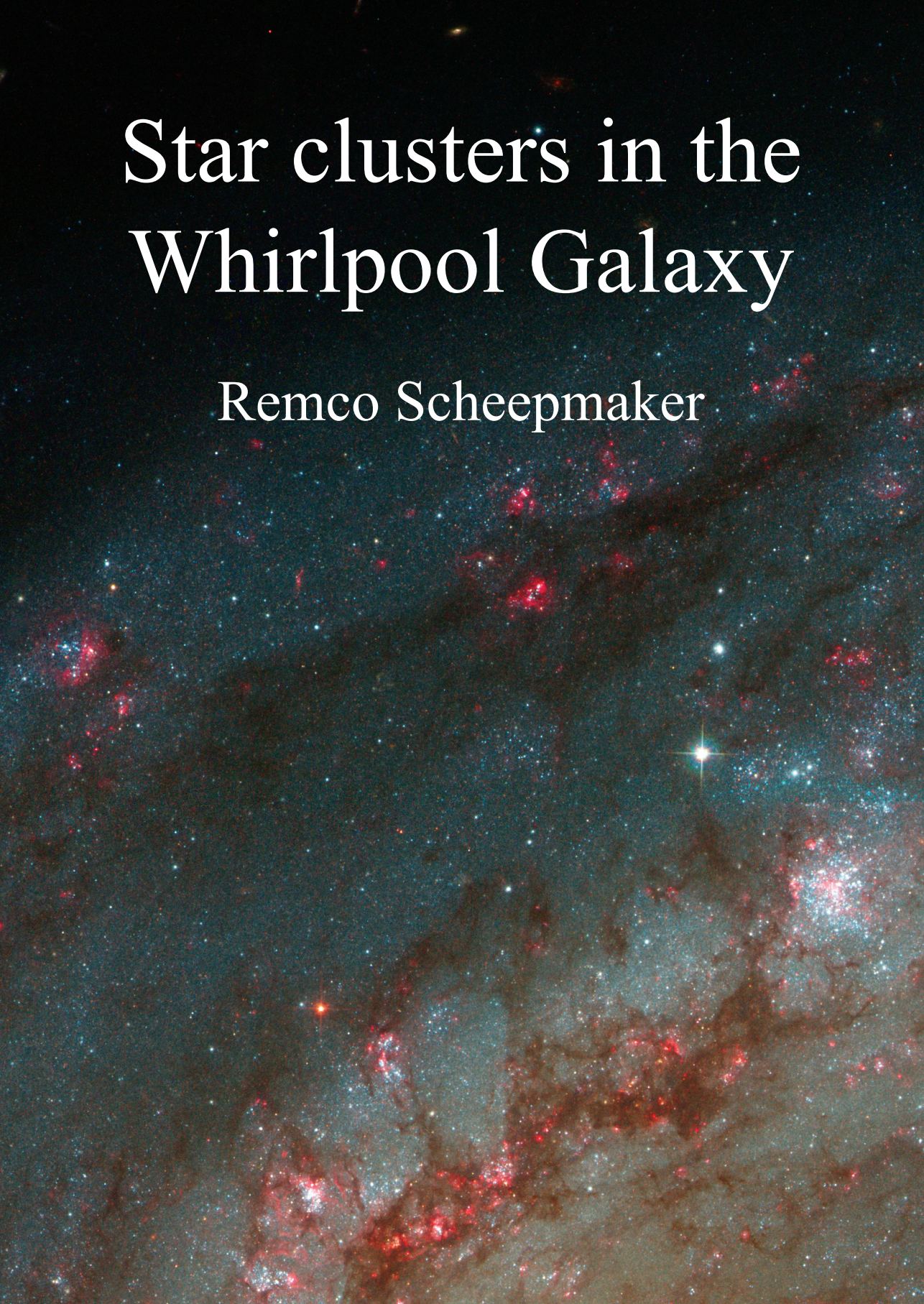

Star clusters in the Whirlpool Galaxy

ISBN 978-90-393-5072-0

Cover image: small part of the *HST/ACS* mosaic image of the Whirlpool Galaxy (NGC 5194 or M51). Most of the white-blue dots are young star clusters emerging from bubbles of hydrogen gas, which glow in pink. Image courtesy of NASA, ESA, S. Beckwith (STScI) and The Hubble Heritage Team (STScI/AURA).

Star clusters in the Whirlpool Galaxy

Sterrenhopen in de Draaikolknevel

(met een samenvatting in het Nederlands)

Proefschrift

ter verkrijging van de graad van doctor aan de Universiteit Utrecht op gezag van de rector magnificus, prof. dr. J. C. Stoof, ingevolge het besluit van het college voor promoties in het openbaar te verdedigen op dinsdag 16 juni 2009 des middags te 12.45 uur

door

Remco Alexander Scheepmaker

geboren op 4 oktober 1980 te Rijssen

Promotor: Prof. dr. H. J. G. L. M. Lamers

Co-promotor: Dr. S. S. Larsen

Contents

Chapter 1

Introduction

1.1 Star clusters as astrophysical tools

Star clusters are important tools in a wide variety of astrophysical research. As with many astrophysical tools they were first applied in our own astronomical backyard, the Milky Way. It was actually by virtue of star clusters that our current picture of the Milky Way began to take shape. Thanks to the work of Shapley (1918), who estimated the distances to nearly a hundred globular clusters, we began to realise the true extent of the Milky Way. Also, it became clear that the sun is not located close to its centre. Furthermore, the work on open clusters by Trumpler (1930) proved to be of great significance. Trumpler showed that stars in remote clusters appeared significantly fainter than expected based on their distance alone. This made us aware of the importance of interstellar extinction.

At a later stage, when star formation sites in the Milky Way could be studied in detail, it became clear that practically all star formation seems to occur in a clustered fashion. Star clusters are therefore excellent tracers of star formation. This is underlined by the fact that star formation occurs very rapidly. This means that all stars in a cluster have practically the same age, equal to the time elapsed since the star formation event.

The rapidity of star formation can be understood as a result of the short free-fall timescale of the giant molecular cloud (GMC) that forms the cluster. For a spherical cloud with an initial homogeneous density ρ_0, the free-fall time is roughly equal to $(G\rho_0)^{-1/2}$, where G is the gravitational constant. This means that for a typical GMC with $\rho_0 \approx 2 \times 10^{-22}$ g cm^{-3}, the free-fall time is about 5 Myr. All stars in a cluster will therefore have ages not more than a few Myr apart.

The picture, in which a single self-gravitating GMC collapses and forms a cluster in about a free-fall timescale, is very simplistic. However, it functions as a first

order approximation to get a feeling for the timescale of star formation. In reality, star formation is a very complex process in which not only self-gravity, but also turbulence and magnetic fields play an important role (see e.g. Mac Low & Klessen 2004, McKee & Ostriker 2007). Also, a GMC, which has a typical mass of $\sim 10^7\ M_\odot$, will form a complex of different star clusters and not just a single cluster. If a GMC (or the interstellar medium (ISM) in general) is controlled by turbulent motions, the velocity of the material at a given point in the cloud will fluctuate irregularly. The fact that turbulence is a key ingredient for star formation was realised when Larson (1981) observed that the internal velocity dispersion (σ) of GMCs scales with their radius (R) as $\sigma \propto R^{0.38}$. Such a power-law relation, as well as power-law relations for the mass and radius distributions of gas clouds, are expected when the motions in the gas clouds are controlled by turbulence (Elmegreen & Efremov 1997). For GMCs these relations are observed to hold from their largest scales ($\sim$ 1 kpc) down to their cores with radii of $\sim$ 0.1 pc (Elmegreen & Falgarone 1996). This also means that the ISM can be considered scale-free (sometimes referred to as hierarchical or fractal). This shows that turbulence is important to explain the observed structure of the ISM and the structural parameters of the GMCs, prior to their collapse and the formation of star clusters. It is still uncertain, however, if the amount of hierarchy, e.g. expressed in the *fractal dimension*, is universal throughout different galaxies.

The collapse of (part of) a GMC is triggered when the turbulent motions create overdensities, which become gravitationally unstable. Once the collapse of such an overdensity has begun, the resulting star formation occurs very fast and all stars in the cluster will form at about the same time. Also, the spatial distribution of the young star cluster population is expected to show the same amount of hierarchy as the fractal medium from which they formed. The general validity of this still needs to verified, however, especially whether it holds on all scales and in different galaxies.

Because all stars that make up a cluster formed from the same cloud of material, a star cluster can be considered a Simple Stellar Population (SSP), meaning a population of stars which have the same age and chemical composition (also known as metallicity). This makes star clusters ideal for testing and calibrating stellar evolution models. Such models are used to generate isochrones for stellar populations with a fixed age and metallicity, which can be compared directly with observations of the individual stars in a cluster. Furthermore, the high stellar density in a cluster increases the chance of exotic stellar interactions to happen. This attracts even more attention of stellar evolution modellers to star clusters.

All this attention proved useful, as in turn the isochrones from stellar evolution modelling were used to estimate ages and distances of more and more clusters in the Milky Way. This was done using a technique called "CMD fitting", in which CMD is short for *Colour-Magnitude Diagram*. As an illustration of such a CMD fit we show in Fig. 1.1 an image of the most famous star cluster in the Milky Way, M45 or the Pleiades. In Fig. 1.2 we show its corresponding CMD, together with an isochrone from the Padova stellar evolution group (Girardi et al. 2002), assuming solar metallicity (i.e. $Z = 0.019$). The isochrone for an age of 126 Myr fits the bend or "turn-off point" at the top of the diagonal main sequence of stars. The main sequence

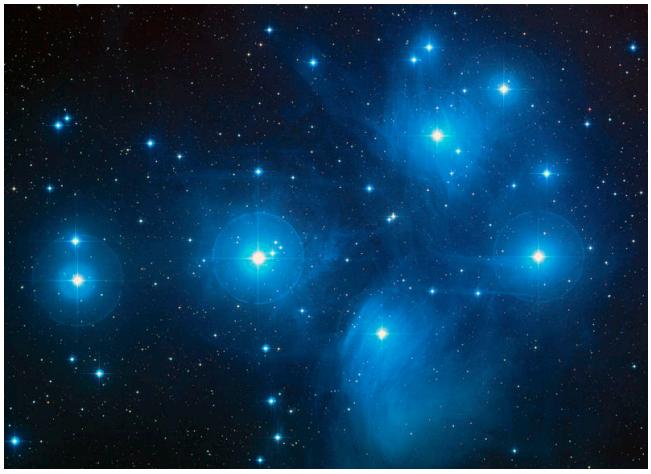

Figure 1.1: Image of M45, the most famous star cluster in the Milky Way and also known as the Pleiades. The colour version of this image can be found on page 126. Image courtesy of NASA/ESA/AURA/Caltech.

itself is only fitted after we have shifted down the isochrone by 5.65 mag, which is the distance modulus corresponding to a distance of 135 pc. This technique has been applied to many star clusters in the Milky Way, and resulted in a better picture of the Milky Way's dimensions and star formation history.

Consequently, star clusters were an important factor in improving our understanding of the structure and age of our own galaxy. Today, star clusters are playing a similar role in our understanding of the structure and ages of other galaxies, because they can now be used as chronometers in the evolution of other galaxies. This results from the fact that important epochs in the lifes of galaxies are traced by star formation, and thus by the age distribution of star cluster systems.

Thanks to the rise of space-based observatories such as the *Hubble Space Telescope* (*HST*) with its superb resolution, we can now observe star clusters in many other galaxies in a systematic way. Since galaxies are in some respects the building blocks of the universe, star clusters bridge a tremendous part of astronomy, from understanding single stars to understanding the entire universe.

Star clusters trace *when* star formation was occurring in galaxies, but for a complete picture we also need to know *exactly how much* star formation occurs in clusters. This is not straightforward, as star clusters are not static entities, but they evolve.

1.2 The evolution of star clusters

The evolution of star clusters is characterised by roughly three different phases. Although the physical processes involved occur in all three phases, the dominant

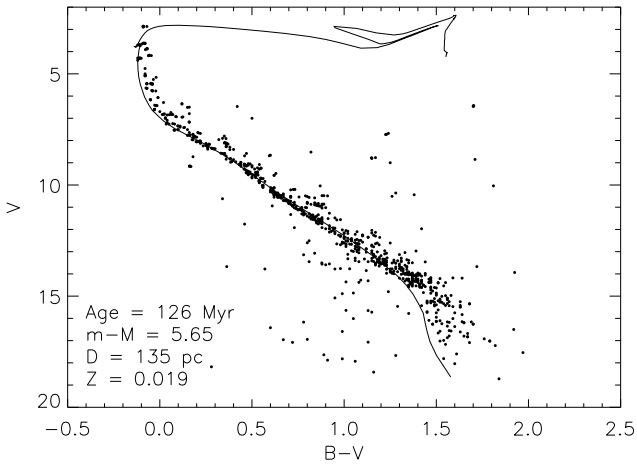

Figure 1.2: Colour-magnitude diagram of the Pleiades. The solid line is an isochrone from the Padova stellar evolution group for an age of 126 Myr, a distance modulus of 5.65 mag (corresponding to a distance of 135 pc) and solar metallicity.

process differs in each phase. During their evolution star clusters lose gas and stars, in different amounts and on different timescales during each phase.

The first phase is the time immediately following the formation of the clusters. This phase is dominated by violent relaxation and can last up to ~50 Myr (Goodwin & Bastian 2006, Parmentier & Fritze 2008). Violent relaxation is the dynamical response of the cluster after it emerges from its natal gas cloud. This is an important process, since it will lead to the majority of field stars that constitute the stellar populations of galaxies. In this phase most of the clusters become unbound. This first phase is also the least understood one, and will be an important aspect of this thesis. We will therefore treat it in more depth in the next section.

The second phase in the evolution of star clusters is dominated by stellar evolution. Because of stellar evolution the luminosity of the clusters will decrease with age. The clusters will slowly lose mass as the stars will first blow their winds and eventually their remaining material out of the cluster. Due to the important input that observations of Galactic star clusters have had on the development of stellar evolution models, this phase is now generally understood. Some open questions remain, however, mainly caused by the ubiquitous blue straggler population (see e.g. Xin et al. 2008) and by the latest phases in the evolution of stars, such as the red giant branch (RGB) and asymptotic giant branch (AGB) phases. Since these phases last relatively short in the lifetimes of stars, not that many stars in a star cluster occupy the corresponding regions in the CMD. Calibrating and testing the models of these evolutionary phases using star clusters therefore results in poor statistics and large uncertainties. The high instrinsic brightness and mass loss rates of RGB and

AGB stars, however, makes them very important for the integrated luminosity and dynamical evolution of star clusters. By coupling the stellar evolution models to a description of how the stellar mass in a cluster is distributed over stars of different masses (which is the stellar initial mass function or IMF), precise predictions can be made of how the luminosity and mass of star clusters evolve over time. This is the domain of evolutionary synthesis modelling, and today there are many of these models, the so-called SSP models, available (e.g. Leitherer et al. 1999, Bruzual & Charlot 2003, Anders & Fritze-v. Alvensleven 2003, Maraston 2005). Most of these models have a different treatment of the RGB and AGB phases, resulting in large differences in the model output (such as intrinsic colour) at certain ages where these phases become important (e.g. between 200 Myr and 1 Gyr for the AGB phase and between 1–2 Gyr when the RGB develops). Since SSP models are widely used in star cluster research, it is crucial to know which models are best.

The duration of the phase in which stellar evolution dominates the appearance of clusters depends on the local environment in the host galaxy. In a dynamically calm environment, such as the outer regions of a galaxy or galaxies without strong spiral arms or many gas clouds, stellar evolution can dominate the evolution of clusters up to $\sim$ 1 Gyr. At this time a cluster will have lost about 25% of its initial mass due to stellar evolution (Lamers et al. 2005). If the environment is less calm, a cluster will experience shocks from encounters with other clusters, gas clouds and spiral arms. This will shorten the period during which stellar evolution dominates to a few hundred Myrs, before internal and external dynamical effects become more important.

These dynamical effects control the third and last phase in the evolution of star clusters. As a result of random encounters between two or three stars, the velocity of some stars can become larger than the escape velocity of the cluster. These stars will disperse into the field. This process will eventually lead to the complete dissolution of the cluster. It is enhanced in regions where there are more encounters with gas clouds or spiral arms, since such encounters will "heat" the cluster by increasing the total kinetic energy of the stars (Spitzer 1958, Gieles et al. 2006c). A stronger tidal field (e.g. closer to a galaxy's centre) will also enhance the dissolution, since it will make the tidal radius of the cluster smaller and as a result a lower velocity is needed for a star to disperse into the field.

The dissolution time $t_{\rm dis}$, which is the time it takes stellar evolution and dynamical effects to dissolve a cluster completely, does not only depend on the environment of the cluster. It is also found to scale with the mass of a cluster as $t_{\rm dis} \propto M^{0.6}$. This mass dependence was found empirically in the study of the age and mass distributions of cluster populations (Boutloukos & Lamers 2003, Lamers et al. 2005), and independently from N-body simulations of star clusters in a tidal field (Baumgardt & Makino 2003). Together with N-body simulations of the shocks experienced by spiral arm passages (Gieles et al. 2007) and encounters with GMCs (Gieles et al. 2006c), a picture has begun to emerge in which we can describe the largest part of the life of a star cluster (Lamers & Gieles 2006a).

By understanding the stellar and dynamical evolution phases in the life of star

clusters, we can take a population of observed, aged clusters and derive what the initial population of clusters looked like. This way we begin to understand what an observed population of star clusters in a galaxy tells us about the *cluster* formation history of this galaxy. However, the first phase of violent relaxation, is critical if we want to exploit the same population of clusters to study the *star* formation history. The process and outcome of violent relaxation holds important clues to the details of star formation itself. Only if we understand these, we can find the link between observed star clusters and the star formation history of galaxies.

1.3 Violent relaxation

As previously mentioned, the majority of star clusters are believed to become unbound in their first few Myrs after formation. During this period the clusters emerge from their enshrouding gas clouds and become optically visible. By comparing the formation rates of optically visible star clusters to those of clusters still embedded in their natal gas, Lada & Lada (2003) find that $\sim$ 90% of the clusters in the solar neighbourhood do not survive this process. The reason for this "infant mortality" is the violent relaxation triggered by the gas expulsion. In what follows I first describe the process of gas expulsion and then explain how this leads to infant mortality.

During the collapse of a GMC, the increasing density in the cloud will lead to a decreasing Jeans mass. As a result, parts of the cloud will satisfy the local Jeans criterion for gravitational collapse, and the cloud will fragment into individual clumps. These clumps will collapse by themselves and form the protostars in the cluster, the masses of which are distributed according to the IMF. This means that there will only be a few massive protostars, and many more with lower masses. The massive protostars are the first to reach the state of burning hydrogen in their core, which marks the start of their lifes as stars. At this point these massive stars are so bright in the ultra-violet (UV) part of the spectrum, that their radiation starts to ionise the residual gas in the cluster. These massive stars will ionise their surrounding medium and eject strong radiation-driven winds. These winds begin to expel the gas, which is only weakly bound to the protostars, from the cluster. These massive stars soon end their lives in supernovae, which push the remaining gas from the cluster. An example of this process can be seen in Fig. 1.3, which shows the Galactic star cluster NGC 3603 as captured by the *HST's Wide Field and Planetary Camera 2* (*WFPC2*). The fact that we see young star clusters expelling their residual gas indicates that not all material of the GMC is used to form stars. This shows that the *Star Formation Efficiency* (SFE) is not 100%, where the SFE is defined as the mass fraction of the GMC turned into stars.

When gas is removed from the cluster, gravitational binding energy is also removed with it. In other words: the stars in the cluster reside in a gravitational potential well that suddenly becomes shallower due to the removal of mass. This removal can be treated as "sudden", as it happens on a timescale shorter than the

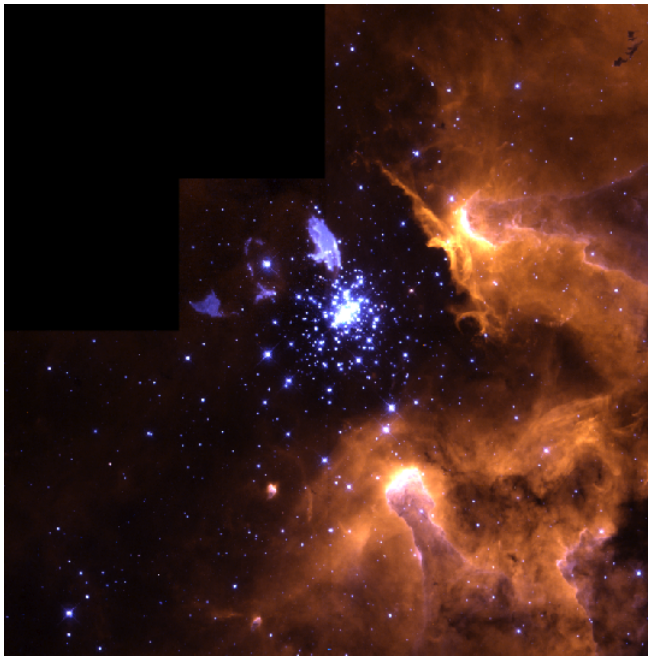

Figure 1.3: *HST/WFPC2* image of NGC 3603. The colour version of this image can be found on page 130. Many of the bright, blue stars in the centre of the cluster are young O-type stars. Their strong UV radiation is ionizing the remaining gaseous material, which glows in yellow-brown in the colour version of this image. After being ionised, the strong stellar winds blow the material out of the cluster. The small blue nebulae, top-left of the centre, are the result of the fast wind of the blue supergiant Sher 25, colliding with material from its preceding slower wind (Chita et al. 2008). This shows that fast winds are indeed present in young star clusters. Image courtesy of W. Brandner (JPL/IPAC) and NASA.

crossing timescale[1] of stars in the cluster (Goodwin 1997). Therefore, the stars cannot immediately adapt to the lower potential (they need a few crossing times to do this) and many stars will have a velocity higher than the one dictated by virial equilibrium. As a result the cluster will expand and a certain fraction of stars will leave the cluster. This type of initial mass loss is dubbed "infant weight loss". If enough mass is lost, the response of the cluster will be so violent that it disrupts completely, in which case we speak of "infant mortality".

The mass fraction of star formation that we can detect in young and optically visible star clusters is defined as the *Cluster Formation Efficiency*, or CFE. The scenario

[1] The crossing (or *dynamical*) timescale of a system is defined by R/v, where R is the characteristic radius of the system and v the characteristic velocity of the bodies in the system. For a star cluster, R is usually taken to be the core radius r_c (i.e. the radius where the surface brightness of the cluster is half its central value) and v is taken to be $3^{1/2}$ times the radial velocity dispersion in the core (Spitzer 1987). This results in a typical crossing timescale of $\sim 10^5$ years.

above illustrates that the fraction of clusters that survive infant mortality is coupled to the fraction of mass that can be blown out of the cluster by the first massive stars. The CFE is therefore directly coupled to the SFE. It is expected that a lower SFE will lead to more gas removal and thus to a higher infant mortality and a lower CFE.

Many questions, however, remain to be answered. First, the value of the SFE is not well determined. This problem is coupled to the spatial scale under consideration. On the scale of entire GMCs, the SFE will be of the order of a few percent (Lada & Lada 2003). However, in the core of a GMC that actually forms the star cluster, the SFE will be higher, probably around 10–40% (Parmentier & Fritze 2008). It is this SFE in the core that determines how much mass will be rejected from the newly formed cluster. Elmegreen & Efremov (1997) predict that the SFE scales with the pressure of the environment. This ambient pressure is expected to be higher in central regions of galaxies, regions of high turbulent compression and large-scale shocks in interacting galaxies (e.g. Jog & Solomon 1992). Only if the pressure is high enough, the binding energy of the cluster will be high enough to prevent the winds and radiation of the first massive stars to reject enough gas and completely disperse the cluster. More observations of the exact values and the environmental dependencies of either the SFE (in the cluster forming *cores* of the GMCs), infant mortality rate or CFE are necessary to test this theory.

Second, the fate of a newly formed cluster (i.e. does it remain bound or become unbound) might also depend on the metallicity of the primordial material. If the metallicity is higher, the radiation-driven winds of the first O and B-stars will be stronger. This could result is more efficient gas expulsion, and therefore more infant mortality, in regions where the metallicity is higher.

Finally, there are open questions related to the timescale of violent relaxation. In a weak tidal field, models predict that the effects of violent relaxation become apparent after an age of $\sim$ 10 Myr, and that it lasts till an age of $\sim$ 50 Myr (Goodwin & Bastian 2006, Parmentier 2009). In a strong tidal field, however, these timescales might be considerably smaller. Is this observed to be the case? Also here, more observations are necessary.

Because the CFE is a tracer of the SFE, observations of young star clusters can be used to tackle all these open questions. Many of the processes discussed so far (violent relaxation, cluster evolution) depend on the environmental conditions, such as ambient pressure or tidal field strength. Some processes also depend on the masses and radii (sizes) of GMCs and star clusters, or they have a specific impact on these structural parameters. This implies that we can study these processes by means of the mass and radius distributions and the mass-radius relations of large populations of clouds and star clusters in different environments. The formation and early evolution of star clusters can be studied by comparing these distributions and relations to those of the progenitor clouds and clumps (i.e. the cores of clouds). The subsequent evolution of star clusters can in turn be studied by comparison of differently aged cluster populations.

Today, the structural properties of GMCs are reasonably well known. As we mentioned in section 1.1, Larson (1981) observed a relation between the velocity

dispersion and radius of GMCs of the form $\sigma \propto R^{0.38}$, and Solomon et al. (1987) observed $\sigma \propto R^{0.5}$. Assuming that GMCs are in virial equilibrium, i.e. $\sigma^2 \propto M/R$ in which M is the GMC mass, these observations lead to the mass-radius relation for clouds: $R \propto M^x$ with x in the range 0.5–0.6. For young star clusters this relation is significantly weakened or even missing (Larsen 2004). In section 1.1 it was also mentioned that large-scale turbulence results in power-law mass and radius distributions of clouds. These are now well observed (Elmegreen & Falgarone 1996). The mass distribution of young star clusters is observed to follow the power-law mass distribution of clouds (see e.g. Zhang & Fall 1999, Bik et al. 2003, de Grijs et al. 2003a). The radius distribution of clusters, however, is less well constrained, despite the fact that it holds important clues to the structural changes during violent relaxation and the missing mass-radius relation of clusters.

At the present time it is impossible to obtain a complete picture of star formation and the SFE directly. The problem is to observe star formation in detail, on large scales, in a consistent manner and under a range of different environmental conditions (such as a strong or weak tidal field), simultaneously. This is due to the required high resolution of the observations, combined with the proper wavelength range (infrared) and large field of view. However, by using star clusters we can begin to tackle all these issues *in*directly, so that eventually we can understand star formation and the SFE throughout the evolution of galaxies by means of the observed clusters.

It is clear that for this we need observations of large star cluster populations, preferably throughout entire galaxies, in order to sample different scales and environmental conditions in a consistent way. This is now possible with new observations such as those of the Whirlpool Galaxy, taken with the *HST* using the *Advanced Camera for Surveys* (*ACS*).

1.4 The Whirlpool Galaxy

In this thesis I set out to determine the properties of young star clusters in the Whirlpool Galaxy M51 (NGC 5194), using the new *HST*/*ACS* mosaic image, combined with *WFPC2* and *Near Infrared Camera and Multiple Object Spectrometer* (*NICMOS*) data. Figure 1.4 shows a greyscale composite of the *ACS* image, which is a combination of images taken through the B_{F435W}, V_{F555W}, I_{F814W} and $H\alpha_{F658N}$ filter bands[2]. The colour composite *ACS* image can be found on page 131. Since it is a mosaic of six separate pointings, the total field-of-view spans an area of $430'' \times 610''$ or 17.5×24.8 kpc at the distance of M51 of 8.4 ± 0.6 Mpc (Feldmeier et al. 1997).

Figure 1.4 shows M51 on the left, and its companion galaxy, NGC 5195, on the right. It is evident that M51 is a grand-design, late type (Sbc) spiral galaxy and that we observe it nearly face-on. The inclination angle is only 20° (Tully 1974), which

[2]In this notation of the filter bands the subscript refers to the exact *ACS* filter name, while the upper-case letter refers to the corresponding filter band in the standard Johnson-Cousins system. There are slight differences between these systems, but note that throughout this thesis I will work in the *ACS* system without applying any transformations.

Figure 1.4: *HST/ACS* mosaic image of the NGC 5194/5195 system, taken as part of the Hubble Heritage Project (Mutchler et al. 2005, http://archive.stsci.edu/prepds/m51/). M51 (NGC 5194) is the spiral galaxy on the left. The image spans an area of 430″ × 610″, which corresponds to 17.5 × 24.8 kpc at the distance of 8.4 ± 0.6 Mpc. The colour version of this image can be found on page 131.

means that we can observe the entire disc and that extinction effects are kept to a minimum. The majority of the star clusters reside in the disc, which has a negligible thickness compared to the distance of M51. Therefore the distances to the clusters are all the same, which is another advantage of extragalactic star cluster studies over Galactic studies.

Due to the clear spiral structure, M51 is also known as the "Whirlpool Galaxy". The spiral arms are likely enhanced due to the interaction with NGC 5195. Models by Salo & Laurikainen (2000) show that a close passage of NGC 5195 400–500 Myr ago, followed by a second passage more recently, is responsible for the main spiral structure. The tidal interaction is also responsible for an enhanced star formation activity. Bastian et al. (2005b) have shown that ∼ 60 Myr ago there was a burst in the cluster formation rate (CFR), consistent with the proposed second passage of NGC 5195 50–100 Myr ago by Salo & Laurikainen (2000). The current overall star formation rate (SFR) in M51 is ∼ 3.4 $M_\odot$ yr^{-1} (Calzetti et al. 2005), which is about three times as high as in our own Milky Way. This results in many young star clusters

and thus good statistics for studies on star cluster populations. It is thanks to the amazing resolution of 2 pc per pixel of the *ACS* that we are able to identify thousands of star clusters in M51.

In summary, we have a dataset in which we can study the properties of thousands of star clusters throughout an entire galaxy in a consistent way. We can sample different environments such as the dense regions close to the centre and in the spiral arms, but also the low density regions further out and in the interarm regions. This makes this dataset unique. Assuming that M51 and its local star forming conditions are *not* unique, the findings on the star and cluster formation in a specific galaxy like M51 will improve our understanding of star formation and galaxy evolution throughout the universe.

1.5 Outline of this thesis

In this thesis I focus on various aspects on the formation and evolution of star clusters in M51. The chapters are based on a series of papers written by me in collaboration with my colleagues, in which we study the radii, masses and ages, as well as the spatial distribution of star clusters in M51. The purpose of the thesis is to compare the properties of star clusters to the properties of the clouds from which they form, and to use these properties to derive the CFE for different environmental conditions.

1.5.1 *ACS* imaging of star clusters in M51: identification and radius distribution (Chapter 2)

In Chapter 2 we address the differences in structural parameters between clouds and clusters, and how the radii of star clusters depend on environmental conditions. We compare the radius distributions of clouds and clusters, and we search for a cluster mass-radius relation.

We start by identifying a large sample of star clusters in the M51 *HST*/*ACS* dataset. The selection of the star clusters is done based on radius measurements. We are able to resolve 7698 star clusters on the B_{F435W} image. The radii of the brightest 1284 clusters with the smallest errors are studied in detail.

The median radius of the clusters is derived and compared between clusters in the spiral arms and clusters in the interarm regions, as well as between blue and red clusters. We interpret the colour differences between clusters as an age effect, redder clusters being older, in accordance with SSP models. We find that the radii of clusters increase with their $B-V$ colour. Also, clusters in lower background regions are redder and thus larger. We speculate that this is due to a dynamical expansion of the clusters with age. We also study the correlation between cluster radius and galactocentric distance, and find a correlation which is considerably weaker than the observed correlation for old globular clusters in the Milky Way.

The radius distribution of the star clusters is also presented and compared to the radius distribution of GMCs. It is shown that the radius distributions of clusters

and GMCs are different. We also show that there is no relation between the mass and radius of clusters, while such a relation is observed for GMCs. Since the mass distributions of GMCs and young clusters are similar, these observations suggest that the radii of star clusters have changed shortly after formation. However, the current scenarios to explain early cluster expansion are not consistent with the radius distribution we observe.

Finally, we find six new candidates for "faint fuzzy" star clusters, projected onto the disc of M51. One of these objects is peculiar, since it is very large and located (in projection) very close to the centre of M51. This peculiar object is studied separately in Chapter 3.

1.5.2 A peculiar object in M51: fuzzy star cluster or a background galaxy? (Chapter 3)

In Chapter 3 we focus on the nature of the peculiar object mentioned in Chapter 2. We try to answer whether it is a background galaxy, a cluster in the disc of M51, or a cluster in front of the disc. We complement the data with photometry from the *NICMOS* instrument in the near-infrared. We estimate the extinction and fit the surface brightness profile of the object with different cluster and galaxy models.

We find that it is not very likely that the object is a background galaxy, based on its intrinsic colour and surface brightness profile. Assuming the object is a star cluster we estimate its age, mass and extinction using SSP models. From this we conclude that it is not impossible, but unlikely that the object is a star cluster in the disc of M51, since this would mean that we observe it just prior to its dissolution. Our favourite scenario is therefore the one in which the object is a cluster seen in projection against the disc. In this scenario the cluster is a real faint fuzzy cluster and not observed in a special phase of its lifetime.

1.5.3 The spatial distribution of star and cluster formation in M51 (Chapter 4)

In Chapter 4 we address the issue of the universality of hierarchical star formation. We study whether the spatial distribution of star clusters shows the same amount of hierarchy as the turbulent ISM. We further derive how well the positions of young star clusters are correlated with independent tracers of star formation.

We first complement the *ACS* dataset with data in the near-UV. We add *WFPC2* U_{F336W} photometry to the resolved star clusters, which means that we can estimate the ages, masses and extinctions of 1580 star clusters based on SSP model fitting. The ages are used to select a young, intermediate and old cluster sample.

We use two-point autocorrelation functions to study to what degree the positions of the clusters are clustered. This clustering of clusters provides clues to the amount of hierarchy present in the star formation process. We generally find that the amount of hierarchy (in terms of the fractal dimension) of the star clusters is similar to

the amount of hierarchy observed for interstellar gas and for star clusters in other galaxies. This is evidence suggesting that the fractal dimension is universal.

In this chapter we also exploit different multi-wavelength datasets, to have independent tracers of the locations and the amounts of star formation throughout M51. Information of the spatially resolved SFR is taken from the literature. We find that the positions of the youngest star clusters (ages < 10 Myr) show the strongest correlations with the resolved SFRs, the spiral arms and emission in Hα and the radio-continuum, while these correlations decrease for the older clusters. This shows that the youngest star clusters are spatially correlated, not only with each other, but also with the current star formation sites in M51. In Chapter 5 we will quantify this correlation.

1.5.4 The star cluster formation efficiency in M51 (Chapter 5)

In Chapter 5 we come back to the question of exactly how much star formation actually occurs in clusters, and how this depends on environmental conditions. In the previous chapter we have shown that the youngest star clusters are spatially correlated to the star formation sites in M51. In this chapter we take the next step of actually studying what fraction of the star formation takes place in the star clusters we observe. We derive the CFE, assumed to be a tracer of the SFE (see section 1.3) and study its environmental dependencies. We also address the timescale of violent relaxation.

After matching the young (< 10 Myr) star clusters with 200 apertures for which we know the SFRs, we find that the clusters represent only 5% (in mass) of the star formation. This fraction does not seem to depend on the environmental conditions such as the local SFR, galactocentric distance or spiral arm distance. This suggests that the CFE and the SFE (and therefore likely the infant mortality) are constant throughout M51.

The fraction of 5%, however, is a lower limit, since we cannot observe the clusters with the lowest masses in M51. To correct for this, we derive and discuss the cluster initial mass function (CIMF). More massive clusters can be lost in our detection due to enshrouding gas clouds or due to confusion effects. After correction for these detection losses, we find that the CFE $\approx$ 20%. In other words, $\approx$ 20% (in mass) of the star formation takes place in the form of star clusters. The remaining 80% takes place in a dispersed way. Considering the effects of violent relaxation and infant mortality discussed in Sect. 1.3, this suggests that the infant mortality can be as high as 80% and occurring on timescales of less than 10 Myr.

1.6 Outlook

In this thesis we gained more insight in early star cluster evolution, the CFE and its environmental dependencies. It is clear that many open questions remain and that some new questions have arised. Here I discuss possible strategies to handle some of these questions.

A clear limitation of the study presented here is that we only address a single spiral galaxy. Although the disc of M51 harbours a range of different local conditions, it is difficult to study the impact of metallicity and tidal field strength using just a single galaxy. Extending the study to a range of different galaxies will provide a longer baseline of environments. This would be useful to test the importance of metallicity on the SFE and CFE, and to confirm whether infant mortality is slower in a weaker tidal field or not.

Extending the study to many more galaxies will not be easy, since one needs high spatial resolution broad-band data, including U_{F336W} to detect and age-date the clusters. These need to be combined with an extensive multi wavelength coverage in order to accurately derive extinction-corrected SFRs. However, here we might benefit from the recent advances in the studies of extragalactic resolved stellar populations (e.g. McQuinn et al. 2009). Such studies need less wavelength coverage, but can provide us with star formation histories of nearby galaxies by detecting individual stars. It remains a challenge, though, to simultaneously detect a significantly large sample of young star clusters in these galaxies in order to study the CFE, since most nearby galaxies are dwarf galaxies, which contain relatively few star clusters.

We have found that the CFE, and therefore likely the SFE, does not depend on the local SFR, galactocentric distance or spiral arm distance. This suggests that the physical conditions deep inside the cores of GMCs regulate the SFE. Future observations of the cores of GMCs by the *Atacama Large Millimeter Array* (ALMA), which is currently being constructed in Chile's Atacama desert, will give us a detailed view of the embedded phase of star cluster formation and evolution. These observations will provide us with more answers about what exactly determines the local SFE.

The study of the nature of the peculiar object in Chapter 3 will benefit from additional spectroscopic observations, or deeper U–band imaging. Such observations will provide better constraints on the extinction and age of the object and possibly on its kinematics and distance.

Finally, there are many open issues regarding the different SSP models that are used in star cluster research. Contrary to simply using a certain SSP model to study the star clusters in M51, we are currently undertaking a study in which we are using the star clusters to study different SSP models. In this study we are focussing on the near-IR colours of the models, since those are the colours in which the different treatments of the post-main sequence evolution of stars become most apparent. Our M51 star cluster data might prove capable of accepting certain SSP models above others.

Here we should also mention other factors that are important for the broad-band colour evolution of star clusters, which have so far not been taken into account in many SSP models, or which are treated differently in the different models. Stochastic effects, introduced by discrete sampling of the stellar IMF, are for example the largest contributor to the observational uncertainties of cluster ages and masses (see e.g. Maíz Apellániz 2009, and references therein). Inclusion of stochastic effects in the age, mass and extinction determinations of star clusters will considerably improve future studies of young star cluster evolution. Further improvements are also expected from

the inclusion of binary stars in the SSP models, and from the improved treatment of massive stars, extreme horizontal-branch stars and thermally pulsing AGB stars.

Chapter 2

ACS imaging of star clusters in M51: identification and radius distribution

R. A. Scheepmaker, M. R. Haas, M. Gieles, N. Bastian,
S. S. Larsen, and H. J. G. L. M. Lamers
Astronomy & Astrophysics v.469, p.925-940 (2007)

Abstract *Context.* Size measurements of young star clusters are valuable tools to put constraints on the formation and early dynamical evolution of star clusters. *Aims.* We use *HST/ACS* observations of the spiral galaxy M51 in B_{F435W}, V_{F555W} and I_{F814W} to select a large sample of star clusters with accurate effective radius measurements in an area covering the complete disc of M51. We present the dataset and study the radius distribution and relations between radius, colour, arm/interarm region, galactocentric distance, mass and age. *Methods.* We select a sample of 7698 (B_{F435W}), 6846 (V_{F555W}) and 5024 (I_{F814W}) slightly resolved clusters and derive their effective radii ($R_{\rm eff}$) by fitting the spatial profiles with analytical models convolved with the point spread function. The radii of 1284 clusters are studied in detail. *Results.* We find cluster radii between 0.5 and ~10 pc, and one exceptionally large cluster candidate with $R_{\rm eff}$ = 21.6 pc. The median $R_{\rm eff}$ is 2.1 pc. We find 70 clusters in our sample which have colours consistent with being old GC candidates and we find 6 new "faint fuzzy" clusters in, or projected onto, the disc of M51. The radius distribution cannot be fitted with a power law similar to the one for star-forming clouds. We find an increase in $R_{\rm eff}$ with colour as well as a higher fraction of clusters with $B-V \gtrsim 0.05$ in the interarm regions. We find a correlation between $R_{\rm eff}$ and galactocentric distance ($R_{\rm G}$) of the form $R_{\rm eff} \propto R_{\rm G}^{0.12\pm0.02}$, which is considerably weaker than the observed correlation for old Milky Way GCs. We find weak relations between cluster luminosity and radius:

$R_{\rm eff} \propto L^{0.15\pm0.02}$ for the interarm regions and $R_{\rm eff} \propto L^{-0.11\pm0.01}$ for the spiral arm regions, but we do not observe a correlation between cluster mass and radius. *Conclusions.* The observed radius distribution indicates that shortly after the formation of the clusters from a fractal gas, the radii of the clusters have changed in a non-uniform way. We find tentative evidence suggesting that clusters in spiral arms are more compact.

2.1 Introduction

One of the most striking questions related to star cluster formation concerns the transition from the densest parts of the star-forming Giant Molecular Clouds (GMCs) to the clusters that emerge from them. Observations show that the masses and radii of clouds follow a clear relation of the form $R_{\rm GMC} \propto M_{\rm GMC}^{1/2}$ (e.g. Larson 1981, Solomon et al. 1987) down to the scale of the star forming clumps (Williams et al. 1995). Such a relation is expected for self-gravitating clouds, which are in virial equilibrium and pressure bounded by their surroundings (e.g. Elmegreen 1989). The same mass-radius relation is observed for *complexes* of multiple clusters (Elmegreen & Salzer 1999, Elmegreen et al. 2001, Bastian et al. 2005a). Elliptical galaxies and very massive ($> 10^{6.5}\,M_\odot$) stellar clusters follow a similar relation ($R \propto M^{0.62}$ (Haşegan et al. 2005)), which advocates a possibility of forming very massive clusters by merging of low mass clusters (Fellhauer & Kroupa 2005, Kissler-Patig et al. 2006).

However, for individual star clusters that emerge from the star forming clouds or clumps, a relation between mass and radius is not present (Van den Bergh et al. 1991, Bastian et al. 2005b, Jordán et al. 2005) or at least strongly weakened (Zepf et al. 1999, Hunter et al. 2003, Mackey & Gilmore 2003, Larsen 2004, Lee et al. 2005). Since this is already the case for very young clusters, it indicates that during, or shortly after (< 10 Myr) the transition from clouds to clusters the mass and/or the radius of the objects change.

These changes in mass and/or radius are likely to be reflected in changes in the mass and radius *distributions* (Ashman & Zepf 2001). On the one hand, however, the mass distributions of both clouds and clusters show great similarities. Both can be approximated by power laws of the form $N(M)\mathrm{d}M \propto M^{-\alpha}\mathrm{d}M$, with the index α in the range of 1.5–2.0 (see Sanders et al. 1985, Solomon et al. 1987, Harris & Pudritz 1994, Brand & Wouterloot 1995, Elmegreen & Falgarone 1996, Fukui et al. 2001 for clouds and see e.g. Zhang & Fall 1999, Ashman & Zepf 2001, Bik et al. 2003, de Grijs et al. 2003b, Hunter et al. 2003 for clusters). Recently, some studies have found evidence for an upper mass truncation of the cluster mass distribution Gieles et al. (2006b), Dowell et al. (2006), which is also found for the mass distributions of GMCs (Rosolowsky 2005). On the other hand, the radius distributions are less well constrained, especially for extragalactic star clusters. If we approximate the radius distributions by a power law of the form $N(R)\mathrm{d}R \propto R^{-\eta}\mathrm{d}R$, the average value of the index for GMCs is observed to be $\eta = 3.3 \pm 0.3$ (Harris & Pudritz 1994, Elmegreen & Falgarone 1996), consistent with the gas having a fractal structure with a fractal

dimension $\eta - 1 = 2.3 \pm 0.3$ (Mandelbrot 1983, Elmegreen & Elmegreen 2001). For young clusters in NGC 3256 Zepf et al. (1999) find $\eta \approx 3.4$, while Bastian et al. (2005, from now on referred to as "B05") find $\eta = 2.2 \pm 0.2$ for star clusters in the disc of M51. This difference, however, seems to be caused by the erroneous addition of +1 to the index in the result of Ashman & Zepf (2001).[1]

Our understanding of whether or not the mass and radius distribution of clouds and clusters are similar, and to which degree, is directly coupled to our understanding of star formation and the early evolution of star clusters. Besides that, possible explanations for the lack of a mass-radius relation for clusters which change the mass and/or the radius of the clusters in a non-uniform way, are likely to affect the mass and radius distributions (Ashman & Zepf 2001). It is therefore important to put better constraints on these distributions, and in this work we will focus on the radius distribution of young star clusters.

In the study presented here we exploit the superb resolution and large field-of-view of the new *HST Advanced Camera for Surveys* (*ACS*) observations of M51, taken as part of the Hubble Heritage Project. These observations allow us to measure the radii of a large sample of clusters in an area covering, for the first time, the complete disc of M51 and its companion, NGC 5195 at a 0.05'' resolution. In this chapter we present the dataset and we study the radius distribution for the complete cluster sample and for cluster samples with a different background surface brightness ("background regions"). The differences in background regions are likely to reflect differences in environmental conditions, which could have an impact on the early evolution of star clusters.

The radii of star clusters in M51 have already been studied by B05 and Lee et al. (2005). However, these studies used lower resolution *HST/WFPC2* data and were not covering the complete disc. Besides this, we use different selection criteria for the clusters than B05, based on the clusters actually being resolved and clearly separated from nearby contaminating sources. In combination with the larger field-of-view and the higher resolution of the *ACS* data, this leads to a larger sample of clusters, divided in different background regions.

The structure of this chapter is as follows: in Sect. 2.2 we describe the dataset, the selection of sources and background regions and the photometry. The radius measurements are described in Sect. 2.3 and in Sect. 2.4 we describe experiments with artificial clusters to determine the accuracy and detection limits of our methods. Our selection criteria and a description of our cluster sample are presented in Sect. 2.5, followed by a comparison between *ACS* and *WFPC2* data in Sect. 2.6. The radius distribution is presented in Sect. 2.7, and we search for correlations between mass, radius and galactocentric distance in Sect. 2.8. In Sect. 2.9 we finish with the summary and conclusions.

[1] Fitting a function of the form $\log(N(r)) = a + b \cdot \log(r)$ results in $b = -\eta$. However, using logarithmic binning, one fits $\log(N(\log(r))) = a + b \cdot \log(r)$, in which $b = 1 - \eta$. This extra term +1 can easily cause confusion when comparing different distributions. Also see B05 and Elmegreen & Falgarone (1996).

Table 2.1: Overview of the filters and exposure times used. The limiting magnitude is for a point source with S/N = 5.

Filter	Exposure time	Limiting magnitude
B_{F435W}	4×680 s = 2720 s	27.3 m_B
V_{F555W}	4×340 s = 1360 s	26.5 m_V
I_{F814W}	4×340 s = 1360 s	25.8 m_I
$H\alpha_{F658N}$+N[II]	4×680 s = 2720 s	–

2.2 Observations, source selection and photometry

2.2.1 Observations

We make use of the *HST/ACS* dataset of M51 (NGC 5194, a late type Sbc galaxy), taken as part of the Hubble Heritage Project in January 2005 (proposal ID 10452, PI: S. V. W. Beckwith). The dataset consists of 6 *ACS* pointings using the Wide Field Channel (*WFC*) in B_{F435W} ($\sim B$), V_{F555W} ($\sim V$), I_{F814W} ($\sim I$) and $H\alpha_{F658N}$, with 4 dithered exposures per filter, as is summarised in Table 2.1. The observations were reduced and drizzled into one mosaic image by Mutchler et al. (2005). In summary, the standard *ACS* pipeline (CALACS) was used for bias, dark and flat-field corrections of the individual dithered images. The corrected images were then combined into one mosaic image using the `MultiDrizzle` task (Fruchter & Hook 2002, Koekemoer et al. 2002), which also corrects for filter-specific geometric distortion, cosmic rays and bad pixels. For a complete description of the dataset we refer to Mutchler et al. (2005) and the M51 mosaic website (`http://archive.stsci.edu/prepds/m51/`). For details on the standard pipeline processing we refer to the *ACS Data Handbook* (Pavlovsky et al. 2005).

The resulting mosaic image covers a region of $430 \times 610''$ (= 17.5×24.8 kpc) with a resolution of 2.0 pc per pixel, where we assumed a distance modulus of $m - M = 29.62$ from Feldmeier et al. (1997), i.e. a distance of 8.4 ± 0.6 Mpc. The covered region is large enough to include the complete spiral disc of M51, as well as its companion NGC 5195 (a dwarf barred spiral of early type SB0), while at the same time the resolution is good enough to *resolve* stellar cluster candidates, i.e. to distinguish them from stars by measuring their sizes and comparing these to the *Point Spread Function* (PSF) of the *HST/ACS* camera.

2.2.2 Source selection

For source selection we used the SExtractor package (Bertin & Arnouts 1996, version 2.3.2). SExtractor first generates a background map by computing the mean

and standard deviation of the intensity of every section of the image with a user defined grid size for which we choose 10×10 pixels. In every section the local background histogram is clipped iteratively until every remaining pixel value is within $\pm 3\sigma$ of the median value. The mean of the clipped histogram is then taken as the local background value. Every area of at least three adjacent pixels that exceeded the background by at least 5σ was called a source. For details on the background estimation and the source selection we refer to the SExtractor user manual (Bertin & Arnouts 1996) or Holwerda (2005). The coordinates of the sources in B_{F435W}, V_{F555W} and I_{F814W} were matched and only sources that were detected in all three filters within two pixel uncertainty were kept. This resulted in a list of 75 436 sources, including cluster candidates but also many stars and background galaxies. We did not apply any selection criteria based on shape, sharpness or size during the source selection with SExtractor. However, in Sect. 2.5 we use individual radius measurements to select a large sample of cluster candidates from the source list.

2.2.3 Background selection

In order to study any possible relations between radius and environment, and to perform completeness and accuracy tests for different background levels, we divided the image into three regions according to the background surface brightness. These background regions were selected by smoothing the V_{F555W} image with a boxcar average of 200 pixels. Consequently, pixels with a value < 0.19 e$^-$/s (corresponding to a surface brightness $\mu > 21.02$ mag arcsec^{-2}) were flagged "low background". Pixel values ≥ 0.19 e$^-$/s and < 0.25 e$^-$/s ($20.72 < \mu < 21.02$ mag arcsec^{-2}) were flagged "intermediate background" and pixels with a value ≥ 0.25 e$^-$/s ($\mu < 20.72$ mag arcsec^{-2}) were flagged "high background". These values were chosen because they resulted in a contour map, shown in Fig. 2.1, in which the high background region clearly follows most of the inner spiral arms, covering most areas that would be marked "high background" if the selection would take place by eye. The "intermediate" region should be considered as a transition region to clearly separate cluster samples within a low and high background region.

2.2.4 Point spread function

For our photometry, radius measurements and artificial cluster experiments we need a filter dependent PSF. Since there are not enough bright, isolated point sources in the M51 mosaic image to determine the PSF accurately, the PSF was observationally determined from a crowded star field on a drizzled image of the Galactic globular cluster 47 Tuc (NGC 104, *HST* proposal GO-9281, PI: J. E. Grindlay). For each filter a separate PSF was determined.

With drizzled data, the size of the PSF depends on the choice of the drizzle kernel and the accuracy with which the flux from multiple images is combined. We note that the image of 47 Tuc was drizzled in a slightly different way than the M51 image. The 47 Tuc images were drizzled using a square kernel with a size of one pixel (i.e.

Figure 2.1: The contours outlining the three background regions, superimposed on the *HST/ACS* mosaic image in the V_{F555W} passband. The solid lines enclose "high background" regions, and everything outside the dashed lines indicates the "low background" regions. The regions in between solid and dashed lines are called "intermediate background".

pixfrac = 1.0 (Fruchter & Hook 2002)), while a Gaussian kernel with pixfrac = 0.9 was used for M51. Therefore, we expect some differences between the PSFs, with the M51 PSF possibly being larger than the 47 Tuc PSF. This could lead to an overestimation of the measured radii. However, tests by Larsen (2004) have shown that the lower limit down to which ISHAPE can detect a source as being resolved is ~10% of the FWHM of the PSF. At the distance of M51 and with a FWHM of the ACS PSF of ~2.1 pixels, this corresponds to an effective radius ($R_{\rm eff}$) of ~0.5 pc. We indeed find a very strong

peak in the $R_{\rm eff}$ distribution of all measured sources below 0.5 pc, consistent with the majority of the sources (faint stars) being fit as point sources.

This peak of point sources implies that the measured radii are *not* biased towards larger values. We therefore conclude that the empirical PSF we use, although drizzled in a slightly different way than the image of M51, is *not* too small. It shows that other effects on the PSF, like combining the flux of multiple separate images, are more important than the differences in the drizzle parameters. In Sect. 2.6 we also show that there are no large systematic offsets between our measured radii and the radii of some clusters that were independently measured by B05 using *WFPC2* data. We can therefore use the empirical PSF from the image of 47 Tuc and we will use as a lower-limit for the measured $R_{\rm eff}$ a value of 0.5 pc.

2.2.5 Photometry

We performed aperture photometry on all sources in the source list using the IRAF[2]/DAOPHOT package. We used a 5 pixel aperture radius and a background annulus with an inner radius of 10 pixels and a width of 3 pixels.

The aperture correction ($\mathrm{AC}_{0.5''}$) for resolved sources from the 5 pixel aperture to 10 pixels (= 0.5″) depends on the size of the source. Larger sources will have more flux outside the measuring aperture, and therefore need a larger (i.e. more negative) aperture correction. We measured the aperture corrections on artificial sources with different effective (i.e. projected half-light) radii between ∼ 1 pc and ∼ 5 pc, generated by the BAOLAB package (Larsen 1999, 2004). For these artificial sources we used Moffat profiles (Moffat 1969) with a power-law index of −1.5, which we convolved with the filter dependent PSF of the *HST*/*ACS*. The aperture correction was then measured by comparing the photometry between a 5 and 10 pixel aperture.

The measured aperture corrections in all three filters (B_{F435W}, V_{F555W} and I_{F814W}) show a clear linear relation with the measured size of the analytical cluster. Fig. 2.2 shows the results for B_{F435W}. The relations between $\mathrm{AC}_{0.5''}$ and measured effective radius ($R_{\rm eff}$) for the different filters can be written as:

$$\begin{aligned} B_{F435W}: \frac{\mathrm{AC}_{0.5''}}{\mathrm{mag}} &= -0.045 - 0.043 \cdot \left(\frac{R_{\rm eff}}{\mathrm{pc}}\right) \\ V_{F555W}: \frac{\mathrm{AC}_{0.5''}}{\mathrm{mag}} &= -0.045 - 0.042 \cdot \left(\frac{R_{\rm eff}}{\mathrm{pc}}\right) \\ I_{F814W}: \frac{\mathrm{AC}_{0.5''}}{\mathrm{mag}} &= -0.057 - 0.043 \cdot \left(\frac{R_{\rm eff}}{\mathrm{pc}}\right). \end{aligned} \tag{2.1}$$

For a source which has a typical measured size of 3 pc (see Sect. 2.7), this corresponds to an aperture correction of −0.17, −0.17 and −0.19 mag in B_{F435W}, V_{F555W} and I_{F814W}, respectively.

[2]The Image Reduction and Analysis Facility (IRAF) is distributed by the National Optical Astronomy Observatories, which are operated by the Association of Universities for Research in Astronomy, Inc., under cooperative agreement with the National Science Foundation.

We could use Eq. 2.1 to apply a size-dependent aperture correction to every source based on their radius measurement. However, this could introduce new and unknown systematic uncertainties due to the limitations of the radius measurements. We therefore decided to use a fixed aperture correction, determined for a 3 pc source. We are aware that this introduces uncertainties in the flux as a function of the sizes of the sources (Anders et al. 2006). We will underestimate the flux by ∼0.3 mag for a 9 pc source and overestimate the flux with ∼0.1 mag for a 0.5 pc source (also see Sect. 2.4). However, it is preferred to deal with these systematic uncertainties of known origin rather than introducing new uncertainties due to the less well determined uncertainties of the sizes. Moreover, since the coefficients in Eq. 2.1 are very similar for the different filters, uncertainties in the aperture corrections practically cancel out when we consider colours instead of fluxes. Nevertheless, when necessary we will mention how our results change if we use the size-dependent aperture corrections.

The filter dependent aperture corrections from 0.5″ to infinity (the "infinity corrections") were taken from Table 5 of Sirianni et al. (2005), which were determined for point sources. In principle, with these infinity corrections for point sources we are slightly underestimating the infinity corrections for resolved sources. However, in Sect. 2.4 we will show, using artificial cluster experiments, that with the infinity corrections for point sources we are not introducing systematic offsets in the photometry for 3 pc sources.

A final correction for Galactic foreground extinction of $E(B-V) = 0.038$ in the direction of M51 was applied, according to Appendix B of Schlegel et al. (1998). This corresponds to an additional correction in B_{F435W}, V_{F555W} and I_{F814W} of −0.152, −0.117 and −0.068 mag, respectively.

We did not apply any CTE corrections, since on the drizzled mosaic image the exact location of every source on the CCD is not easily retrieved, nor did we do photometry on the single (i.e. "un-stacked") exposures, both of which are necessary to calculate the CTE corrections. We have estimated the CTE corrections to be of the order of −0.02 mag and therefore ignoring them does not lead to large systematic effects. We also did not apply a correction for the impact of the *red halo* (Sirianni et al. 2005) on our I_{F814W} photometry, since clusters in the spiral disc of M51 are mainly blue objects and the red halo effect is most significant for very red objects observed in the *F850LP* filter. Using Tables 6 and 8 from Sirianni et al. (2005) we estimate that the error in the infinity correction for our I_{F814W} photometry would be of the order of ∼ 0.01 mag, if the clusters would be red objects. This shows that the red halo effect has no significant effect on our photometry.

2.3 Radius measurements

We exploit the resolution of the *ACS* camera by measuring the effective radii of all 75 436 detected sources in B_{F435W}, V_{F555W} and I_{F814W}. These radii can then be used to distinguish *slightly resolved* stellar cluster candidates from stars (Sect. 2.5) and to

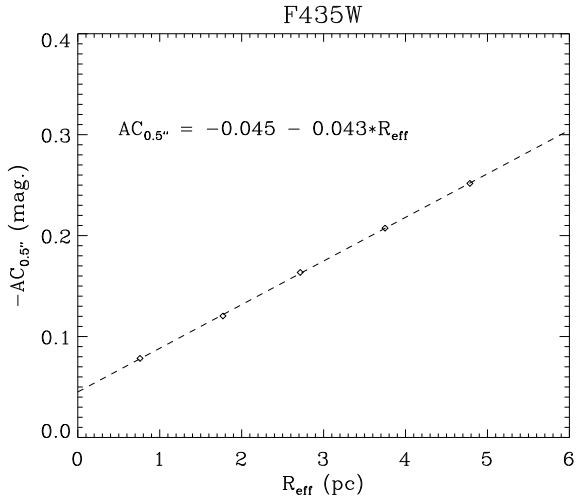

Figure 2.2: The aperture correction ($AC_{0.5''}$) for the flux between a 5 and 10 pixel (= 0.5″) aperture in B_{F435W}, versus the effective radius $R_{\rm eff}$ of analytical sources at the distance of M51 (diamonds). The dashed line is a linear fit to the data of the form of Eq. 2.1.

study the size distribution of a large sample of stellar cluster candidates (Sect. 2.7). With "slightly resolved" we mean that the cluster candidates have an intrinsic size which is comparable to or smaller than the FWHM of the PSF.

For the radius measurements we used the ISHAPE routine, which is part of the BAOLAB package (Larsen 1999, 2004). ISHAPE convolves analytic profiles for the surface brightness distribution of a cluster with different effective radii with the PSF and then fits these to each source in the data. The best fitting $R_{\rm eff}$ is then determined by minimizing the χ^2 in an iterative process. For the analytic profiles we used the same ones as for the measured aperture corrections described in Sect. 2.2.5, namely Moffat profiles with a power-law index of -1.5 (i.e. a Moffat 15 profile). These profiles were found to be the best-fitting profiles to young stellar clusters in the LMC (Elson et al. 1987).

Because the M51 *ACS* data was drizzled, the cores of the surface brightness profiles of the young clusters in M51 could have been slightly changed. We did not quantify this effect, but instead stick to the Moffat 15 profiles, since the outer regions of the profiles, which in the case of Moffat 15 profiles approximate power laws, are not expected to change.

The average surface brightness profile of Galactic globular clusters (GCs) is a King 30 profile (King 1962, Harris 1996). Tests by Larsen (1999) have shown that when clusters that follow a King profile are measured using a Moffat 15 profile, the effective radius is reproduced quite well. Therefore, even in the case where the true profiles of stellar clusters in M51 are not perfect Moffat 15 profiles, the use of this

profile will likely not lead to large systematic errors.

The radii of the sources were measured using the flux within a 5 pixel radius around the centre of the source (i.e. using an ISHAPE fitting radius of 5 pixels). To avoid neighbouring sources affecting the radius measurements, we rejected all sources which have a neighbour in the original source list within 5 pixels (see Sect. 2.5 for a full description of the selection criteria applied).

Since stellar cluster profiles are almost never perfectly spherically symmetric, we fitted them with elliptical profiles. We transformed the measured FWHM (in pixels) along the major axis into an effective radius according to the formulae from the ISHAPE user's guide:

$$R_{\rm eff} \approx 0.5(1 + \text{ratio}) \times 1.13 \times 2.036 \cdot \text{FWHM}, \tag{2.2}$$

which gives $R_{\rm eff}$ in parsecs. The factor 2.036 accounts for the size of a pixel in parsecs at the distance of M51, the factor 1.13 is the conversion factor from FWHM to $R_{\rm eff}$ for a Moffat 15 profile and the term 0.5(1 + ratio) is a correction for the elliptical profile (using the derived aspect ratio). Because of the correction for ellipticity, Eq. 2.2 gives the radius of a circular aperture containing half the total light of an elliptical profile. This way we have a single value for the effective radius of elliptical sources and we still preserve information about the aspect ratios and position angles of the sources for future studies.

2.4 Artificial cluster experiments

To test how our selection of stellar cluster candidates (Sect. 2.5) depends on the brightness and size of the cluster and the background region, and how accurate our radius measurements are, we performed tests with artificial clusters for all three filters, different background regions and different cluster sizes. The results of these tests will be used in Sect. 2.5 to select a sample of stellar cluster candidates with accurate radii.

First we created artificial clusters using the MKCMPPSF and MKSYNTH tasks, which are part of the BAOLAB package (Larsen 1999). For every filter we convolved the PSF with a Moffat profile with a power-law index of −1.5 and effective radii between 1 and 9 pc, in steps of 2 pc. These artificial clusters were then scaled to a range of magnitudes between 18 and 26 mag with steps of 0.5 mag. For every magnitude 100 clusters were added at random locations to every background region on the mosaic image by combining MKSYNTH with the IMARITH task in IRAF. We made sure that the minimum distance between these random locations was at least 30 pixels, in order not to introduce artificial crowding effects.

We then performed the cluster selection on these sources in a similar way as with the normal data. We performed these tests for every filter individually, since taking into account the matching of every source in three filters, as we did with the normal data, would imply creating artificial clusters with a range of colours (i.e. ages) for every magnitude, drastically increasing the computing time. However,

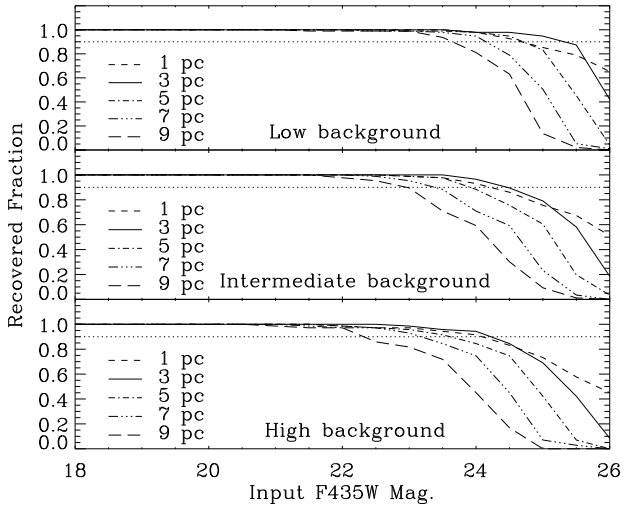

Figure 2.3: The recovered fraction of artificial clusters as a function of magnitude and $R_{\rm eff}$ for the three background regions on the B_{F435W} image (i.e. "completeness profiles"). The horizontal dotted line indicates where 90% completeness is reached. The magnitudes at which the completeness profiles reach this 90% completeness limit are summarised in Fig. 2.4.

by comparing analytical spectral energy distributions (SEDs) from GALEV simple stellar population (SSP) models (Schulz et al. 2002) to the measured detection limits, we tested that for cluster ages up to ~1 Gyr, the I_{F814W} filter is always the most limiting filter for detecting clusters. We therefore do not expect that using the results of these tests for individual filters introduces large age-dependent biases in the derived detection limits.

The artificial clusters were recovered by running SExtractor, followed by photometry in all three filters and by performing size measurements in B_{F435W} and V_{F555W}. For B_{F435W} and V_{F555W}, we considered a cluster to be recovered when we found a resolved source (i.e. with a $R_{\rm eff}$ larger than our adopted lower limit of 0.5 pc (see Sect. 2.5) and a χ^2 which is lower than the χ^2 using only a PSF) within 1 pixel from the input coordinates and with a distance to the nearest neighbouring source of >5 pixels. For I_{F814W} we considered a cluster to be recovered when we found a source within 1 pixel from the input coordinates and with a distance to the nearest neighbouring source of >5 pixels. The recovered fraction as a function of B_{F435W} magnitude for the different background regions and input radii is plotted in Fig. 2.3. For the V_{F555W} and I_{F814W} passbands the results are similar, except that the turn-off of the completeness curves happens at brighter magnitudes due to a lower S/N ratio of the V_{F555W} and I_{F814W} data (see below).

The recovered fraction shown in Fig. 2.3 is scaled to the number of clusters recovered at magnitude 18. We note, however, that a certain fraction of even the

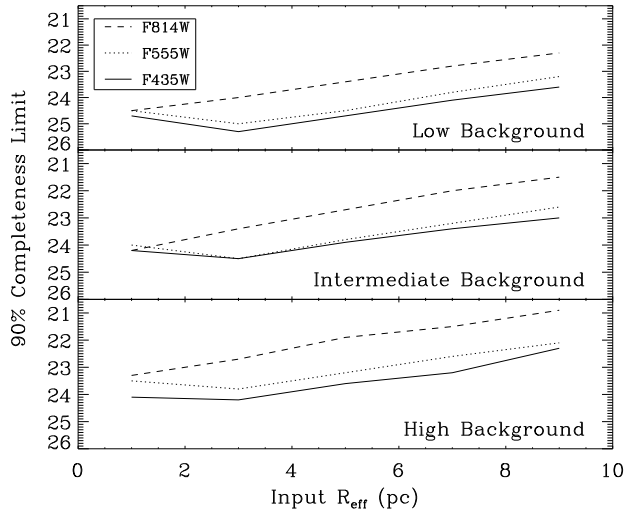

Figure 2.4: The 90% completeness limits versus effective radius ($R_{\rm eff}$), determined for B_{F435W}, V_{F555W} and I_{F814W} for the three background regions.

brightest artificial clusters is not recovered due to their vicinity within 5 pixels from a neighbouring source. Our completeness tests show that these initial losses will be ~3, ~13 and ~28% for the low, intermediate and high background, respectively. This shows that due to crowding effects one can never select a sample which is 100% complete. Depending on the selection criteria and background region, one will lose up to ~28% of the initial sample present in the data. This number will be even higher when one considers that young clusters are not randomly distributed across the spiral disc, but will mostly be clustered themselves in high background regions.

Fig. 2.3 shows that larger clusters are harder to recover than smaller clusters with the same brightness. This is expected, since larger clusters have a lower surface brightness, which makes them easier to blend into the background. We define the magnitude at which 90% of the artificial clusters was recovered to be the 90% completeness limit. The values we found this way for the different filters, cluster sizes and background regions are plotted in Fig. 2.4.

For our current study, where we look at the radius distribution of stellar clusters, it is not only important to detect clusters by measuring their radii, but the measured radii also have to be accurate. To test the limitations of our radius measurements, we looked at how the difference between input and measured radius of the artificial clusters depends on magnitude, input size and background region. In Fig. 2.5 we plot the 50th (i.e. the median), 68th and 90th percentile of δ versus the magnitude in B_{F435W}, where we define δ as the relative difference between input and measured

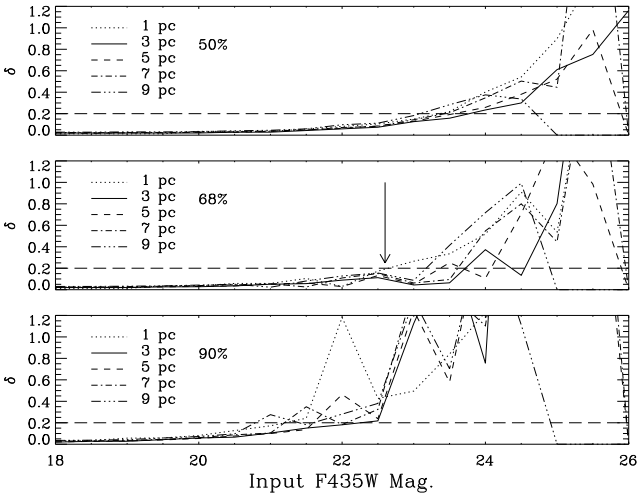

Figure 2.5: The median (top), 68th percentile (middle) and 90th percentile (bottom) of δ (see Eq. 2.3) versus B_{F435W} magnitude for the artificial clusters with different radii in the high background region. Below the horizontal line the uncertainty of the radius measurements is smaller than 20%, which is achieved for more than 68% of the clusters up to $R_{\rm eff}$ = 9 pc brighter than B_{F435W} = 22.6 mag (indicated by the arrow).

radius:

$$\delta \equiv \frac{|R_{\rm eff,in} - R_{\rm eff,out}|}{R_{\rm eff,in}}. \tag{2.3}$$

We note that the pth percentile is the value such that p% of the observations (δ) is less than this value. Fig. 2.5 shows for example, that when we select cluster candidates with $B_{F435W} < 22.6$ mag, ~68% of the sample will have a radius uncertainty smaller than 20%. The figure also indicates that the radius measurements are the most limiting factor in the detection of stellar cluster candidates: at the 90% completeness limit for a 3 pc source (B_{F435W} = 24.2 mag), about 50% of the recovered sources are likely to have inaccuracies in their radii *larger* than 25–40%. Therefore, in Sect. 2.5 we will select magnitude limits in B_{F435W} and V_{F555W} *brighter* than the 90% completeness limits of these passbands. Since we will not use the radius measurements in the I_{F814W} passband, in this passband the 90% completeness limit will be used in the selection of the sample.

We also used the results of our artificial cluster experiments to test the robustness of our photometry and the accuracy of the applied aperture corrections described in Sect. 2.2.5. In Fig. 2.6 we show the mean difference between the measured magnitude and the input magnitude (Δ mag) versus B_{F435W} magnitude for different sizes in the high background region. We applied the constant aperture correction for a 3 pc source according to Eq. 2.1 and the infinity correction for point sources from Sirianni

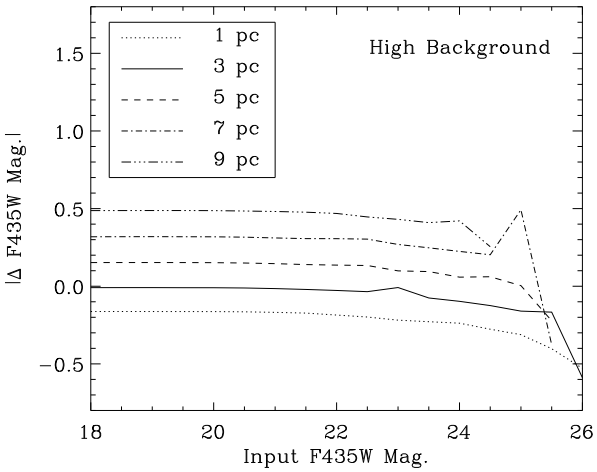

Figure 2.6: The mean difference between the measured magnitude and the input magnitude of the recovered artificial clusters versus B_{F435W} magnitude for different sizes in the high background region. The truncated line for the largest and faintest clusters means none of these artificial clusters were recovered.

et al. (2005) that we described in Sect. 2.2.5. First, Fig. 2.6 shows that the applied aperture correction is very accurate, since the photometry of 3 pc clusters is almost perfectly reproduced to ~22.5 mag. This shows that applying the point source infinity correction to 3 pc sources does not introduce systematic offsets in the photometry. Second, the range covered in Δ mag shows that when there is no information about the radius of the cluster, the uncertainty in the photometry can be as large as ~ 0.5 mag for clusters with radii in the range 1–9 pc.

2.5 Selection of the sample

We used the radius estimates to distinguish the resolved clusters from unresolved objects. In this section we select two different cluster samples: a "resolved sample" with clearly resolved clusters, and a smaller subset from this sample, a "radius sample". The radius sample satisfies extra criteria that make the radii more reliable, and will be used to study the radius distribution (Sect. 2.7) and the correlations between mass, radius and distance (Sect. 2.8). The resolved sample is used in other studies of the luminosity function of stellar clusters in M51 (Gieles et al. 2006b, Haas et al. 2008).

The cluster selection process is hampered by various factors like an irregular background (spiral arms, dust lanes), contaminating background galaxies and crowd-

ing effects which causes many sources to be (partially) blended with neighbouring sources, biasing the radius measurements. We tried to automate the selection of stellar cluster candidates as much as possible, taking into account all these factors. However, it was unavoidable to subject the automatically selected sample to visual inspection, to filter out any remaining contaminants or the stellar cluster candidates of which the radii measurements could not be trusted.

2.5.1 Selection criteria

1. Our first two selection criteria were concerned with the sources actually being resolved. As mentioned in Sect. 2.3, we will use as a lower-limit for the measured $R_{\rm eff}$ a value of 0.5 pc, since below this radius we observe a strong peak of unresolved sources (most likely bright stars). Therefore, our first criterion for the selection of stellar cluster candidates was to select sources with $R_{\rm eff} > 0.5$ pc. We applied this criterion to the radius measurements in both B_{F435W} and V_{F555W}. We did not apply a criterion to the measured radii in I_{F814W}, since that would have restricted our sample too much due to the lower signal-to-noise ratio in this passband.

2. Not only should a stellar cluster candidate be resolved when we fit a Moffat15 profile, but using the profile convolved with the PSF should also result in a better fit than fitting the candidate with the PSF alone. A second criterion was therefore to use the χ^2 of the radius fit using the Moffat15 profile, which should be lower than the χ^2_0 of a fit using only the PSF: $\chi^2/\chi^2_0 < 1$.

After applying these criteria there were still many contaminants in our sample, e.g. patches of high background regions in between dark dust lanes that were detected as a source, background galaxies, blended sources and crowded regions. The following criteria were used to remove contaminants and to select only cluster candidates with accurate radii:

3. Following the results of our artificial cluster experiments, we applied the following magnitude cutoffs to our "radius sample": $B_{F435W} < 22.6$, $V_{F555W} < 22.3$ and $I_{F814W} < 22.7$. The first two limits were chosen according to Fig. 2.5. With these limits for B_{F435W} and V_{F555W}, more than 68% of the artificial clusters with input radii up to 9 pc that were retrieved, had a measured radius better than 20%. In Fig. 2.4 we see that these limits are brighter than the 90% completeness limits in the high background region for sources up to ~8 pc. Since we do not use the radii measurements in I_{F814W}, in this passband the 90% completeness limit for a 3 pc source was applied. For the selection of the larger "resolved sample" we used the 90% completeness limits in all three passbands: $B_{F435W} < 24.2$, $V_{F555W} < 23.8$ and $I_{F814W} < 22.7$.

4. We only selected sources that had an absolute difference in $R_{\rm eff}$ between B_{F435W} and V_{F555W} of less than 2 pc. Tests revealed that mostly all sources in low,

homogeneous background regions already fulfilled this criterion and a check by eye showed that sources which did not pass this criterion were practically all contaminants due to a highly varying local background. We did not apply this size difference criterion for our resolved sample, since sources in this sample do not necessarily have accurate radii measured in both B_{F435W} and V_{F555W}.

5. We used the distance of every source to its nearest neighbouring source as a criterion to filter out unreliable fits due to blending or crowding. A source was rejected if it had a neighbour within 5 pixels (the fitting radius of ISHAPE). Of course this method only works when both neighbouring sources are in the original source list.

6. To select out the remaining blended sources and crowded regions that were initially detected as a single source, we inspected every remaining source in our sample by eye. We realise that this introduces some amount of subjectivity into our sample, but we are dealing with a face-on spiral galaxy with a high degree of irregularities in the background light due to the spiral structure and many crowded star forming regions. Therefore, visual inspection was unavoidable for our purpose of selecting a cluster sample with accurate radii.

   We created small images in all three filters for all sources that fulfilled the above mentioned criteria, and by visual inspection we looked for:

   - the presence of a second, separate peak within a distance of ~5 pixels
   - a very irregular shape
   - very small fitted aspect ratio for sources that appear fairly circular
   - crowded regions
   - very steep gradients in the background light that likely influenced the fitted radius
   - background galaxies

   If, based on one of these points, the source was not a clear cluster candidate with an accurately determined radius, we rejected the source from our sample. In Fig. 2.7 we show a number of sources that were rejected together with the main reason. For comparison we show a number of accepted cluster candidates in Fig. 2.8. Visual inspection removed another 24, 21 and 22% of the sources from our sample in the low, intermediate and high background region, respectively.

In Table 2.2 we summarise the results of our sample selection for the radius sample. Our final *sample of stellar cluster candidates with accurate radii* consists of 1284 sources, of which 57% are located in the high background region and 25% in the low background region. From here on we will refer to this sample of stellar cluster candidates simply as "clusters". The larger sample of *resolved sources*, which does not satisfy the radius difference criterion (criterion 4) and which magnitude cutoffs follow the 90% completeness limits (criterion 3), consists of 7698, 6846 and 5024 sources in B_{F435W}, V_{F555W} and I_{F814W}, respectively. This sample is studied in Haas et al. (2008).

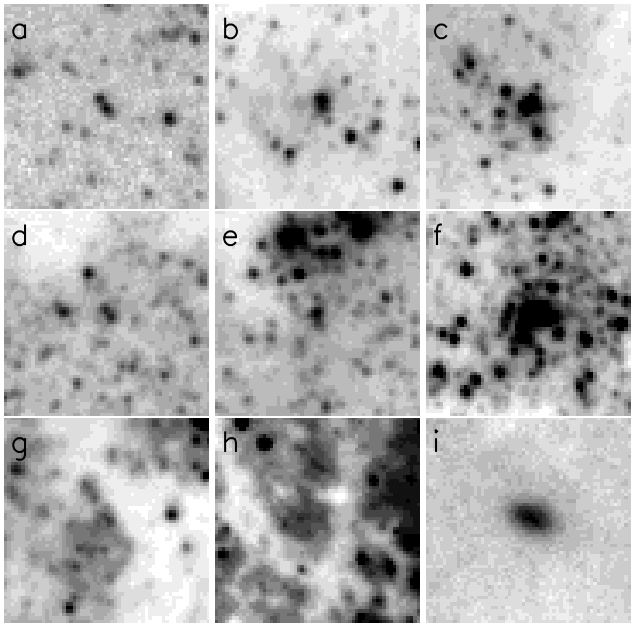

Figure 2.7: A selection of B_{F435W} images centred on sources that were rejected from the sample after visual inspection. The size of each image is 60×60 pixels or 3″×3″. Rejection was based on the following criteria: a. neighbour too close by, b. likely blended, c & d. clearly blended, e. too irregular, f. crowded, g. interfering background, h. radius fit on the background and i. likely a background galaxy.

2.5.2 Old Globular Clusters and Faint Fuzzies

To see if there are any possible old ($\gtrsim$ 10 Gyr) GC candidates in our cluster sample, we applied the colour criteria $B-V > 0.5$ and $V-I > 0.8$ to our cluster sample, typical for old MW GCs. There are only 70 clusters satisfying these criteria, showing that the majority of our cluster sample consists of young clusters, but a small fraction of ∼5% is probably part of an old GC population or highly reddened. A more detailed identification of GC candidates in M51 will be carried out in future studies.

We note that our dataset covers the same field used by Hwang & Lee (2006, from here on referred to as "HL06"), who detect 49 "faint fuzzy" star clusters around the companion of M51, NGC 5195. Faint fuzzy clusters were introduced by Larsen & Richtler (2000), because they formed a subgroup in a radius-colour diagram of star clusters in NGC 1023. In Fig. 2.9 we show $R_{\rm eff}$ versus $V-I$ for the clusters in our sample. Six clusters in our sample satisfy the criteria of a faint fuzzy, namely $0.6 < B-V < 1.1$, $1.0 < V-I < 1.5$ and $R_{\rm eff} > 7$ pc. These faint fuzzy candidates are indicated in Fig. 2.9. The figure shows that the faint fuzzy candidates indeed form a

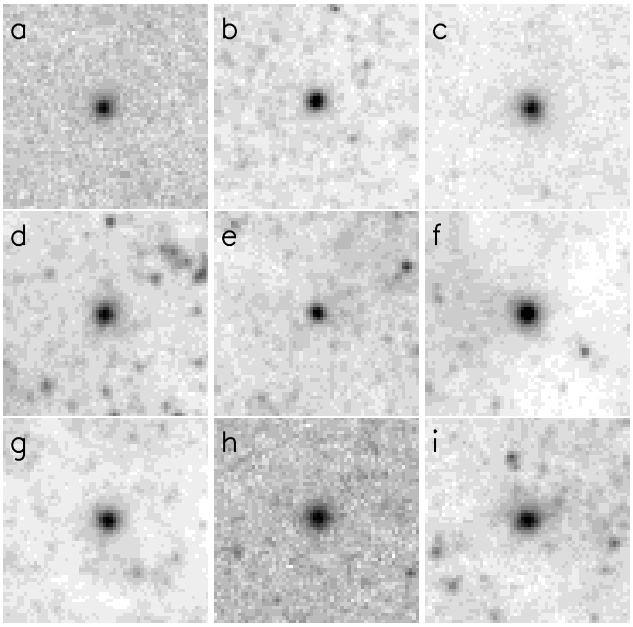

Figure 2.8: A selection of isolated stellar cluster candidates in B_{F435W} that passed the visual inspection. The size of each image is 60×60 pixels or 3″×3″.

Table 2.2: The selection of the sample of stellar cluster candidates with accurate radii. The numbers indicate the amount of sources that satisfy the criterion mentioned and all criteria mentioned above it, split into the low, intermediate and high background region.

Criterion	Nr. remaining		
	low	inter	high
All sources	35 980	15 809	23 647
$R_{\rm eff} > 0.5$ pc	11064	4799	7238
$\chi^2/\chi^2_0 < 1$	10715	4661	7028
$B_{F435W} < 22.5$ mag			
$V_{F555W} < 22.3$ mag	472	346	1301
$I_{F814W} < 22.7$ mag			
$\lvert R_{B_{F435W}} - R_{V_{F555W}} \rvert < 2$ pc	457	327	1068
No neighbour within 5 pixels	418	302	939
After visual inspection	317	239	728
Total sample: 1284			

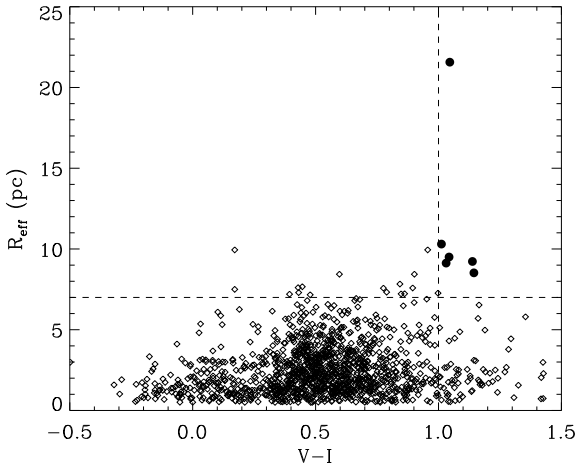

Figure 2.9: $R_{\rm eff}$ versus $V-I$ colour for the total sample of 1284 clusters. The upper-right corner of the dashed lines indicate the region of the sub-group of faint fuzzy candidates (filled circles). These cuts are the same as used by Hwang & Lee (2006) to select faint fuzzy clusters in NGC 5195.

separate group in a radius-colour diagram and are not simply the largest clusters in the tail of a continuous radius distribution.

The six faint fuzzy candidates seem located randomly in (or projected onto) the disc of M51. None of the 49 faint fuzzy candidates of HL06 are therefore recovered in our cluster sample. This is because all these 49 candidates are fainter than the magnitude limits we apply. This is expected, since we apply rather conservative magnitude limits in order to achieve accurate radius measurements, also for large clusters in high background regions (Sect. 2.5.1). If we would drop our conservative magnitude limits from the selection criteria, we would have 37 of the 49 faint fuzzy candidates from HL06 in our sample. The 12 remaining candidates are removed from our sample based on "inaccurate radii" criteria (large radius difference between B_{F435W} and V_{F555W} or a χ^2 larger than χ^2_0). The six faint fuzzy candidates in our sample are not in the sample of HL06, because these authors focused on the region around NGC 5195 and did therefore not cover the disc of M51.

2.5.3 The largest cluster: 212995

One cluster candidate in our radius sample, with our ID number "212995", clearly stands out from the other cluster candidates in radius. The cluster candidate, positioned at RA=$13^{\rm h}29^{\rm m}51\overset{\rm s}{.}94$, Dec=+47°11′19$\overset{''}{.}63$ and shown in Fig. 2.10, has an (ellipticity corrected) $R_{\rm eff}$ = 21.6 pc in B_{F435W}. The projected galactocentric distance of

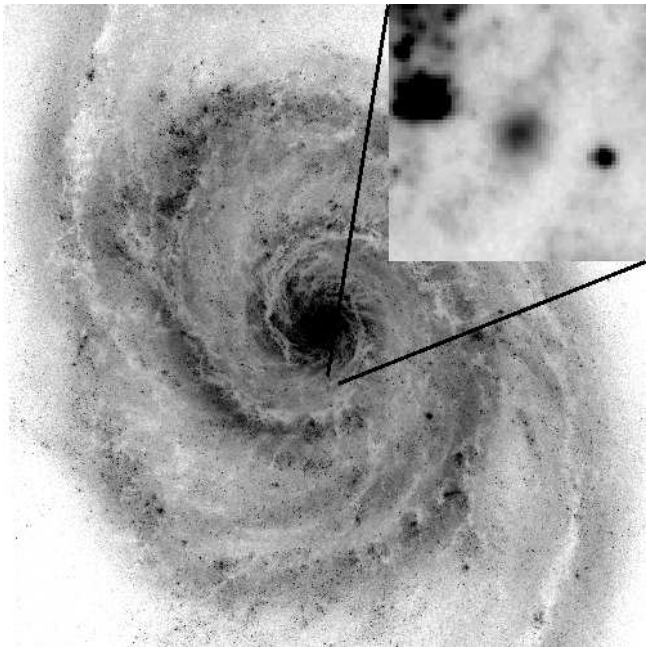

Figure 2.10: Cluster "212995", the largest cluster in our sample with a $R_{\rm eff}$ = 21.6 pc (centre of the inset), and its location in M51 (north is up, east is to the right). The projected galactocentric distance is 1.02 kpc. The scale of the inset image is $\sim 60 \times 60$ pixels or $\sim 122 \times 122$ pc. The scale of the big image is $\sim 16 \times 16$ kpc.

this cluster candidate is 1.02 kpc. Its brightness in B_{F435W}, V_{F555W} and I_{F814W} is 22.27, 21.52 and 20.48 mag, respectively, with corresponding $B-V$ and $V-I$ of 0.75 and 1.05, respectively. These colours make this source both an old GC and faint fuzzy candidate. Assuming the source is a cluster, we can make an estimate of its age and mass by using GALEV SSP models. However, since we only have photometry in three filters, this estimate suffers from an age-extinction-metallicity degeneracy, introducing rather large uncertainties. Assuming a low extinction ($E(B-V) < 0.1$) and a metallicity in the range of 0.2–1.0 $Z_{\odot}$, the best estimate for the age is $2.7^{+2.8}_{-1.8}$ Gyr. The corresponding best estimate for the mass is $2.5^{+3.3}_{-1.1}\times10^5$ $M_{\odot}$, which is a lower limit due to the underestimation of the aperture correction for the photometry for such a large source. Assuming the metallicity is 0.02 $Z_{\odot}$, the best estimates for the age and mass are $13.2^{+2.8}_{-9.7}$ Gyr and $8.0^{+3.5}_{-4.6}\times10^5$ $M_{\odot}$, respectively. However, the possibility of the source being a highly reddened young cluster is not fully excluded. There is also a possibility that this cluster candidate is actually a background galaxy, but this possibility is considered to be unlikely, since the cluster is located (in projection) very close to the centre of M51, where the extinction of the background source and the surface brightness of the foreground (M51) is high.

2.6 A comparison between *ACS* and *WFPC2*

As a test of the robustness of our methods, we compared the photometry and the radii of our clusters to the data of B05. B05 derived ages, masses, extinctions and effective radius estimates of stellar clusters covering the central $\sim 7.3 \times 8.1$ kpc of M51 using *HST NICMOS* and *WFPC2* data. We calculated the transformation between a mosaic of the V_{F555W} *WFPC2* images and the *ACS* mosaic image with the GEOMAP task in IRAF, by identifying 10 sources by eye that were clearly visible in both data sets. We then transformed the coordinates of all clusters in their sample to our *ACS* mosaic frame using the GEOXYTRAN task in IRAF, and we matched sources which were within 1 pixels from a cluster in our sample, which had photometry in B_{F435W} ($\approx B$), V_{F555W} ($\approx V$) and I_{F814W} ($\approx I$) in both data sets and which had a measured radius on the *WFPC2* data $0 < R_{\rm eff} < 12$ pc. This resulted in 271 matched clusters, of which a few will be mismatched due to the uncertainties in the transformation and, most importantly, geometric distortion of the *WFPC2* images.

For these 271 clusters we compared the $B-V$ and $V-I$ colours of B05 with our results, after we removed our filter dependent infinity corrections and Galactic foreground extinction corrections, since these were constant for the photometry of B05. In Fig. 2.11 we plot the difference between the *ACS* and *WFPC2* colours versus the *ACS* colour. For the mean differences we find:

$$\begin{aligned} \Delta(B-V) = (B-V)_{ACS} - (B-V)_{WFPC2} &= -0.005 \pm 0.005 \\ \Delta(V-I) = (V-I)_{ACS} - (V-I)_{WFPC2} &= 0.064 \pm 0.006, \end{aligned}$$

where the errors are the standard errors of the means, not to be confused with the standard deviations, which are 0.076 and 0.098, respectively. This shows that our colours are in good agreement with B05 and that we can adopt the masses derived by B05 for these 271 clusters to study the mass-radius relation with the higher resolution of the *ACS* data in Sect. 2.8.2.

We also compared the effective radii of the 271 matched clusters on the V_{F555W} image. In Fig. 2.12 we show the difference between the *ACS* and *WFPC2* radius versus the *ACS* radius. No clear trend is visible, except that the average *ACS* radius of the clusters is slightly smaller than the *WFPC2* radius. The mean difference between the *ACS* and *WFPC2* radius is

$$R_{{\rm eff},ACS} - R_{{\rm eff},WFPC2} = -0.34 \pm 0.06 \text{ pc},$$

where the error is the standard error of the mean. The standard deviation around the mean is 0.94 pc. We note that some of the differences between *ACS* and *WFPC2* radii are expected to be caused by contaminants in the matching procedure, as well as resolution effects (blends in the *WFPC2* data) and a different treatment of ellipticity for both data sets. For the *WFPC2* data circular cluster profiles were assumed, while for the *ACS* data we used elliptical profiles with a transformation to a single $R_{\rm eff}$. Overall, the mean difference between the *ACS* and *WFPC2* radii is within the expected accuracy of the radius measurements (~ 0.5 pc), and Fig. 2.12 suggests that there are no strong radius dependent biases in our methods.

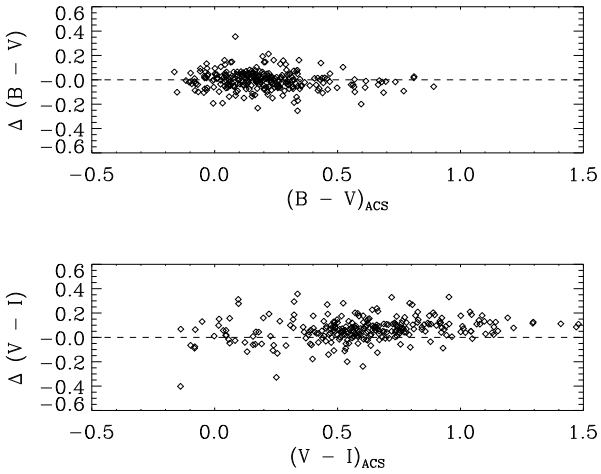

Figure 2.11: The differences between the colours of clusters matched between our *ACS* dataset and the *WFPC2* dataset of Bastian et al. (2005), versus the colour in the *ACS* dataset.The dashed lines show a difference of 0 as a reference for the eye.

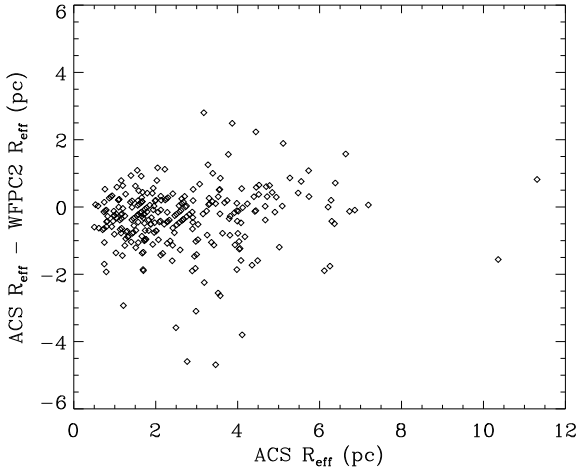

Figure 2.12: The differences between the effective radii of the clusters matched between our *ACS* dataset and the *WFPC2* dataset of Bastian et al. (2005), versus the effective radius in the *ACS* dataset.

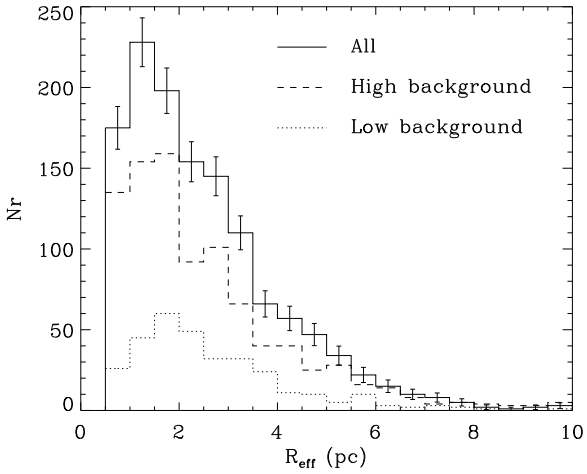

Figure 2.13: The effective radius distribution of the total sample of 1284 clusters, measured on the B_{F435W} image, using linear radius bins (solid line). Also shown are the radius distribution of only the sources in the low background region (dotted line) and the sources in the high background region (dashed line). For better readability, only the (Poissonian) error bars of the total sample are shown.

2.7 The radius distribution

Now that we have selected a sample of clusters with accurate radii, we will study the distribution of their radii and possible dependencies among radius, background region and colour in this section. Possible correlations between radius and luminosity, mass and galactocentric distance will be the subject of the next section.

We show the effective radius distribution[3] of our sample of 1284 clusters with linear bins in Fig. 2.13 and with logarithmic bins in Fig. 2.14. In both figures we plot the radius distributions for clusters in the low and high background region separately. We see that the radius distribution peaks around 1–2 pc and then drops to a maximum radius of ~10 pc. In the remainder of this section we will first focus on the slope of the radius distribution at $R_{\rm eff} > 3$ pc and then focus on the location of the peak.

[3]Strictly speaking, the term *distribution* refers to linear intervals, i.e. $N(R)\mathrm{d}R$, and the term *function* refers to logarithmic intervals, i.e. $N(R)\mathrm{dlog}R$. In this work, however, we will not make this distinction. We will only use the term *distribution* and we will specify the type of interval used when necessary.

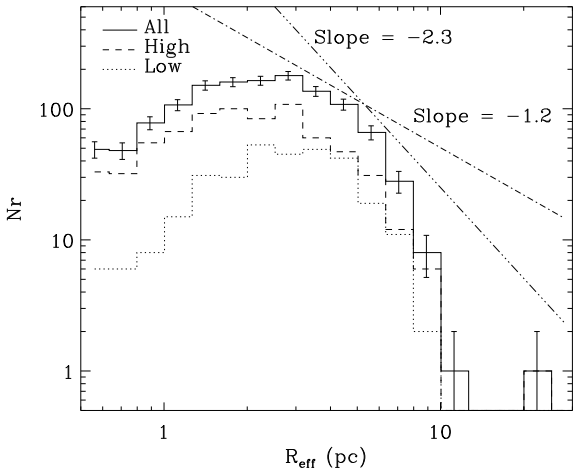

Figure 2.14: The effective radius distribution of the total sample of 1284 clusters, measured on the B_{F435W} image, using logarithmic radius bins (solid line). Also shown are the radius distribution of only the sources in the low background region (dotted line) and the sources in the high background region (dashed line). For better readability, only the (Poissonian) error bars of the total sample are shown. For comparison we also show a power law with a slope of −2.3, typical for a fractal radius distribution of star-forming gas clouds, and a slope of −1.2 as determined by B05 for the radius distribution of 407 star clusters in M51 with *WFPC2* data.

2.7.1 The slope of the radius distribution

It has been observed that the *mass* distributions of both star-forming clouds (Sanders et al. 1985, Solomon et al. 1987, Harris & Pudritz 1994, Brand & Wouterloot 1995, Elmegreen & Falgarone 1996, Fukui et al. 2001) and star clusters (Zhang & Fall 1999, Ashman & Zepf 2001, Bik et al. 2003, de Grijs et al. 2003b, Hunter et al. 2003) can be approximated by power laws of the form $N(M)\mathrm{d}M \propto M^{-\alpha}\mathrm{d}M$, with the index α in the range of 1.5–2.0. Star-forming clouds also show a power-law *radius* distribution of the form $N(R)\mathrm{d}\log R \propto R^{-2.3}\mathrm{d}\log R$ (Harris & Pudritz 1994, Elmegreen & Falgarone 1996). For the clouds, the power-law mass and radius distributions are consistent with the clouds having a fractal structure with a fractal dimension of 2.3 (Mandelbrot 1983, Elmegreen & Elmegreen 2001). Since the mass distribution of clusters is similar to the mass distribution of clouds, one might naively expect the radius distributions also to be similar. We plotted the radius distribution of star clusters in M51 in Fig. 2.14, using logarithmic bins. In this figure a power law would be a straight line. We plotted two lines with a slope of −2.3 and −1.2. The first slope is consistent with the power-law distribution of the form $N(R)\mathrm{d}\log R \propto R^{-2.3}\mathrm{d}\log R$ or $N(R)\mathrm{d}R \propto R^{-3.3}\mathrm{d}R$, observed for star-forming gas clouds on every length scale (down to the smallest scales of $\sim$ 0.1 pc). We see in Fig. 2.14 that the radius distribution of the clusters in

M51 between ~3 and ~10 pc can *not* be approximated by the same power law as the one for the star-forming gas clouds.[4]

The slope of −1.2, indicated in Fig. 2.14, is consistent with the power-law distribution of $N(R)\mathrm{d}R \propto R^{-2.2}\mathrm{d}R$, found by B05 for 407 clusters between 2–15 pc in M51 using *WFPC2* data. Although the slope of our observed radius distribution in the range ~ 3–6 pc is similar to the slope observed by B05, our observed radius distribution is considerably steeper at larger radii. However, we note that we used a larger sample of clusters, measured at twice the resolution and which was checked by visual inspection for contaminants and blends. The cluster sample of B05 is therefore expected to have a larger fraction of contaminants and blends than the current sample. We note however, that the current sample is still biased against clusters in crowded regions, but for the remainder of this study we assume that the current sample is representative of the entire star cluster population of M51.

Fig. 2.14 shows that the radius distribution of star clusters in M51 is not consistent with a fractal structure. This suggests that after the formation of the clusters from a fractal gas, their radii have changed in a non-uniform way. Unfortunately, at the small radius end of the distribution a possible bias against small clusters cannot be completely ruled out, since in a fractal gas the *smallest* clusters are expected to form in groups *closest* together. These small clusters could have been rejected from our sample by the close neighbour criterion (Sect. 2.5). Without this criterion, however, our sample would also be biased against small clusters due to blends. This bias is not expected at the large radius end of the distribution, where the radius distribution of star clusters in M51 is clearly not consistent with a fractal distribution.

The picture in which the radii of the clusters change shortly after their formation is consistent with various suggested explanations for the lack of the mass-radius relation of clusters (see Sect. 2.8.2). One possible explanation is that interactions between young star clusters and gas clouds lead to dynamical heating and therefore expansion of the clusters (e.g. Gieles et al. 2006c). This expansion will be strongest for the largest and least concentrated clusters because of their lower density and it will therefore make an initial power-law distribution more shallow. Although cluster-cloud interactions are probably part of the explanation for the lacking mass-radius relation, on its own this scenario fails to explain the expansion of the smallest clusters, which is necessary to weaken the mass-radius relation.

Another suggested explanation for the weak or missing mass-radius relation of clusters is a star formation efficiency (SFE) which scales with the mass of the clouds (Ashman & Zepf 2001) combined with the early residual gas loss from clusters (Hills 1980, Geyer & Burkert 2001, Goodwin & Bastian 2006). In this scenario the forming clusters initially follow the same mass-radius relation as the clouds. However, the removal of binding energy will lead to the expansion of preferably small clusters, since they form from low-mass clouds which lose relatively more residual gas. On its own, however, this explanation will lead to a steeper radius distribution of clusters compared to clouds, i.e. with a slope < -2.3, contrary to what we observe (Fig. 2.14).

[4]Between 0.5 and ~10 pc a lognormal distribution provides a reasonable fit to the data (not shown here).

Although Fig. 2.14 suggests that the radii of the clusters have changed shortly after their formation, our radius distribution is consistent with neither scenario. Perhaps a scenario including a combination of stochastic cluster-cloud interactions, expansion due to residual gas expulsion and a mass-dependent SFE can change the radius distribution in a way that is more consistent with the observed radius distribution. However, a fundamental problem of the missing mass-radius relation of clusters is that there are also high-mass clusters with *small* radii. The existence of these clusters can not be explained by the scenarios mentioned so far, which all rely on the expansion of clusters. Therefore, we need better scenarios and more insight in cluster formation theory to account for the differences in the radius distributions between clouds and clusters.

2.7.2 The peak of the radius distribution

In Fig. 2.13 we see that there is a peak in the radius distribution around ~1.5 pc. If we assume that the star clusters in M51 formed from a fractal gas, this is consistent with the suggestion of the expansion of preferably the smallest clusters, i.e. clusters with $R_{\rm eff} < 1.5$ pc which expanded to radii >1.5 pc.

Fig. 2.13 and 2.14 also show that the radius distribution of clusters in the low background region (the dotted lines) shows a more pronounced turnover, i.e. there are relatively fewer small clusters in the low background region compared to the high background region. This suggests that generally the smallest clusters are mainly found in the high background regions (e.g. inside the spiral arms). The medians also show this trend: while the median $R_{\rm eff}$ of our complete cluster sample is 2.1 pc, it is 1.9 pc for the high background and 2.7 pc for the low background region.

We stress that it is *not* very likely that this trend is biased due to selection effects, since we applied magnitude limits that are brighter than the 90% completeness limits in the high background region (Sect. 2.4), and visual inspection removed most background galaxies in the low background region and possible blends in the high background region. Also, the more compact clusters are easier to detect, so it is not likely that there is a selection effect against small clusters in the low background regions.

Fig. 2.15 shows the $B-V$ colour distribution of clusters in the low and high background region. The high background region has a higher fraction of blue clusters ($B-V \lesssim 0.05$) than the low background region. This fraction is expected to be higher when extinction is taken into account, since clusters in the high background region are likely more strongly reddened than clusters in the low background region.

Fig. 2.14 and 2.15 suggest that there is a relation between $R_{\rm eff}$ and colour. In Fig. 2.16 we show the radius distribution for 2 equal-sized samples with $B-V < 0.1$ ("blue") and $B-V > 0.1$ ("red"). We indeed see a shift in the radius distribution towards larger radii for our red subsample. The median value follows this shift: for the blue sample the median $R_{\rm eff}$ is 1.8 pc, while for the red sample it is 2.5 pc. In Fig. 2.17 we show the median $R_{\rm eff}$ versus $B-V$ and $V-I$ colour. Because all bins contain an equal number of clusters, size-of-sample effects are excluded. Both for

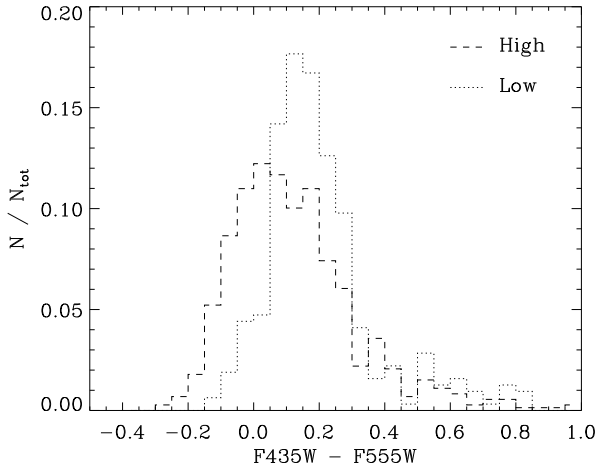

Figure 2.15: The normalised $B-V$ colour distribution for clusters in the low (dotted) and high (dashed) background region. The high background region has a higher fraction of blue clusters than the low background region.

low and high background regions and $B-V$ and $V-I$ colours we see a similar trend of a median $R_{\rm eff}$ increasing with colour, although the scatter is high and the trend is strongest for $B-V$ colours.

Therefore, the observed difference in the radius distribution between low and high background regions can be explained by a higher fraction of red clusters in low background regions, which are generally slightly larger. For young clusters, colours become redder with age. This is consistent with a larger fraction of blue clusters in high background regions, since these regions follow the high density spiral arms, where most clusters are expected to form. If the observed spread in colour is also a spread in the age of the clusters, the slight increase in median $R_{\rm eff}$ with colour in Fig. 2.17 suggests a dynamical evolution of the clusters with age. The fact that the increase in radius is strongest for $B-V$ colours supports this suggestion, because $B-V$ is more sensitive to age than $V-I$.

In this hypothesis, newly formed clusters in spiral arms are generally small, reflecting the high pressure and density of their parental gas clouds. In the subsequent early evolution of the clusters an increase in size is expected, likely due to dynamical heating from cluster-cluster and cluster-cloud encounters and due to the removal of binding energy when the clusters lose mass (Goodwin 1997, Boily & Kroupa 2003). Clusters also expand when moving out of the spiral arm, due to tidal forces from the spiral density wave (Gieles et al. 2007). This hypothesis is consistent with the low background regions containing a relatively larger fraction of older, more evolved

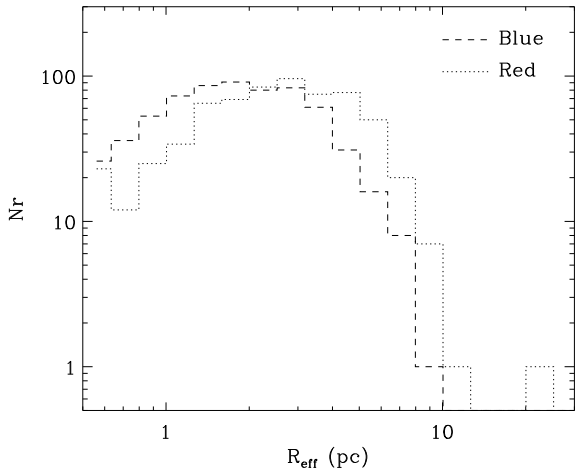

Figure 2.16: The effective radius distribution split in a sample with $B-V < 0.1$ (blue, dashed line, 645 clusters) and $B-V > 0.1$ (red, dotted line, 639 clusters). The radius distribution of the red sample is shifted towards larger radii.

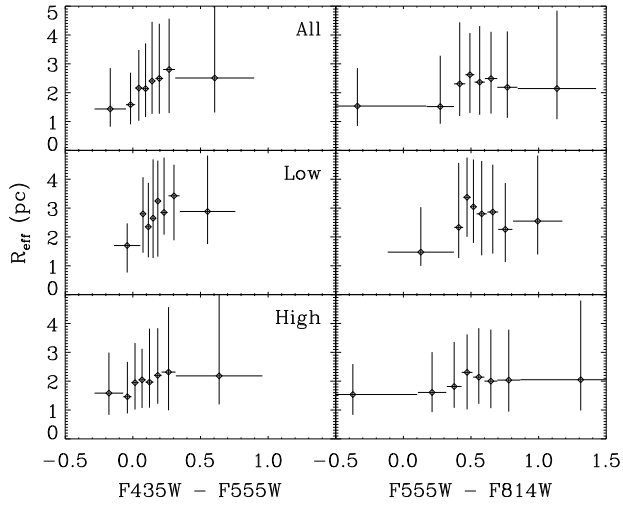

Figure 2.17: The median $R_{\rm eff}$ versus colour for bins containing an equal number of clusters for the complete cluster sample (top) and the low (middle) and high (bottom) background region. The vertical error bars indicate the range in which 68% of the clusters are contained.

clusters with therefore slightly larger radii.[5]

If clusters expand, they will do this on a dynamical (crossing) timescale of a few Myrs (Lada & Lada 2003). The typical timescale for a cluster to move from the high to low background region will be about half the time between 2 spiral arm passages, which for a 2-armed spiral galaxy is

$$\tau(R_{\rm G}) = \frac{\pi R_{\rm G}}{2\left(V_{\rm disc} - \Omega_{\rm p} R_{\rm G}\right)}, \tag{2.4}$$

where $V_{\rm disc}$ is the circular velocity in the disc, $\Omega_{\rm p}$ is the angular pattern speed and $R_{\rm G}$ is the galactocentric distance. For M51 this gives τ(1 kpc) $\approx$ 10 Myr (using V = 200 km s^{-1} (García-Burillo et al. 1993) and $\Omega_{\rm p}$ = 37 km s^{-1}kpc^{-1} (Zimmer et al. 2004)). This is a typical lower-limit for the timescale to move from the high to low background region. For the more average galactocentric distance of 5 kpc, τ(5 kpc) $\approx 5.2 \cdot 10^8$ yr. These timescales are longer than the expansion timescale of the clusters, and are therefore consistent with the low background region containing a considerable number of larger clusters than the high background region, if the clusters started expanding shortly after their formation in a spiral arm.

2.7.3 A radius-age relation?

We have used the 271 matched clusters with an age estimate from B05 to search for a correlation between age and $R_{\rm eff}$. These clusters show a weak relation between radius and age of the form $R_{\rm eff} \propto {\rm age}^{0.08\pm0.03}$, with a large scatter. This is consistent with the relation Lee et al. (2005) observe for clusters in M51 using *WFPC2* data (best fit slope of 0.06 ± 0.02). Fig. 2.18 shows the radius distribution for the matched clusters, split in two equal-sized samples with log(age)<7.5 and log(age)>7.5. The distributions are not very different, although a weak trend is visible since the older sample has slightly more large clusters than the younger sample. However, these differences are within the statistical errors and a K-S test did not give a significant result either (p = 0.126). The median $R_{\rm eff}$ follows a similar trend: the median $R_{\rm eff}$ is 1.8 and 2.2 pc for the younger and older population, respectively.

2.7.4 A comparison with other results

We compared the mean and median $R_{\rm eff}$ of our cluster sample to other work, but we note that these comparisons can easily be biased by differences in the lower limits of the radius and other selection criteria. The mean and median $R_{\rm eff}$ of our total sample are 2.5 and 2.1 pc, respectively. The mean and median $R_{\rm eff}$ of the 70 GC candidates

[5] If one would actually quantify any age-radius relation one needs to be aware of possible biases, due to a slight mass-radius relation or size-of-sample effects. For example at older ages, the low-mass clusters will first fade below the detection limit, so any observed age-radius relation could then result from a possible mass-radius relation. Also, if one would let the absolute age intervals increase with age (i.e. logarithmic binning), one would sample the radius distribution up to larger radii for older ages and the average radius would seem to increase with age.

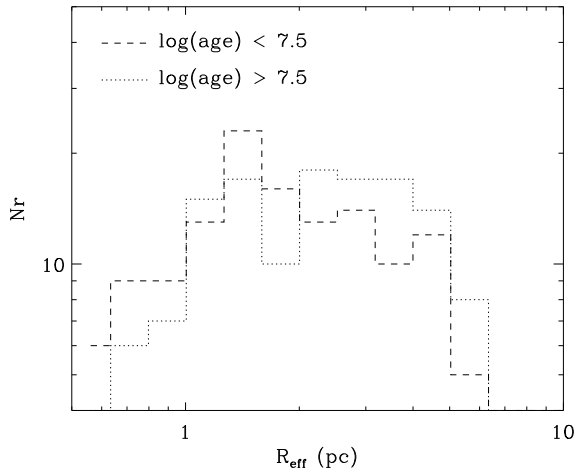

Figure 2.18: The radius distribution of the 271 matched clusters for which we have age estimates from B05, split in a sample with log(age)>7.5 and log(age)<7.5.

in our sample are 3.7 ± 0.4 and 2.4 pc, respectively, where 0.4 is the standard error of the mean (the standard deviation is 3.4 pc). If we restrict ourselves to clusters in the low background regions, the mean and median $R_{\rm eff}$ are 2.9 and 2.7 pc, respectively. This latter value is the same as the mean $R_{\rm eff}$ Jordán et al. (2005) found for thousands of GCs observed in 100 early-type galaxies of the *ACS Virgo Cluster Survey*. Larsen (2004) studied the effective radii of stellar clusters in 18 nearby spiral galaxies using *HST WFPC2* images, and he found a mean $R_{\rm eff}$ of 3.94 ± 0.12 pc. Lee et al. (2005) studied the radii of clusters in M51 using *HST WFPC2* observations covering parts of the mosaic image used in our study, and they found a mean and median $R_{\rm eff}$ of 3.7 and 3.1 pc, respectively. The *ACS* camera has about twice the resolution of the *WFPC2* camera and can therefore detect small clusters more efficiently. This could explain why our mean and median $R_{\rm eff}$ are smaller than the values from Lee et al. (2005). The median $R_{\rm eff}$ for Galactic GCs is ~3.3 pc (Harris 1996), very similar to the value Barmby et al. (2006) found for their sample of blue clusters in M101, namely 3.2 pc. We see that the mean and median values of $R_{\rm eff}$ of our cluster sample are somewhat smaller than what is generally found, although the differences become smaller when we restrict ourselves to the clusters in the low background regions or the GC candidates.

2.8 Correlations between mass, radius and distance

In this section we will combine the effective radii of the clusters with other parameters, such as their galactocentric distance, luminosity and for some clusters their mass. Correlations between these parameters for clusters in M51 have already been studied by B05, using *WFPC2* data of the inner 5 kpc of the disc of M51. We again search for correlations, but now using the *ACS* data out to a galactocentric distance of ∼10 kpc.

2.8.1 Galactocentric distance

For Galactic GCs there is a relation between the distance to the Galactic centre, $R_{\rm G}$, and the half-light diameter $D_{0.5}$, of the form $D_{0.5} \propto R_{\rm G}^{1/2}$ (Van den Bergh et al. 1991). This same trend is observed for the core radii of old clusters in the LMC (Hodge 1962, Mateo 1987) and for the sizes of old GCs in NGC 5128 (Hesser et al. 1984). However, these cluster populations are all old and mainly reside in the outer regions or halo of their host galaxies, while we are studying a population of mostly young clusters in a disc.

For the GCs, different explanations for the observed relation between radius and galactocentric distance have been suggested. One possibility could be that the sizes of GCs reflect the densities of the gas clouds from which they formed, i.e. compact GCs preferentially formed from dense gas clouds near the centres of galaxies, while larger GCs preferentially formed in the less dense halo regions (Van den Bergh et al. 1991). Harris & Pudritz (1994) use the Ebert-Bonnor relations (Ebert 1955, Bonnor 1956) to show that

$$R_{\rm GMC} \propto M_{\rm GMC}^{1/2} P_s^{-1/4}, \tag{2.5}$$

where $R_{\rm GMC}$, $M_{\rm GMC}$ and P_s are the radius, mass and surface pressure of the gas clouds, respectively. The Van den Bergh relation then arises naturally if the clusters form from gas clouds of which the surface pressure scales with the ISM pressure ($P_s \approx 5$–$10 P_{ISM}$), which in turn scales as

$$P_{ISM} \propto R_{\rm G}^{-2} \tag{2.6}$$

for the halo region (Harris & Pudritz 1994). From Eq. 2.5 and 2.6 and the observation that the mean GC mass does not change with galactocentric distance (Harris & Pudritz 1994), the Van den Bergh relation follows. However, models like these assume that the relations with surface pressure are also valid in the cloud cores, where the clusters actually form, but this assumption is not necessarily valid.

Another possible explanation for the observed relation between radius and galactocentric distance for GCs is more evolutionary in nature. It assumes that the GCs have reached tidal equilibrium with their host galaxy. The tidal radius of a cluster in an external logarithmic potential field scales as:

$$r_{\rm t} \propto M_{\rm cl}^{1/3} R_{\rm G}^{2/3}, \tag{2.7}$$

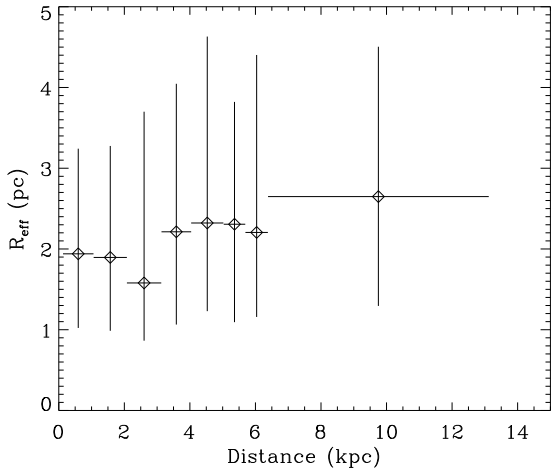

Figure 2.19: The median $R_{\rm eff}$ versus galactocentric distance, for bins containing an equal number of clusters. The vertical error bars indicate the range in which 68% of the clusters are contained.

where $M_{\rm cl}$ is the cluster mass (Binney & Tremaine 1987, chap. 7.3). Thus, when a cluster is relaxed, in tidal equilibrium with its host galaxy and filling its Roche lobe, its tidal radius is expected to scale as $r_{\rm t} \propto R_{\rm G}^{2/3}$. We would also expect the effective radius to scale as $R_{\rm eff} \propto R_{\rm G}^{2/3}$, *only* if the density profile of the cluster would be constant and if the cluster is in tidal equilibrium with the galaxy. For young clusters in the disc, however, the validity of these assumptions remains to be seen.

In Fig. 2.19 we show the median $R_{\rm eff}$ versus the galactocentric distance for the clusters in M51. There seems to be a slight increase in $R_{\rm eff}$ with distance, but the scatter is large (reflected in the large error bars). We have tried to fit a function of the form

$$\frac{R_{\rm eff}}{1\ {\rm pc}} = c \cdot \left(\frac{R_{\rm G}}{1\ {\rm kpc}} \right)^{\alpha} \tag{2.8}$$

to the unbinned data, in which c is a constant, and for the best fit we find $\alpha = 0.12 \pm 0.02$. This relation is significantly weaker than the predicted $\alpha = 0.67$ (for GCs in tidal equilibrium) or the observed relation for Galactic GCs ($\alpha = 0.5$).

The radius distribution changes for different galactocentric distance bins, as shown in Fig. 2.20. The radius distribution close to the centre of M51 (distance < 3 kpc) is shifted towards smaller radii compared to the radius distributions at larger distances. A K-S test confirmed that it is unlikely ($p < 0.001$) that the radius distribution for distance < 3 kpc and > 5.5 kpc are drawn from the same parent distribution.

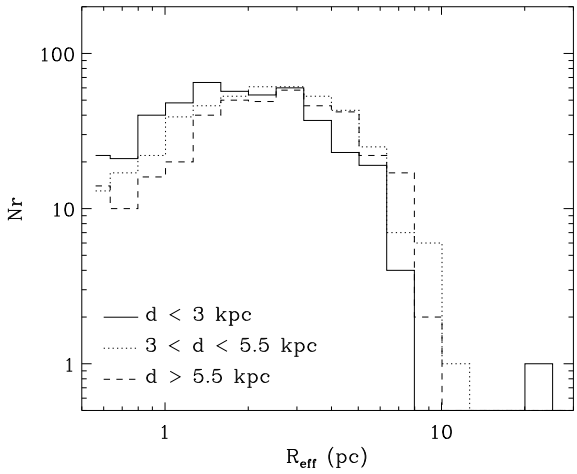

Figure 2.20: The effective radius distributions for three different galactocentric distance regions in M51. The solid line shows clusters close to the centre of M51 (distance < 3 kpc), the dotted line shows clusters at intermediate distances (3< distance <5.5 kpc) and the dashed line shows clusters at large galactocentric distances (> 5.5 kpc). The changes in the distributions are consistent with a slight increase in $R_{\rm eff}$ with distance.

Since we observe a relation between $R_{\rm eff}$ and colour (Fig.2.17), any increase in radius with galactocentric distance could be the result of an increase in colour with galactocentric distance. In Fig. 2.21 we show $B-V$ versus galactocentric distance for the 1284 clusters that were also shown in Fig. 2.19. No obvious trend is visible, which is expected since at all galactocentric radii we encounter clusters in both arm and interarm regions. The arm regions are mostly high background regions and will therefore contain mostly blue clusters, while the interarm regions are mostly low background regions and will therefore contain mostly red clusters (Fig 2.15). The observed $R_{\rm eff} \propto R_{\rm G}^{0.12\pm0.02}$ is therefore not likely a result of the relation between radius and colour.

B05 did not find a relation between $R_{\rm eff}$ and $R_{\rm G}$ for $R_{\rm G} < 5$ kpc. For $R_{\rm G} \lesssim 13$ kpc we find a weak relation, but this relation is considerably weaker than the observed relations for old GCs. Therefore, the clusters we observe in the disc of M51 are either forming under different conditions than the GCs, or the observed relation for GCs emerged during their longer dynamical evolution. We consider the first explanation to be the most likely one, since GCs probably formed outside a spiral disc, in regions where the surface pressure of their parental clouds decreased with distance (Eq. 2.6). For clusters in spiral arms it is not expected that the surface pressure scales in a similar way with distance. Likely, the higher pressure inside spiral arms decreases less strongly with galactocentric distance. Rix & Rieke (1993) find that

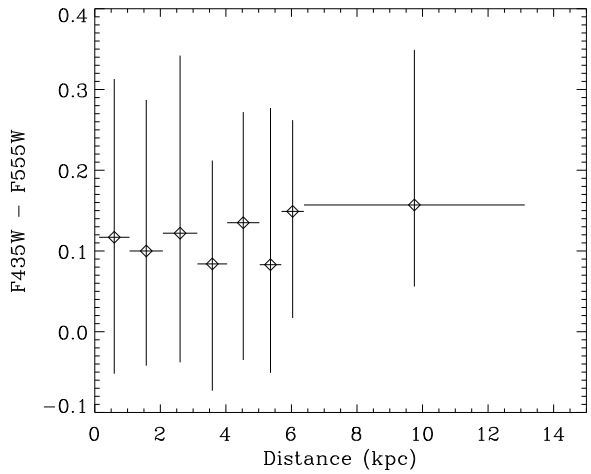

Figure 2.21: The median $B-V$ colour versus galactocentric distance of the 1284 clusters in our sample for bins containing an equal number of clusters. The vertical error bars indicate the range in which 68% of the clusters are contained. No obvious trend is visible in the data.

the arm/interarm density contrast for M51 increases with galactocentric distance, consistent with this picture. In this case a strong radius-distance correlation for the clusters is not expected.

2.8.2 Mass-radius relation

One of the most peculiar properties of star clusters is the lack of a clear relation between their mass and radius. Star clusters are believed to form from Giant Molecular Clouds (GMCs), for which a clear relation between mass and radius is observed. Larson (1981) finds that the internal velocity dispersion of GMCs, σ, scales with their size, $R_{\rm GMC}$, as $\sigma \propto R_{\rm GMC}^{0.38}$. Assuming the GMCs are in virial equilibrium, this leads to a mass-radius relation of the form $R_{\rm GMC} \propto M_{\rm GMC}^{0.57}$. Also assuming virial equilibrium, Solomon et al. (1987) find $R_{\rm GMC} = 1/540 \cdot M_{\rm GMC}^{0.5}$. These observations are consistent with GMCs having a constant surface density ($\Sigma \equiv M_{\rm GMC}/\pi R_{\rm GMC}^2$).

From the Ebert-Bonnor relations for pressure bounded, self-gravitating, isothermal spheres (Ebert 1955, Bonnor 1956), both Eq. 2.5 as well as:

$$\Sigma \propto P_s^{1/2} \tag{2.9}$$

can be derived, in which P_s is the surface pressure (Harris & Pudritz 1994, Ashman & Zepf 2001). So the observed mass-radius relation and constant surface density for clouds are expected if the surface pressure is constant (Elmegreen 1989).

When clusters emerge from GMCs, the mass-radius relation appears to be erased, indicating that high-mass clusters have higher stellar densities than low-mass clusters. A *constant* stellar density would predict $R_{\rm eff} \propto M_{\rm cl}^{1/3}$, which is not observed. Zepf et al. (1999) find $R_{\rm eff} \propto L^{0.07}$ for young clusters in NGC 3256, where L is the luminosity of the cluster which scales directly with the mass (since their cluster sample suggests that colour is independent of luminosity and therefore they assume that the mass-to-light ratio is mostly independent of luminosity). For clusters in a sample of (non-interacting) spiral galaxies, Larsen (2004) finds $R_{\rm eff} \propto M_{\rm cl}^{0.10\pm0.03}$. The effective radius of the old Galactic GCs also does not seem to correlate with their luminosity and thus their mass (Van den Bergh et al. 1991). Mackey & Gilmore (2003) report that for a sample of 53 rich LMC clusters, there seems to be no strong correlation between their mass and core radius, either.

In Fig. 2.22 we show $R_{\rm eff}$ versus magnitude in B_{F435W} for the M51 clusters, split into the low and high background region. For these clusters we do not have mass estimates. However, it is expected that the age range for the largest fraction of this cluster sample is not very large, because most clusters are blue and located in the spiral arms. Many clusters are therefore expected to have similar mass-to-light ratios and therefore any mass-radius relation should also be visible as a relation between magnitude and radius. Fig. 2.22 shows that clusters in the high background regions show a slight trend of radius decreasing with luminosity. Clusters in the low background regions show a less obvious trend, although the median $R_{\rm eff}$ of the brightest bin is considerably larger, especially compared to the brightest bin in the high background region. A fit to the unbinned data points of the form $R_{\rm eff} \propto L^x$, with L the luminosity in the B_{F435W} passband, resulted in $x = 0.15 \pm 0.02$ and $x = -0.11 \pm 0.01$ for the low and high background region, respectively. We verified that applying the size-dependent aperture correction of Eq. 2.1, instead of the constant aperture correction for a 3 pc source (Sect. 2.2.5), would not change this result considerably ($x = 0.13 \pm 0.02$ and $x = -0.10 \pm 0.01$ for the low and high background, respectively).

It is *not* likely that this observed difference in power-law indices is a bias due to our detection limits, since we use magnitude limits (Sect. 2.5.1) brighter than the 90% completeness limits for ∼8 pc sources in the high background regions. Due to the lack of age estimates of these clusters, there is a degeneracy between age and mass. Therefore it is not certain if any evolution in $R_{\rm eff}$ with luminosity is mainly caused by age effects, mass effects, or a combination of both. More measurements of the ages and masses of clusters which also have accurate radii estimates are necessary to break this age/mass degeneracy (e.g. through additional *U*-band imaging).

Using the 271 clusters that were matched with the cluster sample of B05 and for which we therefore have mass estimates, we show $R_{\rm eff}$ versus mass in Fig. 2.23. No apparent relation is visible. This sample is too small to make a distinction between clusters in low and high background regions, since it mostly covers the inner high background regions of M51.

We conclude that *we do not find evidence for any direct relation between mass and radius of the clusters*, although we find weak relations between luminosity and radius, changing with background region. The suggested explanations for a lacking mass-

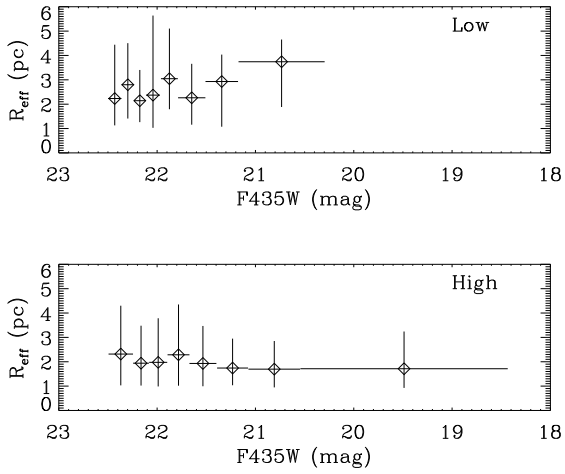

Figure 2.22: The median $R_{\rm eff}$ versus B_{F435W} magnitude for our sample of 317 clusters in the low background region (*top*) and for our sample of 728 clusters in the high background region (*bottom*). The bins contain an equal number of clusters and the vertical error bars indicate the range in which 68% of the clusters is contained.

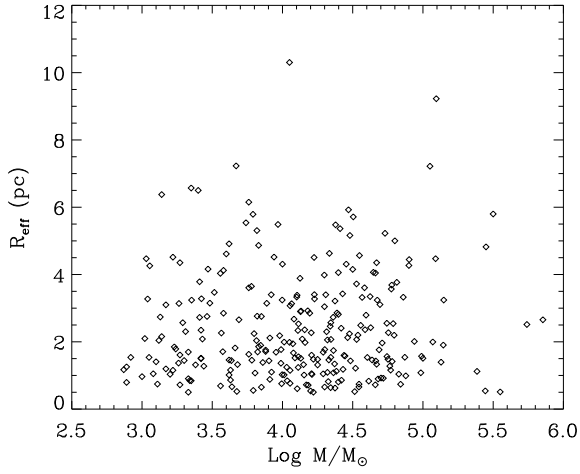

Figure 2.23: $R_{\rm eff}$ versus mass for the 271 clusters that were matched with the cluster sample of B05.

radius relation were already mentioned in Sect. 2.7.1, but we stress again that none of these scenarios are currently capable of explaining the observed differences in the radius distributions between clouds and clusters.

2.9 Summary and conclusions

We have used the *HST ACS* mosaic image of M51 to detect 7698, 6846 and 5024 stellar clusters across the spiral disc in B_{F435W}, V_{F555W} and I_{F814W} respectively, based on effective radius ($R_{\rm eff}$) measurements. We presented the dataset and described the methods used to select our cluster sample, including tests with artificial clusters to show the accuracy, limits and robustness of our methods. We divided the data into 3 regions with respectively a low, intermediate and high background, where the high background traces the spiral arms. We selected a sample of 1284 clusters with the most accurate radius estimates to study the radius distribution and relations between radius, mass, luminosity, galactocentric distance and background region. From these studies we conclude the following:

1. The effective radii of the clusters are distributed between our fixed lower limit of 0.5 pc and ~10 pc (Fig. 2.13). The mean and median $R_{\rm eff}$ of our accurate radii sample are 2.5 and 2.1 pc, respectively. This is smaller than what is generally found for young clusters in spiral galaxies.

2. The radius distribution of clusters in M51 cannot be fitted with a power law similar as the one for star-forming gas clouds. This suggests that shortly after the formation of the clusters from a fractal gas, their radii have changed in a non-uniform way.

3. 70 clusters in our sample satisfy the colour criteria for being old GCs. These clusters are slightly larger than the rest of the cluster sample (median $R_{\rm eff}$ = 2.4 pc). We find 6 clusters in our sample satisfying the criteria for being "faint fuzzy" star clusters projected onto the disc of M51 (Fig. 2.9).

4. The largest cluster in our sample has $R_{\rm eff}$ = 21.6 pc and a projected galactocentric distance of 1.02 kpc (Fig. 2.10). Assuming low extinction and metallicity ($E(B-V) < 0.1$, Z = 0.2–1.0 $Z_\odot$), we estimate its age to be $2.7^{+2.8}_{-1.8}$ Gyr and its mass to be $2.5^{+3.3}_{-1.1}\times10^5$ $M_\odot$. Assuming extremely low metallicity (0.02 $Z_\odot$) results in $13.2^{+2.8}_{-9.7}$ Gyr and $8.0^{+3.5}_{-4.6}\times10^5$ $M_\odot$, for its age and mass, respectively.

5. Comparing clusters in the low and high background regions, we find that the high background regions, i.e. the spiral arms, have a higher fraction of blue clusters, consistent with the idea that these regions are the preferred formation sites for clusters (Fig. 2.15).

6. We detect an increase in $R_{\rm eff}$ with colour, most strongly for $B-V$. Since we detect most of the redder clusters outside the spiral arms, the median $R_{\rm eff}$

outside the spiral arms is larger than inside the spiral arms: 2.7 and 1.9 pc, respectively. The radius distribution of clusters in the low background region also shows a more pronounced turnover around 1.5 pc (Fig. 2.13). We speculate that if the observed spread in colour is also a spread in the ages of the clusters, this observation suggests a dynamical expansion of the clusters with age. In this hypothesis, newly formed clusters in spiral arms are generally small, their radii reflecting the high surrounding pressure of the parental gas clouds. In the subsequent early evolution of the clusters an increase in size is expected, likely due to dynamical heating from cluster-cluster and cluster-cloud encounters and due to the removal of binding energy when the clusters lose mass.

7. We do not observe a strong correlation between $R_{\rm eff}$ and galactocentric distance for the clusters in the disc of M51 out to ~13 kpc. A weak trend is visible of the form $R_{\rm eff} \propto R_{\rm G}^{0.12\pm0.02}$, but the scatter is large. For old GCs, mainly residing in the outer regions or halo of other galaxies, a steeper relation is observed, possibly caused by the decreasing pressure of their parental gas clouds with galactocentric distance. The weaker relation for the clusters in M51 could be explained by the observation that most of the clusters reside in the spiral arms. Since the spiral arms are expected to have a higher pressure and they extend out to large galactocentric distances, a strong radius-distance correlation is not expected.

8. We do not observe a correlation between cluster mass and radius for the 271 clusters of which we have mass estimates. We find weak relations between cluster luminosity and radius for our sample of 1284 clusters. If fitted with a power law of the form $R_{\rm eff} \propto L^x$, we find $x = 0.15 \pm 0.02$ and $x = -0.11 \pm 0.01$ for the low and high background region, respectively (Fig. 2.22). Explanations of the lack of a strong mass-radius or luminosity-radius relation probably need to be sought in the early dynamical evolution (expansion) of the clusters just after their formation. Current scenarios which focus on the expansion of clusters due to either dynamical heating or the removal of binding energy due to gas expulsion are not consistent with the observed differences in the radius distributions between clouds and clusters.

Acknowledgements We thank Peter Anders for useful discussions, tips and comments. We also thank Marcelo Mora at ESO/Garching for discussions and for kindly providing us with the empirical PSFs. We would like to thank Max Mutchler, Richard Hook and Andrew Fruchter for discussions regarding the effects of the drizzle routine on the PSF. We thank Narae Hwang for kindly providing us with the list of faint fuzzies around NGC 5195.

Chapter 3

A peculiar object in M51: fuzzy star cluster or a background galaxy?

R. A. Scheepmaker, H. J. G. L. M. Lamers, S. S. Larsen, and P. Anders

Astronomy & Astrophysics v.477, p.117-123 (2008)

Abstract *Aims.* We study a peculiar object with a projected position close to the nucleus of M51. It is unusually large for a star cluster in M51 and we therefore investigate the three most likely options to explain this object: (a) a background galaxy, (b) a cluster in the disc of M51 and (c) a cluster in M51, but in front of the disc. *Methods.* We use broad-band images of the Advanced Camera for Surveys and the Near Infrared Camera and Multi-Object Spectrometer, both on board the *Hubble Space Telescope*, to study the properties of this object. Assuming the object is a star cluster, we fit the metallicity, age, mass and extinction using simple stellar population models. Assuming the object is a background galaxy, we estimate the extinction from the colour of the background around the object. We study the structural parameters of the object by fitting the spatial profile with analytical models. *Results.* We find de-reddened colours of the object which are bluer than expected for a typical elliptical galaxy, and the central surface brightness is brighter than the typical surface brightness of a disc galaxy. It is therefore not likely that the object is a background galaxy. Assuming the object is a star cluster in the disc of M51, we estimate an age and mass of $0.7^{+0.1}_{-0.1}$ Gyr and $2.2^{+0.3}_{-0.3} \times 10^5\ M_\odot$, respectively (with the extinction fixed to $E(B-V) = 0.2$). Considering the large size of the object, we argue that in this scenario we observe the cluster just prior to final dissolution. If we fit the extinction as a free parameter, a younger age is allowed and the object is not close to

final dissolution. Alternatively, the object could be a star cluster in M51, but in front of the disc, with an age of $1.4^{+0.5}_{-0.2}$ Gyr, mass $M = 1.7^{+0.8}_{-0.3} \times 10^5\ M_\odot$. Its effective radius is between ~12–25 pc. This makes the object a "fuzzy star cluster", raising the issue of how an object of this age would end up outside the disc.

3.1 Introduction

Recently, Scheepmaker et al. (2007, Chapter 2 in this thesis) studied the effective (half-light) radii of 1284 star clusters in the disc of M51. The largest cluster candidate in their sample, carrying their ID number "212995", is remarkable in several ways.

If the object is a cluster in the disc of M51, it is exceptionally large, with an estimated effective radius of 21.6 pc, and located at a galactocentric distance of 1 kpc in a region with many dust lanes. A cluster with this size and galactocentric distance is not expected to survive for long in the spiral disc, where the disruptive effects of the tidal field and other external perturbations (spiral arms, GMCs) are large (Gieles et al. 2005, Gieles et al. 2006c). If the cluster candidate is indeed in the disc, it should therefore be young and highly reddened to account for its observed colours of $B-V = 0.75$ and $V-I = 1.05$. Using only 2 colours, however, Scheepmaker et al. (2007) could not accurately determine an age and extinction.

Observations of HII regions in the disc of M51 show that the metallicity of the gas is approximately solar to twice solar (Diaz et al. 1991, Hill et al. 1997). If the object is in the disc of M51, we would therefore expect its metallicity to be around solar. Outside of the disc, the metallicity could be lower.

There is also the possibility that the object is a background galaxy. The observed colours of the object are similar to the colours of typical background galaxies, but this suggests that the reddening through the disc of M51 is negligible. This would be quite remarkable at a distance of 1 kpc from the nucleus, where the extinction is expected to be high, as suggested by the presence of numerous dust lanes. The hypothesis of a background galaxy therefore suggests a chance alignment, such that the object is observed through a "hole" in a region of the disc with many dust lanes.

In this chapter we present a more detailed study of the nature of the object by extending the data with archival *HST*/*NICMOS* observations in J_{F110W} and H_{F160W}, and by estimating the extinction of the object. Having better constraints on the intrinsic spectral energy distribution of the object, we compare the two hypotheses, of the object being a star cluster or a background galaxy, in a quantitative way.

3.2 Observations and photometry

3.2.1 Observations

We make use of the *HST*/*ACS* dataset in the B_{F435W}, V_{F555W} and I_{F814W} bands of M51 (NGC 5194). These data were taken as part of the Hubble Heritage Project in January 2005 under proposal ID 10452 (PI: S. V. W. Beckwith). We also used *HST*/*NICMOS*

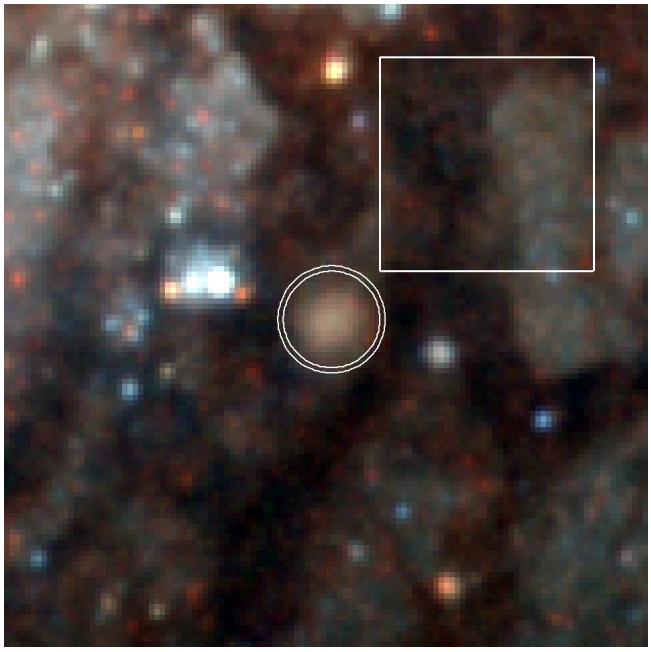

Figure 3.1: Composite image of 120×120 pixels centred on the peculiar object "212995", using the B_{F435W}, V_{F555W} and I_{F814W} bands. The two rings have a radius of 9 and 10 pixels, respectively. The box shows the 40×40 pixel region used for estimating the intrinsic colour of the background.

(NIC3) observations in the J_{F110W} and H_{F160W} bands from the archives (proposal ID 7237, PI: N. Scoville). The *ACS* dataset is described in more detail in Mutchler et al. (2005) and Scheepmaker et al. (2007). For the *NICMOS* dataset, we refer to Bastian et al. (2005b).

Scheepmaker et al. (2007) located the peculiar object (carrying their ID number 212995) at RA=$13^{\rm h}29^{\rm m}51\overset{\rm s}{.}94$, Dec=$+47^\circ11'19\overset{''}{.}63$. An image of a 120×120 pixel region centred on the object is shown in Fig. 3.1, showing that the object is positioned in between two dark dust lanes.

Scheepmaker et al. (2007) used the *ACS* data to perform aperture photometry on the object. Their settings and aperture corrections were, however, optimised for star clusters with an effective radius of ~3 pc. We discuss new aperture photometry on the object in Sect. 3.2.2, taking into account the larger size of the object and its position in between the dust lanes.

The effective radius of 21.6 pc was measured by Scheepmaker et al. (2007), who used the ISHAPE routine (Larsen 1999, 2004) to convolve analytic surface brightness profiles with the point spread function (PSF). EFF (or Moffat) profiles with a power-law index of -1.5 were used (i.e. EFF15 profiles), because these were found to be

the best-fitting profiles for young stellar clusters in the LMC (Elson et al. 1987). However, no tests were performed to find the best-fitting surface brightness profile for our specific object. We describe new fits to the surface brightness profile in Sect. 3.4, also using different analytic profiles.

3.2.2 Photometry

We performed aperture photometry on the object using the IRAF[1]/DAOPHOT package. For the *ACS* data an aperture with a radius of 8 pixels (0.4″) was used, and for the background annulus we adopted an inner radius of 9 pixels and a width of 1 pixel. This annulus is indicated in Fig. 3.1. Zero points in the VEGAmag system were taken from the *ACS* website. There is a possibility that the background annulus contains a small fraction of light from the object. However, this will leave the colours of the object, and therefore our results, largely unaffected, except for the value of the mass (Sect. 3.5.2), which will be a lower limit.

For the *NICMOS* data we used an aperture with a radius of 2 pixels (0.4″) and a background annulus with an inner radius of 2 pixels and a width of 1 pixel. These values are consistent with the aperture of the *ACS* photometry. The magnitudes in the VEGAmag system were determined from the PHOTFNU values from the header, and the bandpass averaged flux densities for Vega from the on-line photometric keyword tables.

No aperture corrections were applied, since these are not well defined for an extended object of which the nature is not well known. However, the aperture was chosen to be as large as possible to minimise any systematic errors. Not applying any aperture correction will not change the colour of the objects significantly (assuming there are no colour gradients), since Scheepmaker et al. (2007) and Bastian et al. (2005b) have shown that the aperture corrections are practically the same for the different filters we use.

To facilitate reading, we will sometimes refer to the *HST* filters using the extended Johnson-Cousin notation (BVIJH), although we note that *no* transformations to this system have been applied. The results of the photometry are listed in Table 3.1.

3.3 Extinction

We have corrected the aperture photometry for Galactic foreground extinction according to Appendix B of Schlegel et al. (1998). Since the object is located in projection close to the nucleus of M51 (R_G = 1.02 kpc), there is possibly a significant amount of additional extinction caused by the ISM of M51. We used two methods to estimate this additional extinction of the object. We note that from here on, all quoted pho-

[1]The Image Reduction and Analysis Facility (IRAF) is distributed by the National Optical Astronomy Observatories, which are operated by the Association of Universities for Research in Astronomy, Inc., under cooperative agreement with the National Science Foundation.

Table 3.1: Results of the aperture photometry, corrected for Galactic foreground extinction.

Filter	Magnitude (VEGAmag)
B_{F435W} ($\sim B$)	22.13
V_{F555W} ($\sim V$)	21.50
I_{F814W} ($\sim I$)	20.49
J_{F110W} ($\sim J$)	20.08
H_{F160W} ($\sim H$)	19.26

tometric values are already corrected for Galactic extinction, and any extinction we will mention refers to the additional extinction at the location of the object in M51.

3.3.1 Extinction from cluster models

The first method used to estimate the extinction assumes that the object is a star cluster, so we use cluster models to fit the extinction based on broad-band colours. We used the GALEV simple stellar population (SSP) models (Anders & Fritze-v. Alvensleven 2003) together with the ANALYSED code (Anders et al. 2004) to simultaneously fit the extinction, metallicity, age and mass of the cluster, based on our broad-band photometry in the B_{F435W}, V_{F555W}, I_{F814W}, J_{F110W} and H_{F160W} bands. The Cardelli et al. (1989) standard extinction law was used ($R_V = 3.1$). Table 3.4 shows the results for different initial constraints on the metallicity, which will be discussed in more detail in Sect. 3.5.2. These results are consistent with $E(B-V) \leq 0.7$, with a best-fitting $E(B-V)$ of 0.1. The resulting ages and masses from these fits will be discussed in Sect. 3.5.2.

3.3.2 Extinction from background colour

The second method used to estimate the extinction of the object is based on comparing the average colour of a background annulus around the object to the intrinsic colour of the local background. The advantage of this method is that we do not have to assume the nature of the object (background galaxy or star cluster) a priori. However, the local background might not be smooth, but could show intrinsic colour variations. The intrinsic colour of the background is therefore not well defined and this method can therefore only provide a rough estimate of the extinction.

For the average observed colour of the background around the object we used the same annulus as we used for the aperture photometry (i.e. an inner radius of 9 pixels and a width of 1 pixel). After correcting for Galactic foreground extinction, the ring has a mean $B-V$ and $V-I$ of 0.75 ± 0.06 and 1.29 ± 0.06, respectively.

To estimate the intrinsic colour of the background we used the 40×40 pixel region indicated by the box in Fig. 3.1. This region was selected because it is free of point

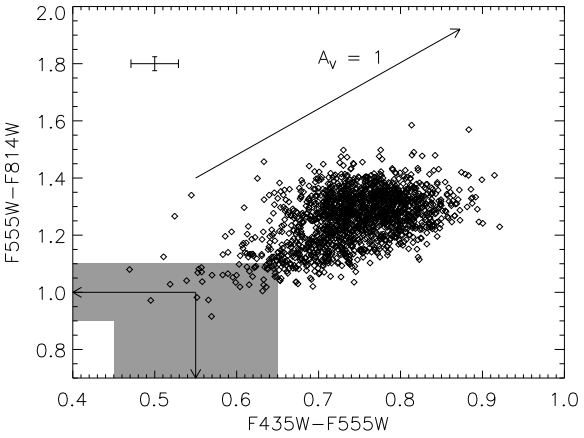

Figure 3.2: $F435W - F555W$ versus $F555W - F814W$ diagram of the pixels in the background box, after correcting for Galactic foreground extinction. The extinction vector is the standard extinction law from Cardelli et al. (1989). The cross in the top-left corner shows the typical error of the pixel colours. The gray region is selected by eye and shows the uncertainty around the two values selected as the intrinsic colour of the background (indicated by the two arrows): $(B-V)_0 = 0.55 \pm 0.10$, $(V-I)_0 = 1.00 \pm 0.10$.

sources and close to the object, and contains a large range of pixel colours, which we assume to be mainly due to extinction differences (the region is at the border of a dust lane). We show the $B-V$ versus $V-I$ colour-colour diagram of all pixels in this box in Fig. 3.2, which also shows the extinction vector. The observation that the scatter in this diagram is mostly parallel to the extinction vector is consistent with extinction being the dominant cause for colour variations among the pixels. Assuming that the pixels with the lowest values for $B-V$ and $V-I$ are least extincted, we estimate the upper limit for the intrinsic colour of the background to be $(B-V)_0 = 0.55 \pm 0.10$ and $(V-I)_0 = 1.00 \pm 0.10$.

We can estimate a lower limit for the extinction of the background ring around the object by assuming that the ring has the intrinsic colour of the background, and that the extinction is caused by a foreground sheet. Thus, the observed mean colours of the ring result in $E(B-V) = 0.2 \pm 0.1$ and $E(V-I) = 0.3 \pm 0.1$. It is more likely, however, that any dust present in the ring will be mixed with the stars. For the same sheet of dust, this reduces the amount of extinction estimated by the observed colours of the ring. We therefore conclude that if our object is in the disc, it has an extinction of *at least* $E(B-V) = 0.2$. If the object is behind the disc, the extinction is likely to be even higher.

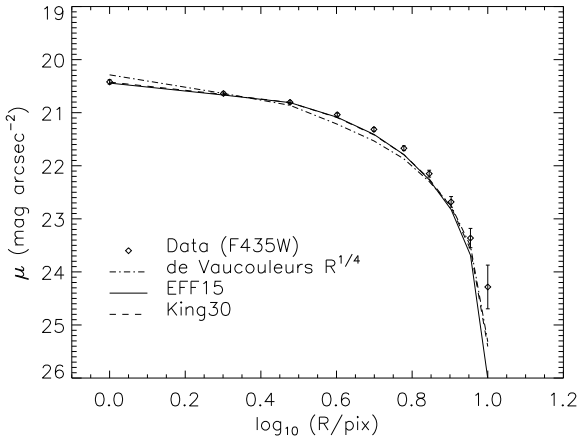

Figure 3.3: Surface brightness profile of the object (including errorbars), compared to the best-fitting surface brightness profiles, assuming typical star cluster profiles (EFF15 and King 30) and the typical profile for elliptical galaxies (a de Vaucouleurs $R^{1/4}$ law).

3.4 Surface brightness profile

In order to study the structural parameters of our object, we measured the surface brightness profile by performing aperture photometry in a series of circular rings around the object, measuring the average intensity in every ring as a function of radius. The resulting profile is shown in Fig. 3.3, in which we also plot the best-fitting surface brightness profiles as determined by the ISHAPE routine (Larsen 1999, 2004). ISHAPE fits two-dimensional analytic profiles to the surface brightness distribution of a source, taking into account the convolution with the PSF of the telescope. In Fig. 3.3 we show the best-fitting profiles typically used for fitting star clusters (i.e. a King 30 profile, see King 1962, and an EFF15 profile, see Elson et al. 1987) and the profile typically used for fitting elliptical galaxies (a de Vaucouleurs $R^{1/4}$ profile, see de Vaucouleurs 1948). The surface brightness profiles of these best-fitting models were measured from the model images that ISHAPE creates. Therefore they include the convolution with the PSF and take into account the slight ellipticity of the object.

Assuming different analytic profiles, we find consistent results for the FWHM and the aspect ratio (a) of the object, namely FWHM $\approx$ 9 pixels (along the major axis) and $a \approx 0.82$. Although the cluster profiles (King/EFF) provide better fits than a de Vaucouleurs profile, ISHAPE cannot determine the best-fitting concentration/power-law index for these profiles, since the extended "wings" are too significantly affected by the dust lanes. The value for the best-fitting effective radius depends on this index, and therefore on the choice of the profile. In Table 3.2 we summarise the results of fitting the surface brightness distribution of our object, assuming different profiles.

Table 3.2: Results of fitting different analytic profiles to the observed surface brightness distribution on the B_{F435W} image, using the ISHAPE routine.

Profile	FWHM (pix)	$R_{\rm eff}$ (pix)	$R_{\rm eff}$ (pc)[a]
de Vaucouleurs	0.15	1.1×10^3	–
EFF15	9.21	9.47	19.29[b]
EFF25	9.34	5.78	11.77
King 5	8.80	5.66	11.52
King 30	9.07	12.15	24.74

[a] Assuming a distance to M51 of 8.4 ± 0.6 Mpc (Feldmeier et al. 1997).

[b] This value is slightly smaller than the $R_{\rm eff}$ = 21.6 pc measured by Scheepmaker et al. (2007), which is caused by the use of a larger "fitting radius" in the current study (i.e. 10 pixels).

For the sake of completeness we also included the values for the de Vaucouleurs profile. Due to the much steeper decline in the innermost regions of a de Vaucouleurs profile, the FWHM of this profile is much smaller than the FWHM of the other profiles, and the effective radius is much larger. These values are not very meaningful, however, since the de Vaucouleurs profile does not provide a good fit to the data.

For comparison, the effective radius of a typical star cluster is 2–3 pc (Harris 1996, Jordán et al. 2005, Scheepmaker et al. 2007), which, at the distance of M51, is equivalent to a FWHM $\approx$ 1 pixel. Thus, although the effective radius of the object is not well constrained without knowing the underlying profile, it is clear that if the object is at the distance of M51, it is about 9–10 times larger than a typical star cluster.

3.5 The nature of the object

3.5.1 Background galaxy

If the object is a background galaxy, the mean extinction of the ring around the object (Sect. 3.3.2) is a lower limit for the mean extinction of the background galaxy. If we use an extinction of at least $E(B-V) = 0.2$, as estimated in Sect. 3.3.2, to correct the observed colours, we find intrinsic colours of the background galaxy no redder than $(B-V)_0 = 0.43$, $(V-I)_0 = 0.68$ and $(J-H)_0 = 0.81$. In Table 3.3 we list the corrected colours for a range of extinctions.

We can compare the intrinsic colours of the background galaxy to the typical colours of other galaxies. Tinsley (1971) finds $(B-V)_0 \approx 0.9$ for giant elliptical galaxies (after applying K-corrections), and using the catalogue of Eisenhardt et al. (2007), we find a mean $(B-V)_0 = 1.15$ and $(V-I)_0 = 1.31$ for 486 galaxies in the Coma cluster (without K-corrections). Tonry et al. (2001) find a mean colour of $(V-I)_0 = 1.15 \pm 0.06$

Table 3.3: Intrinsic broad-band colours of the object, assuming different degrees of extinction and using the Galactic extinction law of Cardelli et al. (1989).

E(B-V)	$(B-V)_0$	$(V-I)_0$	$(J-H)_0$
0	0.63	1.00	0.82
0.1	0.53	0.84	0.79
0.2[a]	**0.43**	**0.68**	**0.76**
0.4	0.23	0.35	0.71
0.6	0.03	0.03	0.65
0.8	-0.17	-0.29	0.59
1.0	-0.37	-0.62	0.54

[a] This value is our best estimate for the average extinction in a ring around the object (Sect. 3.3.2).

for a survey of 300 (mostly E and S0) galaxies (without K-corrections). These colours are significantly redder than those estimated for our object. The colours used in these galaxy surveys are in the standard Johnson-Cousins system, and a direct comparison to the colours of the background galaxy could therefore be misleading. However, Fukugita et al. (1995) give colours (not corrected for Galactic reddening) of galaxies with different morphological types in the *HST/WFPC2* filter system. For E- and S0-type galaxies, these colours are $(V_{\rm F555W} - I_{\rm F814W}) = 1.27$ and 1.12, respectively. These colours are still significantly redder than those estimated for our object, and this suggests that the colour differences involved in the transformations between the photometric systems are small.

Applying K-corrections to the objects in the catalogue of Eisenhardt et al. (2007) or Tonry et al. (2001) would make their colours bluer, but also the colours of our object would have to be corrected for its K-correction, depending on its unknown distance. To reconcile the difference in colours between our object and these catalogue galaxies, the K-corrections of these galaxies have to be ∼0.6 mag *more* negative (in $B-V$ and $V-I$) than those of our object. Considering the distance to the Coma cluster of $\sim 85 \pm 10$ Mpc (Jensen et al. 1999), the expected K-corrections are $\lesssim -0.1$ mag (Bicker et al. 2004). Therefore we conclude that K-corrections *cannot* reduce the difference in colours between our object and the typical galaxies.

In Fig. 3.4 we compare the intrinsic colours of the object to the typical galaxy colours. If our object is a background galaxy, its $(B-V)_0$ and $(V-I)_0$ colours are significantly bluer than the mean $(B-V)_0$ and $(V-I)_0$ colours of elliptical galaxies, and also bluer than 98% and 97%, respectively, of the galaxies of the Coma cluster.

Another comparison to elliptical galaxies can be made in terms of the surface brightness profile. The surface brightness profile of many bright elliptical galaxies is best described by a de Vaucouleurs $R^{1/4}$ law (de Vaucouleurs 1948). In Fig. 3.3 we compare the surface brightness profile of our object with a fit assuming a de

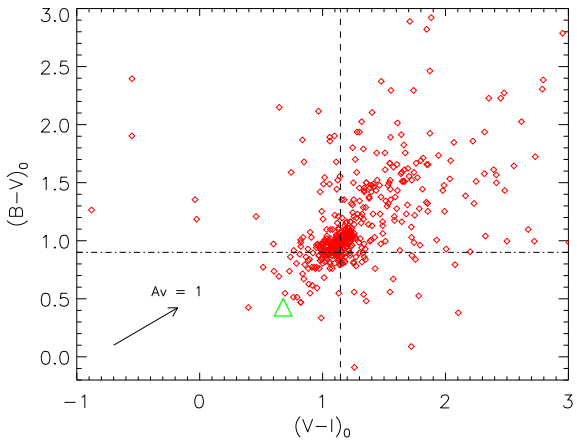

Figure 3.4: $(B-V)_0$ versus $(V-I)_0$ diagram, showing the 486 galaxies from the Coma cluster (small diamonds), the mean $(B-V)_0$ of giant elliptical galaxies of Tinsley (1971) (horizontal line) and the mean $(V-I)_0$ of mostly E and S0 galaxies of Tonry et al. (2001) (vertical line). For comparison, we also show the estimated intrinsic colours of our object, assuming an extinction of $E(B-V) = 0.2$ (big triangle).

Vaucouleurs law. The figure shows that a de Vaucouleurs law is steeper than the observed surface brightness profile (both an EFF15 and a King 30 profile for clusters provide a better fit to the data).

If our object is a background galaxy, it does not necessarily have to be an elliptical or S0 galaxy, and could be a disc galaxy. For disc galaxies, Freeman (1970) found a nearly constant central surface brightness of $\mu_B = 21.65 \pm 0.30$ mag arcsec^{-2} for 28 out of 36 galaxies. 7 out of 36 galaxies had a surface brightness brighter than ~ 20.1 mag arcsec^{-2}. Barden et al. (2005) find $\mu_B = 21.11 \pm 0.03$ mag arcsec^{-2}, increasing with redshift to $\mu_B \approx 19.7 \pm 0.07$ mag arcsec^{-2} for $z = 1$. Comparing these values to our object, within a radius of 2 pixels our object has $\mu_B \leq 19.60$ mag arcsec^{-2}, corrected for Galactic foreground extinction, and an extinction of at least $E(B-V) \geq 0.2$ for the disc of M51. Our object therefore has a surface brightness which is brighter than the majority of the disc galaxies studied by Freeman (1970), but it is consistent with the brightest galaxies from this sample and with the highest redshift galaxies from Barden et al. (2005).

Assuming the lower-limit estimate of $E(B-V) = 0.2$, we can therefore not exclude that the object is a background galaxy. We find, however, that for an elliptical galaxy, the object has $(B-V)_0$ and $(V-I)_0$ colours ~ 0.6 mag bluer than expected and a surface brightness profile that falls off less steeply than a $R^{1/4}$ law, while for a disc galaxy the surface brightness is remarkably high.

Table 3.4: Results of fitting different GALEV SSP models to the broad-band photometry of the object.

#	Constraint	$Z/Z_\odot$	Age/Gyr	$M/10^5 M_\odot$	$E(B-V)$
1.	none	0.4	$1.2^{+14.8}_{-1.2}$	$1.6^{+7.5}_{-1.5}$	$0.1^{+0.6}_{-0.1}$
2.	$0.4 \leq Z/Z_\odot \leq 2.5$	0.4	$1.2^{+0.9}_{-1.2}$	$1.6^{+1.2}_{-1.5}$	$0.1^{+0.5}_{-0.1}$
3.	$Z = Z_\odot$		$1.0^{+0.4}_{-1.0}$	$1.9^{+0.6}_{-1.8}$	$0.1^{+0.4}_{-0.1}$
4.[a]	$Z/Z_\odot = 0.4$, $E(B-V) = 0$		$1.4^{+0.5}_{-0.2}$	$1.7^{+0.8}_{-0.3}$	
5.[b]	$Z = Z_\odot$, $E(B-V) = 0.2$		$0.7^{+0.1}_{-0.1}$	$2.2^{+0.3}_{-0.3}$	
6.[c]	$Z = Z_\odot$, $E(B-V) = 0.7$		0.004[d]	0.084[d]	

[a] Case B.
[b] Case A.
[c] Maximum extinction.
[d] The errors in this best-fitting model cannot be estimated due to the much lower probability of the remaining models.

3.5.2 Star cluster

Assuming the object is a star cluster, it could either be located in the disc of M51, or in front of the disc and seen in projection. For the latter case, the metallicity of the cluster could be different from the metallicity of the disc, and the extinction could be lower than the mean extinction of the ring around the object (Sect. 3.3.2). We used the GALEV SSP models described in Sect. 3.3.1 to fit the age, mass, extinction and metallicity of the cluster. We should note here, however, that not using U-band data in the SSP model fitting makes the derived ages and extinctions rather uncertain. Anders et al. (2004) have shown that not including U-band data can lead to underestimating the extinction and overestimating the ages of young clusters by up to an order of magnitude. There are *HST/WFPC2* U-band data of the region covering our object available in the archives. However, these data are not deep enough to detect our object. We cannot exclude the possibility that our object is younger than the best-fitting age determined from only using BVIJH. We will take this uncertainty into account when we draw our conclusions in Sect. 3.6.

The results of the fits, for different initial constraints, are summarised in Table 3.4. Without any initial constraints on the metallicity and extinction, the age and mass of the cluster are not well defined, although the best fit indicates $Z/Z_\odot = 0.4$ and an extinction in the range 0–0.7 in terms of $E(B-V)$. The lowest two metallicities ($0.02Z_\odot$ and $0.2Z_\odot$) were fitted with a lower probability than a metallicity in the range $0.4 \leq Z/Z_\odot \leq 2.5$. We therefore exclude these lowest two metallicities, which reduces the maximum possible age and mass of the cluster to age $\leq$ 2.1 Gyr and $M \leq 2.8 \times 10^5 M_\odot$. A metallicity in the range $0.4 \leq Z/Z_\odot \leq 2.5$ is consistent with the observed metallicity in the inner disc of M51 (Sect. 3.1).

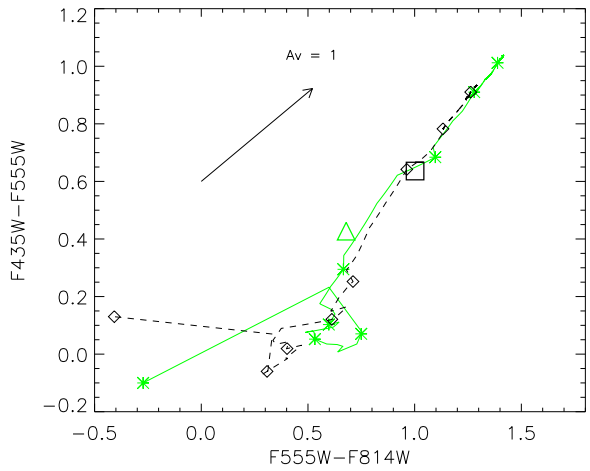

Figure 3.5: $B-V$ versus $V-I$ diagram, showing the colour evolution with time of two GALEV SSP models (solid: $Z = 0.02$, dashed: $Z = 0.008$), and the object without extinction correction (square) and with an extinction correction of $E(B-V) = 0.2$ (triangle). The symbols on the model curves indicate values of log(age), running from 6.6 (lower left) to 10.1 (top right) in steps of 0.5 dex.

If we fix the models to solar metallicity, we find an extinction of $E(B-V) = 0.1^{+0.4}_{-0.1}$, which is consistent with our independent estimate of the extinction in the disc from Sect. 3.3 (using the average background colour). We therefore consider two cases:

A. The cluster is located in the disc with an extinction of $E(B-V) \simeq 0.2$ and solar metallicity.

B. The cluster is seen in projection against the disc with an extinction of $E(B-V) = 0.0$ and a metallicity of $Z/Z_\odot = 0.4$.

In Fig. 3.5 we compare the two cases with the $B-V$ versus $V-I$ colour-colour evolution of GALEV SSP models for $Z/Z_\odot = 0.4$ (black dashed curve) and $Z/Z_\odot = 1$ (grey solid curve).

Considering case A, we find a best-fitting age $= 0.7^{+0.1}_{-0.1}$ Gyr and $M = 2.2^{+0.3}_{-0.3} \times 10^5 M_\odot$. For case B we find an age of $1.4^{+0.5}_{-0.2}$ Gyr and a mass of $M = 1.7^{+0.8}_{-0.3} \times 10^5 M_\odot$.

If the cluster is located in the disc of M51 at a distance of only 1 kpc from the centre (case A), one must question how it can have survived for such a long time. To this end we estimate its initial mass and the expected disruption time. For clusters losing mass due to stellar evolution and tidal dissolution, the present mass is related to the initial mass as

$$M(t) = M_i \left\{ \mu_{\rm ev}(t)^\gamma - \frac{\gamma t}{t_0} M_i^{-\gamma} \right\}^{1/\gamma} \tag{3.1}$$

with M in $M_\odot$ (Lamers et al. 2005), where $\mu_{\rm ev}$ is the fraction of the initial mass that would have remained at age t, if stellar evolution had been the only mass loss mechanism. For $t = 0.7$ Gyr and solar metallicity, one finds $\mu_{\rm ev} = 0.77$. The parameters t_0 and γ describe the mass loss due to dissolution of the cluster as $({\rm d}M/{\rm d}t)_{\rm dis} = -M(t)^{1-\gamma}/t_0$ (Lamers et al. 2005). N-body simulations of clusters in tidal fields (Baumgardt & Makino 2003) and N-body simulations of cluster dissolution due to shocks by encounters with giant molecular clouds or spiral arms (Gieles et al. 2006c, 2007) both suggest that $\gamma \simeq 0.62$. This value agrees with the value that was derived empirically from cluster samples in different galaxies (Boutloukos & Lamers 2003, Gieles et al. 2005). The value of the disruption parameter t_0 depends strongly on the local conditions. For clusters in M51 at $1 < R < 5$ kpc, Gieles et al. (2005) find a mean value of $t_0 = 6.6 \times 10^5$ yr. Adopting these values, Eq. 3.1 implies an initial mass of $M_i \simeq 4.5 \times 10^5\, M_\odot$, and we find that the cluster has lost about 50% of its initial mass.

In this estimate we have neglected the dependence of the dissolution time on galactocentric distance and the large radius of the cluster. The dissolution time of clusters is expected to decrease with galactocentric distance as $t_0 \propto R_G/V$, where V is the circular velocity at distance R_G from the centre (Baumgardt & Makino 2003, Gieles et al. 2005). This implies that t_0 could be smaller than the value adopted above by as much as a factor two or three. In that case, Eq. 3.1 implies an initial mass of about 6–9×10^5 $M_\odot$, and the cluster has lost about 70% of its mass.

We note that the cluster, having an $R_{\rm eff}$ of ∼12–25 pc (depending on the assumed brightness profile, see Table 3.2), is very extended and "fuzzy". The tidal radius of a $M = 2.2 \times 10^5\, M_\odot$ cluster at a galactocentric distance of 1.02 kpc is

$$r_t = \left(\frac{GM}{2V_{\rm G}^2}\right)^{1/3} R_{\rm G}^{2/3} \approx 23.9 \text{ pc}, \tag{3.2}$$

where we used $V_{\rm G} = 200 {\rm km\,s^{-1}}$ (García-Burillo et al. 1993). Therefore, if the object is a cluster in the disc of M51, its effective radius of ∼12–25 pc is very close to the tidal radius (within a factor ∼0.5-1). This is remarkable, since such an extended cluster would not be able to stay bound at this location in the disc.

The disruption time of a cluster depends implicitly on the radius through the parameter t_0. For disruption in a tidal field, $t_0 \propto t_{\rm rh} \propto M^{1/2} r_{\rm h}^{3/2}$ (Spitzer 1987), in which $t_{\rm rh}$ is the half-mass relaxation time and $r_{\rm h}$ is the half-mass radius. This suggests that more extended clusters have a longer disruption time compared to compact clusters. However, for the disruption timescale ($t_{\rm dis}$) of clusters due to external perturbations (e.g. shocks due to encounters with GMCs) Spitzer (1958) has derived that $t_{\rm dis} \propto M r_{\rm h}^{-3}$, implying that a large cluster is more susceptible to external disruptive effects (see also Gieles et al. 2006c). Considering the location of the cluster close to the centre of M51 in a region with many dust lanes, the external perturbations are likely to dominate in the disruption, and they will shorten the disruption time for such an extended cluster, compared to the disruption time of a cluster with a typical size of about 3 pc. Therefore, the estimated value of the disruption time parameter $t_0 \sim$ 2–3×10^5 yr would be too large. Using Eq. 3.1, this implies that the initial mass

of such an extended cluster is probably much higher, to explain its current mass and age. This could mean that the cluster has lost significantly more than 70% of its initial mass, and is currently uncomfortably close to final dissolution. Although such a scenario is not impossible, it is unlikely that we observe a cluster in this final phase of its lifetime.

Case B, seeing the cluster in projection against the disc, is considered to be more likely. In this scenario the cluster can be located well outside the disc, where the tidal radius will be larger and the expected disruption time will be longer. This means that the initial mass needs to be lower compared to case A, and that we observe the cluster in a more "calm" phase of its lifetime.

To establish the nature of the object with greater certainty than presented in this study requires spectroscopic observations. These will be challenging, however, considering the low brightness of the object (Table 3.1). Deep U-band imaging, obtained in good seeing conditions, would also help establish the age and extinction with greater certainty.

3.6 Conclusions

We have studied the photometry, extinction and structural parameters of a peculiar object in M51 using *HST*/*ACS* and *HST*/*NICMOS* data. We have considered different possible scenarios for the object, from which we conclude the following:

1. If we assume that the object is a background galaxy, we estimate that the extinction through the disc of M51 is at least $E(B-V) = 0.2$. Correcting for this *minimum* extinction, we find intrinsic colours of $(B-V)_0 = 0.43$, $(V-I)_0 = 0.68$ and $(J-H)_0 = 0.76$. These colours suggest that the object is not a background galaxy, because $(B-V)_0$ and $(V-I)_0$ are ∼0.6 mag bluer than expected for a typical elliptical galaxy (Fig. 3.4) and the surface brightness is ∼ 2 mag arcsec^{-2} brighter than a typical disc galaxy. If the extinction would be larger than $E(B-V) = 0.2$, these differences in colour and surface brightness would be even larger.

2. The surface brightness distribution can be well approximated by typical cluster profiles (i.e. EFF or King profiles) with a FWHM of ∼9 pixels. A de Vaucouleurs $R^{1/4}$ law, typical for elliptical galaxies, does not provide a good fit to the inner part of the observed profile (Fig. 3.3). Because the exact concentration (or power-law) index of the object cannot be determined, the effective radius of the object depends on the choice of the profile. Assuming the object is at the distance of M51, our best estimates for the effective radius are between ∼12 pc and ∼25 pc (Table 3.2).

3. If we assume that the object is a star cluster in the disc of M51, we estimate an age of $0.7^{+0.1}_{-0.1}$ Gyr and a mass $M = 2.2^{+0.3}_{-0.3} \times 10^5\ M_\odot$, assuming $E(B-V) = 0.2$ and solar metallicity. Considering the large size of the object, however, we

estimate that in this scenario the cluster must initially have been very massive ($> 4.5 \times 10^5 M_\odot$), and that we observe the cluster just prior to final dissolution. Although not impossible, this scenario is considered to be unlikely.

4. We cannot fully exclude the possibility that our best-fitting cluster ages and extinctions are over- and underestimated, respectively, due to the lack of U-band photometry of our object. If we consider the *maximum* extinction of $E(B-V) = 0.7$ (model 6 in Table 3.4), instead of the *best* extinction, the cluster has an age of only ~4 Myr and is not close to final dissolution. With our current data, however, the likelihood of this fit is very low.

5. If we assume that the object is a star cluster well outside the disc of M51 and seen in projection against it, we estimate an age of $1.4^{+0.5}_{-0.2}$ Gyr and a mass of $M = 1.7^{+0.8}_{-0.3} \times 10^5\ M_\odot$. This scenario naturally explains why the best-fitting extinction is low, $E(B-V) = 0.1^{+0.5}_{-0.1}$, although we observe the cluster in between two dust lanes. Furthermore, this scenario implies that we are not observing the cluster in a special phase of its lifetime.

6. We conclude that, without additional U-band data or spectroscopy, both the "disc" and "projection" scenarios are possible within the uncertainties. With the current data, however, the cluster models favour the scenario in which the object is a star cluster seen in projection against the disc. In this scenario, the cluster just qualifies as being a "faint fuzzy" star cluster, namely having $(B-V)_0 > 0.6$, $(V-I)_0 > 1.0$ and $R_{\rm eff} > 7$ pc (Larsen & Richtler 2000). Seen in projection against the spiral disc, the (projected) galactocentric distance of 1 kpc is not unexpected. However, with an estimated age of $1.4^{+0.5}_{-0.2}$ Gyr, the formation mechanism of such a cluster, in combination with its extended shape and its current location outside the spiral disc, are interesting issues that leave room for further investigation.

Acknowledgements We thank the *International Space Science Institute* (ISSI) in Bern, Switzerland, where part of this research took place. The anonymous referee is thanked for useful comments and suggestions.

Chapter 4

The spatial distribution of star and cluster formation in M51

R. A. Scheepmaker, H. J. G. L. M. Lamers, P. Anders, and S. S. Larsen

Astronomy & Astrophysics v.494, p.81-93 (2009)

Abstract *Aims.* We study the connection between spatially resolved star formation and young star clusters across the disc of M51. *Methods.* We combine star cluster data based on *B*, *V*, and *I*-band *Hubble Space Telescope ACS* imaging, together with new *WFPC2 U*-band photometry to derive ages, masses, and extinctions of 1580 resolved star clusters using SSP models. This data is combined with data on the spatially resolved star formation rates and gass surface densities, as well as Hα and 20 cm radio-continuum (RC) emission, which allows us to study the spatial correlations between star formation and star clusters. Two-point autocorrelation functions are used to study the clustering of star clusters as a function of spatial scale and age. *Results.* We find that the clustering of star clusters among themselves decreases both with spatial scale and age, consistent with hierarchical star formation. The slopes of the autocorrelation functions are consistent with projected fractal dimensions in the range of 1.2–1.6, which is similar to other galaxies, therefore suggesting that the fractal dimension of hierarchical star formation is universal. Both star and cluster formation peak at a galactocentric radius of ∼2.5 and ∼5 kpc, which we tentatively attribute to the presence of the 4:1 resonance and the co-rotation radius. The positions of the youngest (< 10 Myr) star clusters show the strongest correlation with the spiral arms, Hα, and the RC emission, and these correlations decrease with age. The azimuthal distribution of clusters in terms of kinematic age away from the spiral arms indicates that the majority of the clusters formed ∼ 5–20 Myr before their parental gas cloud reached the centre of the spiral arm.

4.1 Introduction

The increase in the amount of multi-wavelength data during the past few decades has been of tremendous importance for the field of star formation. On the largest scales, these multi-wavelength studies focussed primarily on the tight correlation between global RC and far-infrared (FIR) emission of galaxies (e.g. Condon 1992, Niklas & Beck 1997, Niklas 1997, Yun et al. 2001) and on the global Schmidt-law, which dictates that there is a power-law relation between the area-normalised star formation rate (SFR) and total gas surface density with an index of 1.4 ± 0.15 (Kennicutt 1998b). These correlations have proven useful in the derivation of global star formation rates from radio-continuum observations (e.g. Condon 1992), as well as in models of galaxy evolution (Mihos & Hernquist 1994).

More recently, these multi-wavelength correlations are exploited to study star formation *locally* across single galaxies. This is done by either utilizing the RC-FIR correlation (Murphy et al. 2006, Schuster et al. 2007, Murphy et al. 2008), or by combining *Spitzer Space Telescope* FIR observations with Hα and Paα data, which allows for a more thorough extinction correction on the derived star formation rates (Calzetti et al. 2005, Kennicutt et al. 2007). Combined with new CO and H I data, recent studies show that the Schmidt-law is also valid *locally* across the spiral galaxy M51 (Schuster et al. 2007, Kennicutt et al. 2007).

There is ample evidence that star formation leads to formation of star clusters (Lada & Lada 2003, and references therein). Therefore, star formation across spiral galaxies has been studied extensively through their star cluster populations, either by using ground-based data (Larsen & Richtler 1999, 2000), or by exploiting the higher resolution *Hubble Space Telescope* (*HST*) observations (e.g. Holtzman et al. 1992, Meurer et al. 1995, Whitmore et al. 1999, de Grijs et al. 2003, Larsen 2004). Most of these studies, however, focus on the star cluster properties themselves, on the connection between the galaxy's star cluster population and SFR on *global* scales, or on their spatial correlation (Zhang et al. 2001). There is still a lack of evidence, however, on the actual *fraction* of current star formation taking place in young star clusters (although de Grijs et al. 2003 find a lower limit of $\approx$ 35% for the Mice galaxies and Fall et al. 2005 find a lower limit of 20% in the Antennae). Although it is probably true that most star formation takes place in some sort of embedded, clustered form (Lada & Lada 2003), it is not clear yet which fraction of these clusters are actually observable as star clusters after they emerge from their natal gas cloud (Bastian & Goodwin 2006, Goodwin & Bastian 2006) and if, or how, this depends on environment. The answers to such questions could give us important clues on the process of star formation and the early evolution of young star clusters.

Before such a quantitative comparison can be made, however, we first need to determine the amount of *spatial* correlation between star and cluster formation, since any quantitative comparison is only meaningful for regions that are spatially correlated. Besides, determining the spatial correlation between clusters themselves allows us to study the amount and evolution of clustering of star clusters, which provide important clues as to which extent the formation of clusters is hierarchical

(e.g. Efremov & Elmegreen 1998, Bastian et al. 2007).

For M51 data with a wide wavelength range and good spatial resolution are available. This makes it possible to study first, how well the positions of star clusters are trace the regions of star formation across this spiral galaxy and second, which fraction of the star formation is taking place in the form of visually observable star clusters. In this study we combine data on the *resolved* Schmidt-law in M51 (SFR and gas surface densities, Kennicutt et al. 2007) as well as archival radio-continuum, 2MASS and *HST/WFPC2* data with slightly resolved young star clusters from Scheepmaker et al. (2007, Chapter 2 in this thesis). These datasets cover a large fraction of the disc, allowing us to compare star and cluster formation under a range of conditions, such a low/high gas and stellar surface densities, within a single galaxy consistently.

In this chapter we will introduce the new datasets used, and present new *WFPC2* U_{F336W} photometry. This photometry allows us to add ages, masses and extinctions to the star cluster data of Scheepmaker et al. (2007). In the remainder of this chapter we will then focus on the *spatial* correlations between star and cluster formation, for differently aged cluster populations. A *quantitative* comparison between star and cluster formation, as well as the cluster initial mass function (CIMF), will be the subject of Chapter 5.

In Sect. 4.2 we describe the star cluster data we used, as well as the *HST/WFPC2* observations. In Sect. 4.3 we estimate ages, masses and extinctions of the star clusters in order to select our cluster samples. We describe the data on SFRs and gas densities in Sect. 4.4, together with our method of tracing the spiral arms. Finally, in Sect. 4.5 we study the spatial distribution of star clusters and star formation in M51 and we summarise our main results in Sect. 4.6.

4.2 Observations and photometry

For our star cluster data, we make use of the dataset of Scheepmaker et al. (2007, Chapter 2 in this thesis), complemented with *HST/WFPC2* U-band (U_{F336W}) observations.

4.2.1 HST/ACS observations

In Chapter 2 we used the *HST/ACS* mosaic image of M51 in B_{F435W} ($\sim B$), V_{F555W} ($\sim V$) and I_{F814W} ($\sim I$) to select star clusters across the entire disc of M51, based on size measurements. For a complete description we refer to Chapter 2 for the star cluster data and to Mutchler et al. (2005) and the M51 mosaic website[1] for the image processing. Below, the source selection, photometry and size measurements of the clusters are summarised.

The SExtractor package (Bertin & Arnouts 1996) was used to select sources above a local threshold, cross-correlating between the three filters. Aperture photometry

[1] http://archive.stsci.edu/prepds/m51/

in the VEGAmag system was performed on the sources using the IRAF[2]/DAOPHOT package, using an aperture radius of 5 pixels and a background annulus with an inner radius of 10 pixels and a width of 3 pixels. A fixed aperture correction for a 3 pc source was applied, which was respectively -0.17 mag for B_{F435W} and V_{F555W} and -0.19 mag for I_{F814W}, and the photometry was corrected for Galactic foreground extinction in the direction of M51 according to Appendix B of Schlegel et al. (1998). The star clusters, being slightly extended, were distinguished from stars based on size measurements using the ISHAPE routine (Larsen 1999, 2004), assuming EFF 15 models (Elson et al. 1987) for the surface brightnesss profiles of the clusters.

4.2.2 HST/WFPC2 observations

For a reliable estimation of star cluster parameters using *Simple Stellar Population* models (see Sect. 4.3.1), Anders et al. (2004) have shown that at least four passbands are necessary, with the U and B bands having the highest significance for young clusters. We therefore complemented the *HST/ACS* data with archival *HST/WFPC2* observations in the U_{F336W} passband ($\sim U$).

A total of seven pointings were taken from the ESO/ST-ECF science archive. The footprints of the pointings, overlaid on the *ACS* B_{F435W} image, are shown in Fig. 4.1. An overview of the different datasets is given in Table 4.1. We note that proposal ID 10501 includes another U_{F336W} pointing covering the companion galaxy of M51, NGC 5195. Since we are interested in the star clusters in the disc of M51, this pointing (dataset U9GA0101B) was not used. We did not use the WF4 chip of dataset U9GA0601B (field 7 in Fig 4.1) either, since it contained too few sources, making the manual selection of enough reference objects impossible, which were necessary to transform the cluster coordinates from the *ACS* frame to the *WFPC2* frames (see below).

We used the individual chips (WF and PC) of the standard pipeline-reduced associations, i.e. no further data reduction was performed. On every chip between 6–11 sources were matched with sources on the ACS B_{F435W} image. Using these sources the coordinate transformations between the *WFPC2* chips and the *ACS* frame were calculated using the IRAF task GEOMAP. The task GEOXYTRAN was used to transform the coordinates of the 7698 resolved sources of Chapter 2 on the *ACS* B_{F435W} image to the *WFPC2* chips. In most cases the root-mean-square accuracy in X and Y was better than one pixel, and in all cases better than 2 pixels.

Aperture photometry was performed at the transformed coordinates using DAOPHOT, allowing for a maximum centring shift of three pixels. For the PC chips a $(5, 10, 3)$ configuration was used for the radius of respectively the aperture, annulus and width of the annulus in pixels. For the WF chips the configuration was $(3, 7, 3)$. Aperture corrections to an aperture of 0.5''were measured using analytic cluster profiles with an effective radius of 3 pc, which were subsequently convolved with the

[2]The Image Redcution and Analysis Facility (IRAF) is distributed by the National Optical Astronomy Observatories, which are operated by the Association of Universities for Research in Astronomy, Inc., under cooperative agreement with the National Science Foundation.

Table 4.1: Overview of the different *HST/WFPC2* U_{F336W} band datasets used in this study.

Field[a]	ID	PI	Dataset (association)	Exposure time	Observation date
1	5652	R. P. Kirshner	U2EW0205B	$3 \times 400 = 1200$ s	12 May 1994
2	7375	N. Scoville	U50Q0105B	$2 \times 600 = 1200$ s	21 Jul 1999
3	10501	R. Chandar	U9GA0201B	$2 \times 1300 = 2600$ s	24 Jan 2006
4			U9GA5301B	$2 \times 1200 = 2400$ s	28 May 2006
5			U9GA0401B	$2 \times 1300 = 2600$ s	13 Nov 2005
6			U9GA0501B	$2 \times 1300 = 2600$ s	13 Nov 2005
7			U9GA0601B	$2 \times 1300 = 2600$ s	13 Nov 2005

[a] The numbers refer to the footprints in Fig. 4.1.

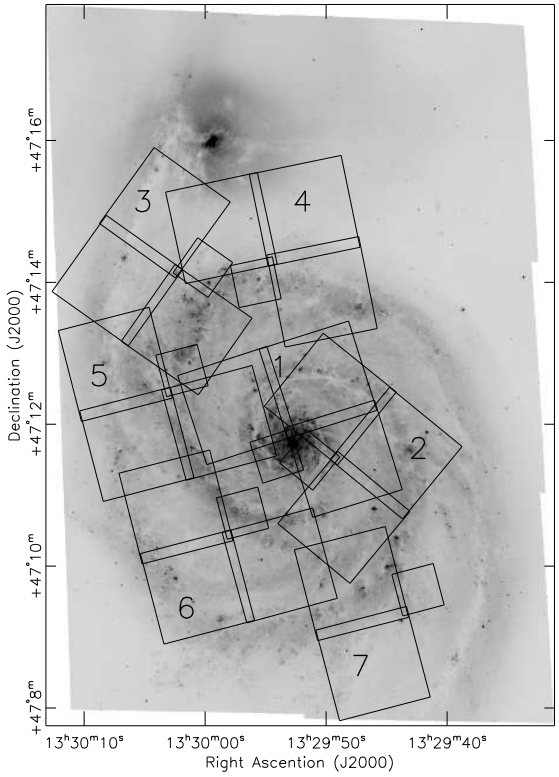

Figure 4.1: Footprints of the *WFPC2* U_{F336W} fields used in this study, overlaid on the *ACS* B_{F435W} mosaic image. The numbers refer to the different datasets in Table 4.1.

PSF. These corrections for the WF and PC chips were −0.14 and −0.19 mag for the WF and PC chips, respectively. Zeropoints (calibrated for the 0.5″aperture) and CTE loss corrections were calculated following Dolphin (2000).[3] We corrected for Galactic foreground extinction in the direction of M51 according to Appendix B of Schlegel et al. (1998).

From the initial source list of 7698 resolved sources on the *ACS* B_{F435W} image, we retrieved positive photometry on the *WFPC2* U_{F336W} images of 5502 sources. The remaining sources had either an aperture covering the edge of an image, a failure in DAOPHOT's centring algorithm or a negative flux, caused by a combination of a faint

[3]The most recent equations for the CTE losses were taken from `http://purcell.as.arizona.edu/wfpc2_calib/`.

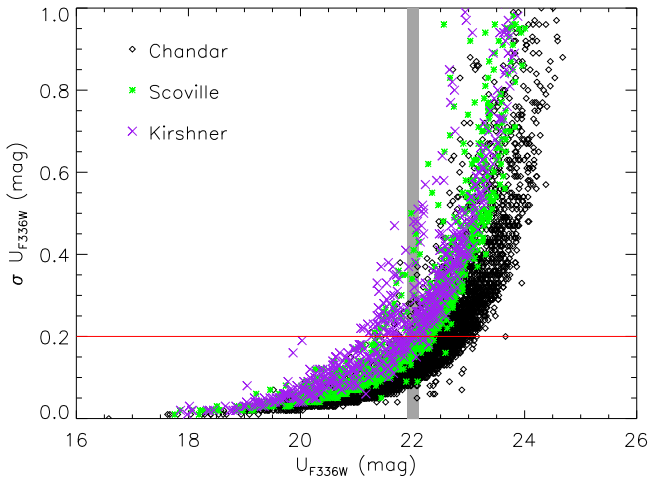

Figure 4.2: The error in the U_{F336W} magnitude versus the U_{F336W} magnitude for all 5502 sources for which we have photometry. The different symbols/colours refer to the different datasets listed in Table 4.1. The horizontal line indicates $\sigma(U_{F336W}) = 0.2$ mag and the bin at $U_{F336W} = 22$ mag indicates the magnitude range in which ~90% of the clusters has $\sigma(U_{F336W}) < 0.2$ mag.

source and noise in the background annulus. As can be seen in Fig. 4.1, there is some overlap between different *WFPC2* chips. If a source had photometry in more than one U_{F336W} chip, the photometry with the smallest error was selected.

In Fig. 4.2 we show the resulting photometry and error in the photometry for the U_{F336W} passband. As expected, the photometry of fields 1 and 2 has larger errors compared to the photometry of fields 3–7, due to the deeper exposures of the latter fields. The horizontal line at $\sigma(U_{F336W}) = 0.2$ mag indicates the limit we applied to select only clusters with accurate photometry. The bin centred on $U_{F336W} = 22$ mag indicates the magnitude at which approximately 10% of the clusters will be rejected from the sample by this $\sigma(U_{F336W}) < 0.2$ mag criterion. These limits will be used in Sect. 4.3.3 to select cluster samples.

4.3 Selection of the cluster samples

In this study we are primarily interested in the spatial distribution of *young* star clusters in the disc of M51. We therefore used *Simple Stellar Population* (SSP) models to estimate the age, mass and extinction of all 5502 clusters for which we have *UBVI* photometry (Sect. 4.3.1). The estimated ages were then used to select cluster samples with different ages (Sect. 4.3.3).

4.3.1 SSP model fitting

For our age determinations we used the GALEV SSP models (Schulz et al. 2002, Anders & Fritze-v. Alvensleven 2003) together with the ANALYSED tool (Anders et al. 2004). In summary, ANALYSED compares the broad-band spectral energy distribution (SED, in our case UBVI) of every cluster to a large grid of modelled SEDs for different ages, extinctions and metallicities. The model with the lowest χ^2 is selected, and the (initial) mass of the cluster is derived by scaling the entire modelled SED to the observed SED. The models and the tool have been extensively tested (e.g. Anders et al. 2004, de Grijs et al. 2005, de Grijs & Anders 2006) and the uncertainty in the derived ages is typically < 0.4 dex.

The GALEV models were preferred above other SSP models because of their freedom in stellar evolutionary models and metallicity and because their output and treatment of extinction is tailored to our specific *HST*/*ACS* filters. Therefore, no transformation between different photometric systems was necessary. We used the models based on the Geneva isochrones (Charbonnel et al. 1993, Schaerer et al. 1993), which are better suited for the age range we are interested in (i.e. age $\lesssim$ 100 Myr) than e.g. Padova isochrones (Bertelli et al. 1994, Girardi et al. 2000), due to a higher time resolution in this age range. However, in Sect. 4.3.2 we will discuss the impact of the different isochrones on the derived cluster ages. For the models we further adopted a Kroupa (2001) stellar initial mass function (IMF) down to $0.1 M_\odot$ and a metallicity between $0.4 Z_\odot$ and $2.5 Z_\odot$. This range in metallicity covers the observed metallicity of H II regions in the disc of M51 (solar to twice solar, Diaz et al. 1991, Hill et al. 1997) and the slightly lower metallicity expected for older clusters. The extinction was varied between $0 \leq E(B-V) \leq 1$ in steps of 0.05 and the Cardelli et al. (1989) extinction law was applied. Absolute magnitudes of all clusters were calculated assuming $m - M = 29.62$ (i.e. a distance to M51 of 8.4 ± 0.6 Mpc, Feldmeier et al. 1997). In Fig. 4.3 we compare the photometry of our clusters to the SSP models in two colour-colour diagrams.

4.3.2 Systematic uncertainties

Due to either the discreteness of the model isochrones or the rapid colour evolution of the models at certain ages in combination with the photometric uncertainties of the data, some fitting artefacts, or "chimneys" will generally appear in the log(mass) vs. log(age) plane of the clusters (Bastian et al. 2005a, Gieles et al. 2005). We find that these artefacts depend on the SSP model parameters such as the adopted isochrones and the range in metallicity. In Fig. 4.4 we compare the ages of clusters fitted with our adopted parameters (Geneva isochrones, Z free between $0.4 Z_\odot$ – $2.5 Z_\odot$) to the ages fitted with metallicity fixed to solar or using Padova isochrones.

First, Fig. 4.4 (left) shows that restricting the metallicity to be solar, leads to a more discrete distribution of ages and the exchange of clusters between the different chimneys: many clusters from the log(age/yr) = 7.2 chimney (on the x-axis) are now fitted with log(age/yr) between 7.6–8 or around 6.7 (on the y-axis), i.e. they show a

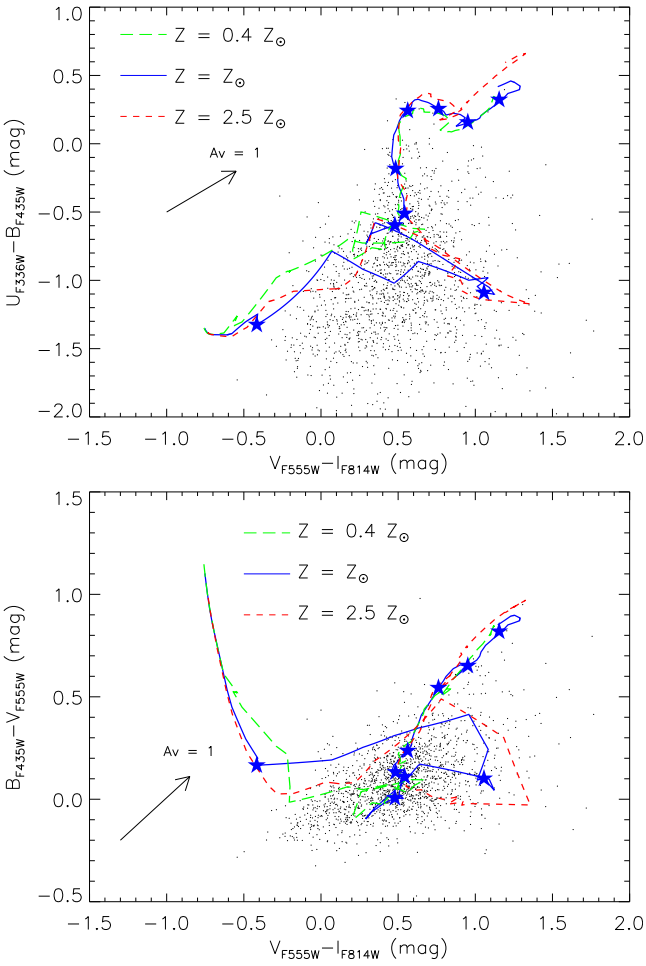

Figure 4.3: $U-B$ versus $V-I$ diagram (*top*) and $B-V$ versus $V-I$ diagram (*bottom*) of the 1580 clusters selected in Sect. 4.3.3 (not corrected for extinction), compared to GALEV SSP models using Geneva isochrones, a Kroupa IMF and three different metallicities, indicated in the figures. The stars indicate log(age/yr), starting from 6.6 (left) to 9.8 (top right) in steps of 0.4 dex.

vertical scatter. Similarly, many clusters from the range log(age/yr) = 6.7–8.0 (x-axis) end up in the log(age/yr) = 7.2 chimney (y-axis), representing the horizontal scatter.

Second, Fig. 4.4 (middle & right) shows that with the Padova isochrones we generally fit older cluster ages for log(age) $\lesssim$ 7.5 (x-axis). These panels also show the limited time resolution of the GALEV models based on Padova isochrones, in the first $\sim$ 16 Myr. This is caused by the fact that in the GALEV models the resolution can only be

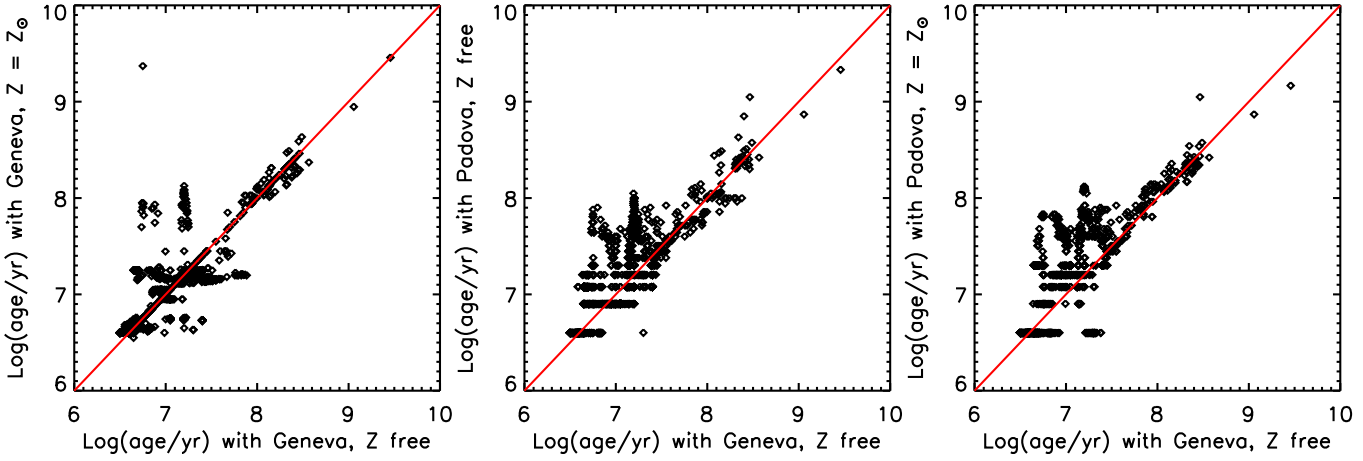

Figure 4.4: Comparison of cluster ages determined using different GALEV SSP model parameters, for the 1580 clusters selected in Sect. 4.3.3. The line shows the one-to-one correlation. **Left:** Geneva isochrones for solar metallicity versus Geneva isochrones for $Z_\odot < Z < 2.5Z_\odot$. **Middle:** Padova isochrones versus Geneva isochrones, both for $Z_\odot < Z < 2.5Z_\odot$. **Right:** Padova isochrones for solar metallicity versus Geneva isochrones for $Z_\odot < Z < 2.5Z_\odot$.

as high as the lowest possible age, which is 4 Myr when using the Padova isochrones. The preference of Geneva based models for younger ages is likely a combination of a stronger contribution from red supergiants, leading to redder colours, and the higher age resolution, which lead to less "smoothing" of the colour fluctuations compared to the Padova based models.

We conclude from Fig. 4.4 that cluster age determinations based on UBVI broad-band photometry can be very uncertain in the first $\sim$ 100 Myr due to the uncertainties in the adopted model parameters. These uncertainties will translate into uncertainties in the different age samples, which we will select in Sect. 4.3.3. Although we will use the ages based on the models using Geneva isochrones and $0.4Z_{\odot} < Z < 2.5Z_{\odot}$ as our "standard ages" in the remainder of this work, we will check, when necessary, how robust our results are against using the other models of Fig. 4.4.

4.3.3 Selection of the different age samples

After fitting the SSP models to our sample of 5502 clusters with *UBVI* photometry, we applied the following selection criteria to reject clusters with unreliable fits and to minimise incompleteness effects:

1. Photometry in B_{F435W}, V_{F555W} and I_{F814W} brighter than the 90% magnitude completeness limits determined in Chapter 2 for a source with an effective (half-light) radius of 3 pc in a high background region (respectively 24.2, 23.8 and 22.7 mag).

2. Photometric accuracy in B_{F435W}, V_{F555W}, I_{F814W} and U_{F336W} better than 0.2 mag.

These two criteria reduced our cluster sample from 5502 to 2089 clusters. Since the U_{F336W} imaging was not part of the source detection, we do not have a well defined completeness limit in the U_{F336W} passband. We can, however, make a rough estimate of the 90% completeness limit in U_{F336W}, since we performed the U_{F336W} aperture photometry at the coordinates of all resolved clusters on the B_{F435W} image. This photometry was followed by the $\sigma(U_{F336W}) < 0.2$ mag criterion. Using bins of 0.2 mag wide, we measured that the magnitude at which this $\sigma(U_{F336W})$ criterion recovers $\sim$90% of the clusters from the total sample is $U_{F336W} = 22.0$ (see also Fig. 4.2). This magnitude can be considered as a rough estimate of the U_{F336W} 90% completeness limit, since in a real completeness test the recovered fraction is measured as a function of the *input* magnitude and not of the *measured* (possibly extincted) magnitude. Also, in a proper completeness test the recovered clusters are compared to an input sample which is (by definition) 100% complete. In our case we can only measure the effect of the $\sigma(U_{F336W})$ criterion on the detected sample, which is probably already affected by some incompleteness due to extinction. Keeping this in mind, we used the estimated U_{F336W} limit as an additional criterion to select our cluster samples:

3. $U_{F336W} < 22.0$ mag,

which further reduced our sample to 1580 clusters.

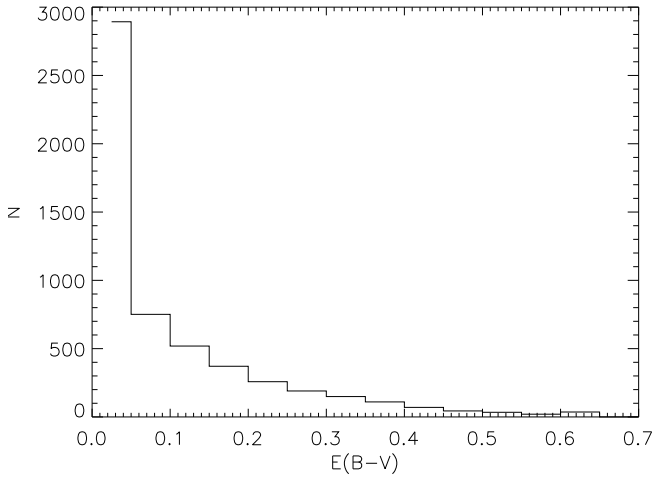

Figure 4.5: Distribution of the best-fitting extinctions ($E(B-V)$) of the 5502 clusters for which we have UBVI photometry.

To estimate the impact of an extinction induced bias, we can do the following: if we would assume that U_{F336W} = 22.0 mag is the detection limit for extinction *free* sources, we could correct the measured U_{F336W} photometry of every source according to their best-fitting extinction, before applying the magnitude cut. This would include another 271 clusters in our sample. Still, such a correction would not account for the most extincted sources, which are not detected in the first place. This shows that extinction effects can introduce biases of the order of $\sim$ 15% of the sample size. Unfortunately we have to accept that we simply *cannot* fully correct for such extinction effects by the proper choice of magnitude cuts.

The extinction distribution is shown in Fig. 4.5 and is in excellent agreement with the results of Bik et al. (2003). Since the distribution is peaked towards low extinctions, most of the additional clusters, if we could correct for extinction, would be located close to the U_{F336W} detection limit. We therefore note that, although one can use 90% completeness limits, since extinction (and also crowding, see e.g. Chapter 2) cannot properly be taken into account, one will always end up with a sample being less than 90% complete. This also holds for the remainder of this work, where we nevertheless will use terms like "90% complete" for the sake of simplicity.

The age-mass diagram for the clusters fullfilling criteria 1–3, is shown in Fig. 4.6. In this diagram two trends are immediately visible. First, we see that the mass of the most massive cluster generally increases with age. This is most likely a statistical size-of-sample effect caused by the logarithmic age interval (see e.g. Hunter et al. 2003, Gieles & Bastian 2008). Second, we see that the mass of the least massive clusters increases steadily with age. This is a selection effect caused by the detection limit (i.e. the most limiting 90% magnitude completeness limit, see criterion 1 above).

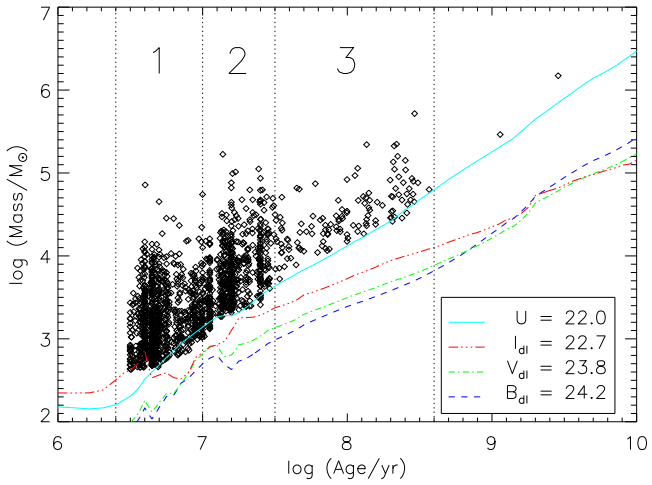

Figure 4.6: Log(mass) versus log(age) diagram of the 1580 clusters with photometric accuracies < 0.2 mag and extinction corrected magnitudes brighter than the 90% completeness limits in B_{F435W}, V_{F555W} and I_{F814W} and $U_{F336W} < 22.0$, as indicated in the lower-right corner. The corresponding mass limits as a function of age are indicated by the lines. Note that the masses are *initial* masses (i.e. corrected for stellar evolution but *not* for secular evolution). The three magnitude-limited age samples are indicated by the numbered regions.

For the *BVI* passbands we also plotted the mass evolution with age, corresponding to the 90% magnitude completeness limit. For the U_{F336W} passband we plotted the corresponding mass evolution for the applied $U_{F336W} = 22.0$ limit. We see that for log(age/yr)> 6.7 U_{F336W} is the most limiting factor that sets the lower mass limit. These mass evolution curves were calculated using GALEV models with solar metallicity. The slope of these detection limits is caused by the evolutionary fading of the clusters: a less massive cluster reaches a constant magnitude limit much faster compared to a more massive cluster. These curves show that after $\sim$ 20 Myr the limiting mass in U_{F336W} evolves faster with age compared to the other passbands, because the integrated flux in U_{F336W} is always dominated by the hottest (and therefore fastest evolving) stars. We see some clusters with best-fitted masses below the predicted limiting U_{F336W} mass. This is possible because of two effects. First, the mass of a cluster is determined by scaling of the *complete* modelled SED (i.e. *UBVI*) and not by scaling a single passband only. Second, the curve for the limiting mass is for solar metallicity, while the best-fitting model can have a different metallicity.

We selected three *magnitude-limited* cluster samples with different ages for the remainder of this study:

- Sample 1:
  $6.4 \leqslant \log(\text{age/yr}) < 7.0$
  Number of clusters: 895

- Sample 2:
  $7.0 \leqslant \log(\text{age/yr}) < 7.5$
  Number of clusters: 556

- Sample 3:
  $7.5 \leqslant \log(\text{age/yr}) < 8.6$
  Number of clusters: 127

These three cluster samples are indicated by the numbered regions in Fig. 4.6. The total number of clusters in these three samples is 1578.

Due to the systematic effects described in Sect. 4.3.2, our cluster samples will change significantly if we adopt the Padova stellar isochrones instead of the Geneva isochrones. This results in $\sim$ 230 fewer clusters in sample 1, and $\sim$ 200 additional clusters in sample 3.

As can be seen from Fig. 4.6, our cluster samples have different lower-mass limits. Our youngest cluster sample contains clusters down to estimated masses of $\log(M/M_{\odot}) \approx$ 2.6, but is 90% complete down to $\log(M/M_{\odot})$ = 3.1, while the lowest possible mass in our oldest cluster sample is $\log(M/M_{\odot}) \approx$ 3.7. An electronic table with the photometry, ages, masses and extinctions of the clusters will be published together with a forthcoming paper (Scheepmaker et al. 2009b).

4.4 Star formation rates, gas densities and spiral arms

4.4.1 Spiral arms

In order to study the relation between star and cluster formation and spiral structure, we first defined the two spiral arms in M51 using data from the *Two Micron All Sky Survey* (2MASS), which we downloaded from the *NASA/IPAC Extragalactic Database* (NED). The background subtracted *H*-band (1.65μm) image was used, which is part of the 2MASS *Large Galaxy Atlas* (Jarrett et al. 2003). We used near-infrared data to trace the spiral arms, since the near-infrared is most sensitive to older stellar populations. This means that we are tracing the dominant mass component in the disc of M51, *independent* of the dominant flux in the near-UV and optical of young star clusters and massive star formation.

We enhanced the spiral structure by first masking the companion galaxy, the inner 750 pc region, bright point sources and negative pixels. We then subtracted radial averages and convolved the resulting image with a Gaussian kernel with a FWHM of 25'' ($\approx$ 1 kpc). In the resulting smoothed image we identified 23 peaks tracing the two spiral arms using IRAF/DAOPHOT, and transformed their positions into polar coordinates. Finally, the regions in between the peaks were interpolated using cubic splines of the form $\ln(R(\theta))$. The resulting interpolated spiral arms are shown in Fig. 4.7, overplotted on the original background subtracted *H*-band image (left) and the enhanced image (right). We will refer to the arm extending towards the

south-west (i.e. bottom right) as "Spiral arm 1", and to the arm extending towards the nort-east (top left) as "Spiral arm 2", as indicated in the figure.

4.4.2 Star formation rates and gas surface densities

In a recent paper Kennicutt et al. (2007, from here on referred to as "K07") studied the locally resolved SFRs and gas densities in M51, based on Hα, Paα, CO, H I and *Spitzer Space Telescope* 24μm imaging. For a series of 257 circular apertures with a diameter of 13'' (corresponding to ~530 pc) and distributed across the disc of M51, these authors present extinction corrected SFR surface densities, as well as hydrogen gas and total gas surface densities. The SFRs are derived from the Hα line emission (after extinction correction using Paα) using the transformation from Kennicutt (1998a), and therefore trace the *current* star formation up to ~10 Myr (Calzetti et al. 2005). We used Table 1 of K07 to retrieve their list of aperture positions and the corresponding SFR surface densities and total gas surface densities.

The aperture positions were transformed to the frame of the *ACS* V_{F555W} image using the IRAF task RD2XY. In Fig. 4.8 (left) we show the resulting positions of the 13'' apertures. The mean SFR surface density in every aperture is indicated in greyscale. In the regions where two or more apertures overlap the average value was used.

4.5 Spatial distribution of star clusters and star formation

In Fig. 4.8 (right) we show the 2-dimensional spatial distribution of the three cluster samples in M51. Also shown are the interpolated spiral arms from Fig. 4.7 and the regions (white) which are covered by the *WFPC2* pointings, i.e. the regions for which we have derived ages of the clusters.

We can see from Fig. 4.8 that most current star formation is taking place in the centre of M51 and at a galactocentric radius of $\sim$ 5 kpc, and that these are also the locations where most of the young star clusters reside. We study these correlations more closely in Sect. 4.5.1 with the help of radial distributions.

Fig. 4.8 shows clearly that the majority of the clusters is closely tracing the spiral arms. This is expected, since the majority of the clusters are believed to be formed by the passing spiral density wave. Older clusters are expected to trace the spiral arms less closely, and we indeed see that the clusters from sample 3 (log(age/yr) $\geqslant$ 7.5) are more uniformly distributed. This is consistent with the result of Hwang & Lee (2008), who found that, using only the *ACS BVI* data, the bluest clusters in M51 are closely associated with the spiral structure and redder clusters are more uniformly distributed. We look at this in more detail in Sect. 4.5.2 using azimuthal distance distributions.

East (left) of the centre of M51 the clusters are more concentrated on the convex (outward) side of spiral arm 1 compared to the concave (inward) side, up to ~5 kpc. For spiral arm 2 in the south-west this effect is less obvious, although we note that for

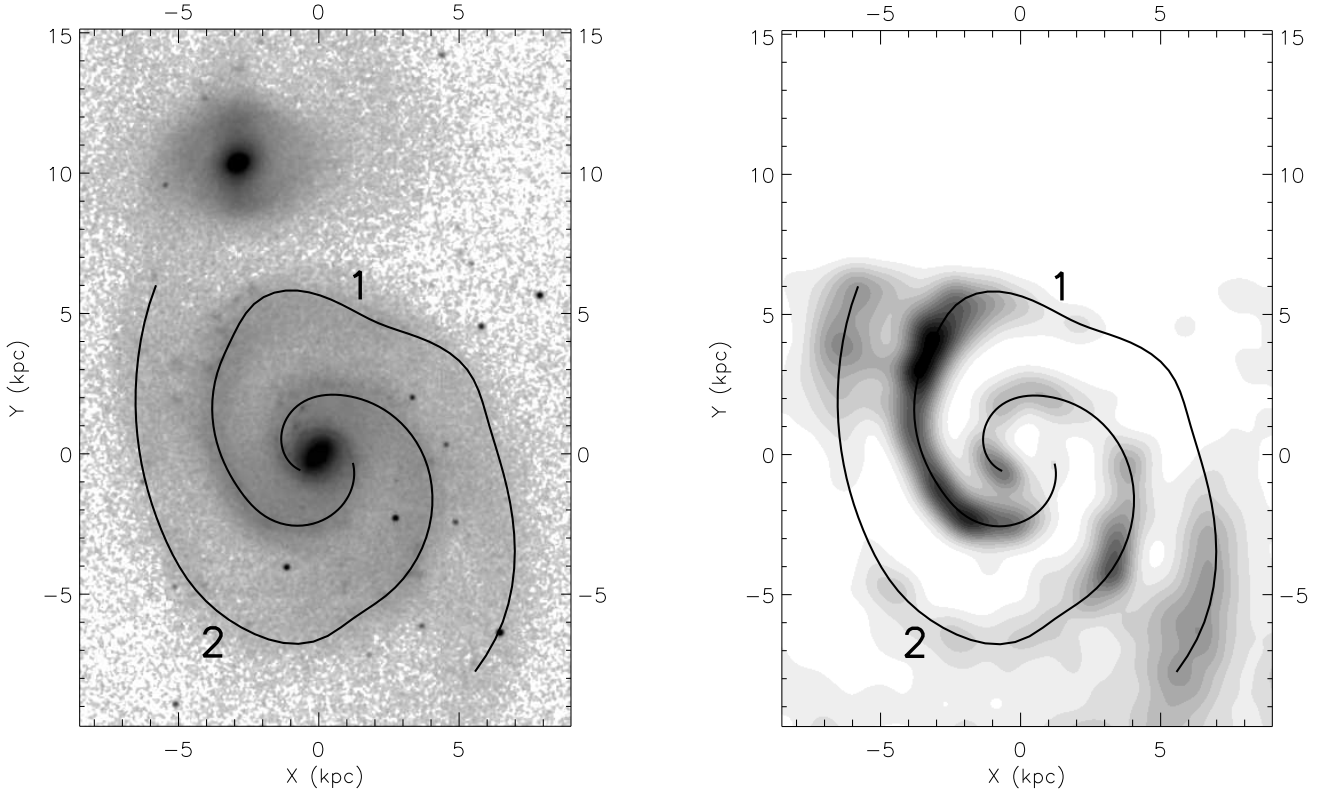

Figure 4.7: Left: Location of the two spiral arms, overlaid on the *2MASS Large Galaxy Atlas H*-band image of M51. The few black points are foreground stars. **Right:** Same spiral arms, overlaid on the enhanced (masked, radial average subtracted and smoothed) image.

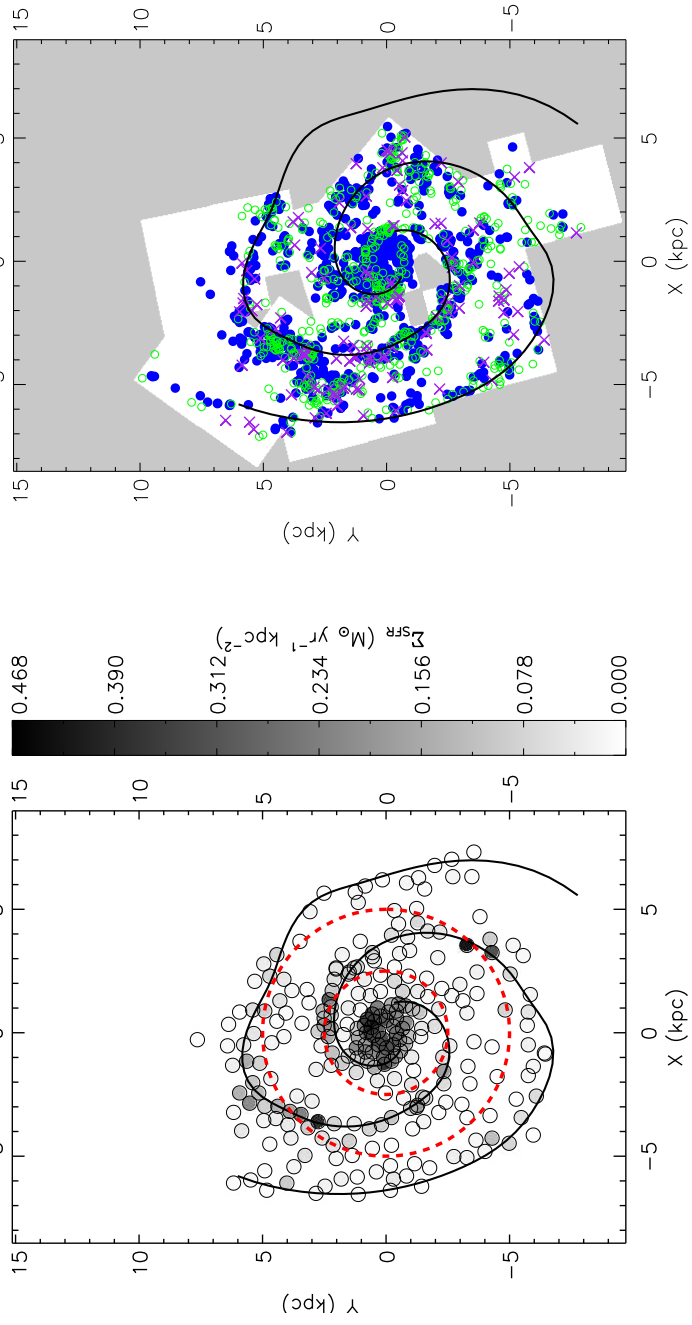

Figure 4.8: Left: Locations of the Kennicutt et al. (2007) 13″ apertures used to trace the SFR and gas surface density in M51. The greyscale indicates the mean SFR surface density. The spiral arms from Fig 4.7 are overplotted for reference. The two dashed circles are centred on the nucleus of M51 and have a radius of 2.5 and 5 kpc, respectively. **Right:** Distribution of the cluster samples with different ages across the disc of M51, in the same scale as the figure on the left. Filled blue (greyscale: black) circles: clusters with log(age/yr)< 7.0. Open green (light grey) circles: clusters with $7.0 \leqslant \log(\mathrm{age/yr}) < 7.5$. Purple (dark grey) crosses: clusters with $7.5 \leqslant \log(\mathrm{age/yr}) < 8.6$. The regions not covered by the *WFPC2* fields, i.e. for which we have no age estimation of the clusters, are indicated in grey. The spiral arms from Fig 4.7 are overplotted for reference.

spiral arm 2 we are much more hampered by selection effects due to the incomplete *WFPC2* coverage.

Fig. 4.8 also shows that the distribution of clusters itself is "clustered" in so-called cluster complexes (see e.g. Efremov 1995, Bastian et al. 2005b). These complexes are the largest groups in the hierarchy of star formation, which originates from the fractal distribution of the interstellar gas (Elmegreen & Efremov 1996, Efremov & Elmegreen 1998, Elmegreen & Elmegreen 2001). In such a hierarchy, the smallest observed structures are the youngest ones. This trend is visible in Fig. 4.8, were the spatial distribution of the youngest cluster sample shows most clustering and the amount of clustering decreases with the age of the cluster sample. We will quantify this more precisely in Sect. 4.5.3 with the help of two-point autocorrelation functions.

4.5.1 Radial distributions

From the 2-dimensional spatial distributions of SFR, gas surface densities and star clusters (Fig. 4.8) we derived radial density distributions using 13'' wide circular annuli and, in case of the clusters, masking out the regions not covered by the *WFPC2* fields (i.e. the grey area in Fig. 4.8 (right)). The SFR and gas apertures cover the entire field of view, so no masking was necessary for those. In Fig. 4.9 we compare the radial number density distributions of the different cluster samples directly to the SFR surface density distribution. Fig. 4.10 shows the radial distribution of the total gas surface density (including helium and metals), and in Fig. 4.11 we show the radial surface brightness distributions of the older stellar populations (no masking applied), derived from 2MASS *J*, *H* and *K*-band imaging (Jarrett et al. 2003). In a recent paper, Schuster et al. (2007) also presented radial distributions of SFR and gas density in M51 using 20 cm RC data for the SFR density and a combination of CO and H I data for the gas density. These distributions can be used as an independent check to the data taken from K07 and are also shown in Figs. 4.9 & 4.10. We note that Schuster et al. (2007) have corrected their distributions (i.e. the galactocentric radii) for the inclination angle of the disc of M51, while the cluster densities and the densities from K07 have only been divided by an additional factor of 1.07 to correct for the effect of the inclination on the projected area of the apertures/annuli. With an inclination angle of only 20 ° (Tully 1974), however, this difference is negligible for our purposes. Figures 4.9 & 4.10 show that the Schuster et al. (2007) distributions are smoother than the K07 distributions. This is consistent with the radio data having a lower resolution (namely a half-power beamwidth of 15'' for the SFR data and 13'' for the gas data, compared to the 13'' apertures of K07). The offset in the gas surface densities (Fig. 4.10) between K07 and Schuster et al. (2007) is probably due to differences in the conversion factors used to calculate the H_2 column density based on the CO data.

From Fig. 4.9 & 4.10 we see that both the SFR and gas density are peaking in the centre, and show two other distinct peaks at ~2.5 and ~5 kpc. These peaks are *not* simply a side effect of tracing a larger part of the spiral arms at these distances, as they are not clearly visible in the *K*-band surface brightness distribution (Fig. 4.11),

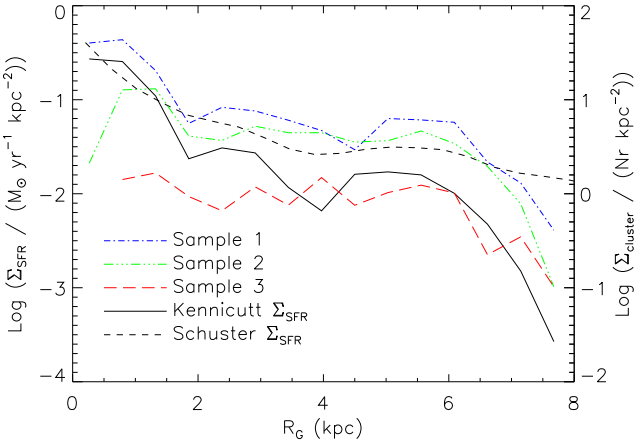

Figure 4.9: Radial number density distributions of the different cluster samples (right axis), compared to the radial distribution of the SFR surface density from Kennicutt et al. (2007) and Schuster et al. (2007) (left axis).

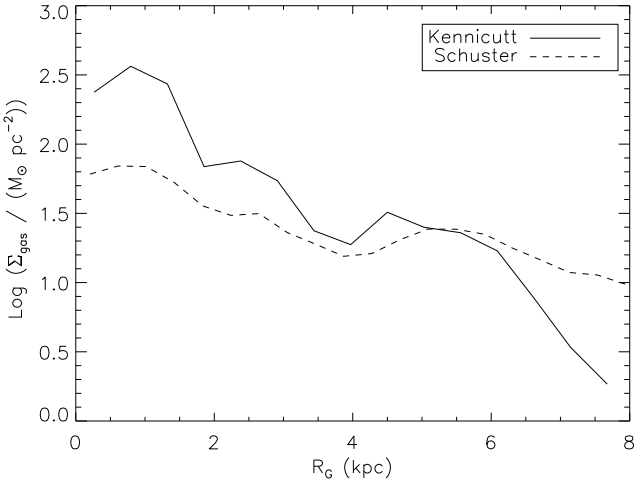

Figure 4.10: Radial distributions of the total gas (i.e. including helium and metals) surface density. The solid curve is derived from the data of Kennicutt et al. (2007), while the dashed curve is from Fig. 4 of Schuster et al. (2007).

while this band was used to define the spiral arms (Sect. 4.4.1). The locations of the peaks however, coincide with the locations of the four most active star forming regions in the spiral arms of M51, as can be seen in Fig. 4.8 (left).

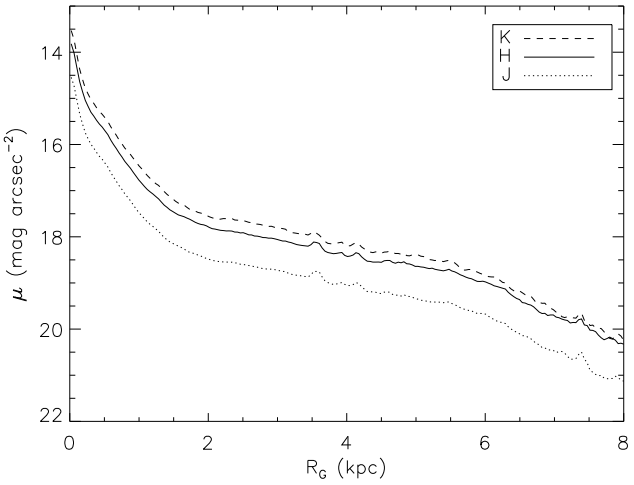

Figure 4.11: Surface brightness distribution of M51 in the 2MASS *J*, *H* and *K*-band.

We see from Fig. 4.9 that the radial distribution of clusters younger than 10 Myr (sample 1) follows the SFR density distribution to a high degree (including the 2 peaks). Sample 2 shows a much flatter distribution but is still peaking towards the centre, followed by a dip within the inner ∼1 kpc, while the oldest cluster sample (sample 3) shows a flat distribution. These conclusions hold if we would use the Padova isochrones, and it agrees very well with the results of Hwang & Lee (2008), who find peaks at ∼3 and ∼6 kpc in the radial distribution of their "class 2" clusters (i.e. clusters which are more distorted and/or have multiple neighbours) and an increasing flattening of the radial distribution with increasing cluster colour (i.e. with increasing age, although some of their reddest clusters might be very young and extincted).

The peaks in $\Sigma_{\rm SFR}$, $\Sigma_{\rm gas}$ and $\Sigma_{\rm cluster}$ at $R_{\rm G} \approx 5$ kpc are consistent with an enhanced star formation activity caused by corotation (Elmegreen et al. 1989), since the corotation radius of M51 is at $R_{\rm G} = 5.4$ kpc, assuming a circular velocity of $V = 200{\rm km\,s^{-1}}$ (García-Burillo et al. 1993) and a pattern speed of $\Omega_{\rm p} = 37{\rm km\,s^{-1}kpc^{-1}}$ (Zimmer et al. 2004). The peaks at $R_{\rm G} \approx 2.5$ kpc could be explained by the presence of the 4:1 resonance, which is were $\Omega - \kappa/4$ equals the pattern speed, Ω being the angular velocity of the stars and interstellar material and κ the epicyclic frequency (Contopoulos & Grosbøl 1986, 1988). Elmegreen et al. (1989) have found evidence for a spiral arm amplitude minimum at this resonance, consistent with the gaps, orbital loops and stellar orbit crowding, that are expected for this resonance (Contopoulos & Grosbøl 1986). It is also suggested that orbit crowding and loops result in more gas shocking. This would lead to enhanced star formation at the 4:1 resonance radius, resulting in an enhancement of $\Sigma_{\rm SFR}$ at ∼2.5 kpc, which is then followed by an enhanced $\Sigma_{\rm cluster}$ for the youngest cluster sample.

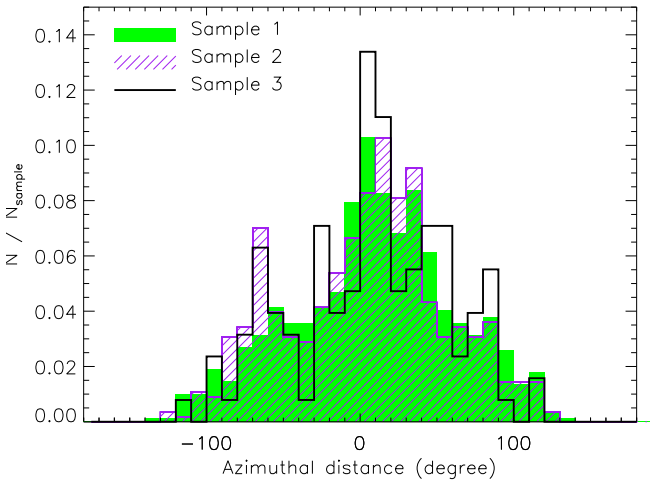

Figure 4.12: Normalised distribution of the azimuthal distance of the clusters to their closest spiral arm.

4.5.2 Azimuthal distributions

If the formation of star clusters is triggered by gas shocking due to the passing spiral density wave (Roberts 1969), we expect the youngest star clusters to be located closer to the spiral arms compared to older clusters. Using the spiral arms from Fig. 4.7, we derived for every cluster their azimuthal distance from their closest spiral arm, assuming circular orbits. No corrections for the position angle (PA) and inclination angle (i) were applied, since these will be practically negligible for the almost face-on orientation of M51 (PA = 170°, i = 20°, Tully 1974). In Fig. 4.12 we show the distribution of the azimuthal distances for the three cluster samples (sometimes referred to as the "circular distribution", e.g. Boeshaar & Hodge (1977)), normalised by the total number of clusters in every sample. The figure shows that *all* cluster samples are peaking at the location of the spiral arms (i.e. an azimuthal distance of 0°). Although the youngest clusters (sample 1) show the smoothest distribution (i.e. with least scatter) compared to the other two samples, K-S tests do *not* indicate statistically significant differences between the samples. This result is robust against the variations of the SSP model parameters, used to derive the cluster ages, as described in Sect. 4.3.2.

The fact that the oldest cluster sample peaks at the centre of the spiral arms is likely a side effect of the enhanced cluster formation around the co-rotation radius (Sect. 4.5.1). Around the co-rotation radius the drift velocity away from the spiral arms is very low, meaning that older clusters once formed in these regions are still located close to the arms. The azimuthal distance of the clusters from the spiral arms expressed in terms of "kinematic age" will therefore be a better description

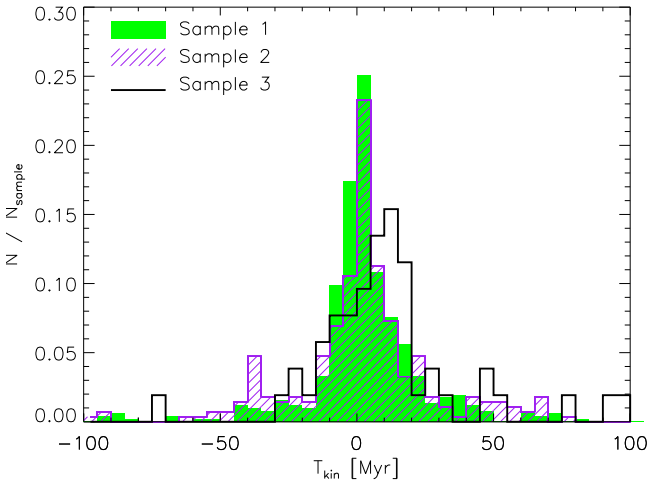

Figure 4.13: Normalised distribution of the kinematic ages of the clusters from their closest spiral arm, for the clusters with a galactocentric distance < 4 kpc.

of the differences in the circular distributions between the three cluster samples. In Fig. 4.13 we show the circular distributions in units of kinematic age, $T_{\rm kin}$, which is the azimuthal distance to the closest spiral arm, divided by the local drift velocity at the location ($R_{\rm G}$) of the cluster. A negative $T_{\rm kin}$ implies that the cluster is still approaching its closest spiral arm. In Fig. 4.13 we only plotted clusters with $R_{\rm G} < 4$ kpc, i.e. well within the co-rotation radius, since close to co-rotation $T_{\rm kin}$ will diverge and outside the co-rotation radius the "kinks" or near-circularity of the spiral arms could make the intersection of the cluster orbit and spiral arms ambiguous. Note that this prescription for $T_{\rm kin}$ does not account for the passing of multiple spiral arm, e.g. an old cluster which has passed numerous spiral arms in its orbit can still be appointed a very low kinematic age, if it currently happens to be located close to an arm.

This notwithstanding, we see in Fig. 4.13 that the oldest cluster sample peaks at older kinematic ages (10–15 Myr) compared to the younger two cluster samples, which peak at 0–5 Myr. We also see that sample 1 has a larger fraction of clusters at the youngest kinematic ages left of the peak compared to sample 2. The kinematic ages of the peaks in the distributions are younger than the typical ages of the clusters in the samples, indicating that the majority of the clusters formed $\sim$ 5–20 Myr before their parental gas cloud would have reached the centre of the spiral arm. This is in agreement with the sharp edge of the dust clouds, seen on the *HST*/*ACS* image (see e.g. the dust lane covered by fields 1 and 2 in Fig. 4.1). For a collapse time of the order of 10^6 years we expect most contracting clouds to have formed a cluster well before the centre of the spiral arm is reached. Tamburro et al. (2008) find a timescale of 3.3 Myr in M51 for the transition from H I emission, via CO emission to 24μm emission from current star formation. Since H I first has to condense to H_2, the collapse time

has to be shorter than 3.3 Myr.

The circular distributions are reasonably symmetrical around their peaks, which is consistent with the circular distributions found for H II regions in other spiral galaxies (e.g. in NGC 4321, Anderson et al. 1983) and it is in qualitative agreement with the density wave models which predict a smoother surface brightness distribution across spiral arms (e.g. Bash 1979), as opposed to the models which predict an asymmetric distribution (Roberts 1969).

4.5.3 Clustering of star clusters

The degree of clustering for different cluster samples can be quantified and compared using the two-point correlation function (Peebles 1980, § 45). Applied to clusters from the same cluster sample, the two-point correlation function becomes an autocorrelation function. In the following, we broadly follow the method described in Peebles (1980) and Zhang et al. (2001). Zhang et al. applied two-point correlation functions to star clusters in NGC 4038/39 (the "Antennae"). The autocorrelation function is defined as:

$$1 + \xi(r) = \frac{1}{\bar{n}N} \sum_{i=1}^{N} n_i(r), \tag{4.1}$$

where $n_i(r)$ is the number density of clusters found in an aperture of radius r centred on, but excluding cluster i. N is the total number of clusters and $\bar{n}$ is the average number density of clusters (excluding the grey regions in Fig. 4.8 (right)). In general, $\xi(r)$ is defined such that $\bar{n}[1 + \xi(r)]\mathrm{d}V$ is the probability of finding a neighbouring cluster in a volume $\mathrm{d}V$ within a distance of r from a random cluster in the sample (Peebles 1980). For our spatial distribution of clusters this means that $1 + \xi(r)$ is a measure of the mean surface density within radius r from a cluster, divided by the mean surface density of the total sample (i.e. the surface density enhancement within radius r w.r.t. the global mean). Therefore, a random distribution of clusters will have a constant $1 + \xi(r) = 1$, while for a clustered distribution $1 + \xi(r) > 1$.

Since the star clusters in M51 reside primarily in the disc, while the observations cover a larger projected area, all cluster samples will show some degree of autocorrelation and the absolute scaling of $1 + \xi(r)$ will be arbitrary. We can, however, compare the relative scaling of $1 + \xi(r)$ between the different cluster samples as well as the different functional forms.

In Fig. 4.14 we show the autocorrelation functions as a function of radius for the three cluster samples. Before the autocorrelation was calculated, the original *ACS* coordinates were mapped onto a new image with 1'' resolution to reduce computing time. We took into account that as a result of this binning, one pixel could contain multiple clusters. For the errorbars we used (Peebles 1980, § 49):

$$\delta(r) = \left(\frac{1}{2} \sum_{i=1}^{N} n_{\mathrm{p}}(r) \right)^{-1/2}, \tag{4.2}$$

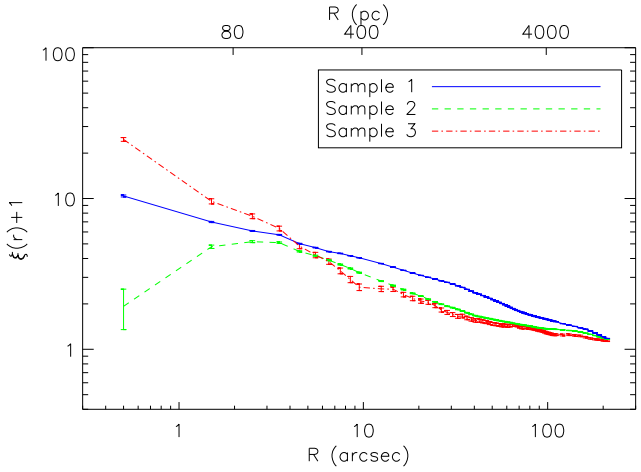

Figure 4.14: The autocorrelation function as function of radius for the three cluster samples.

where $n_p(r)$ is the number of pairs formed with the central cluster i of the current aperture, and the factor 1/2 accounts for not counting every pair twice.

Fig. 4.14 shows that for $r > 4''$ (~ 160 pc) the clusters with ages < 10 Myr (sample 1) are most clustered (largest $\xi(r)$) and that the amount of clustering decreases with age. This is consistent with the visual interpretation of Fig. 4.8 (right). This result is robust against variations in the isochrones (Padova or Geneva) or metallicity range used in the SSP model fitting of our clusters. Below $r \sim 10''$ (i.e. ~ 400 pc) we see a steady increase in the clustering of sample 3, surpassing sample 1 below $r \sim 4''$. We also see that below this radius the amount of clustering for sample 2 decreases. However, if we would use the Padova isochrones we find that the autocorrelation function of sample 3 is much flatter, while the turnover of sample 2 decreases. Due to this degeneracy, we cannot draw any firm conclusions on the age dependence of the autocorrelation function on scales below $\sim 4''$.

Moreover, on these smallest scales we may be biased by selection effects in the original sample selection of resolved sources of Scheepmaker et al. (2007). In this sample selection, sources with a neighbouring source within 5 *ACS* pixels (i.e. 0.25'') were rejected, possibly lowering the amount of autocorrelation in the first radius bin in Fig. 4.14. Crowding effects and the high background in the most compact regions in which the star clusters form, will also introduce a bias against the detection of clusters on the smallest scales. This bias will be stronger for younger clusters, since in a hierarchical (i.e. "scale free") model of star formation the youngest structures are also the most compact ones. Correcting for such biases will increase the autocorrelation function of our youngest sample (sample 1), as we will show below.

The general trend of $1 + \xi$ decreasing with radius is expected for hierarchical (i.e. "scale free" or "fractal") star formation (e.g. Gomez et al. 1993, Larson 1995,

Bate et al. 1998). If we consider a compact, isolated grouping of newly formed star clusters, we expect such a grouping to disperse with a typical velocity dispersion $< 10\ \mathrm{km\,s^{-1}}$ (Whitmore et al. 2005). For a 10 and 30 Myr old population of clusters, autocorrelation is therefore expected to increase on scales smaller than roughly 100 and 300 pc, respectively (which are lower limits, considering the initial size > 0 pc of the GMC that formed the grouping). On larger scales, the autocorrelation for an isolated grouping of clusters is expected to level off. However, this will only hold if the grouping was *not* part of a larger hierarchy of star formation. In a hierarchical model, on the other hand, the clusters will be correlated with other clusters from other groupings on larger scales, together forming a group higher up in the hierarchy of star formation. The smooth decline of $1 + \xi$ with radius, observed for our cluster samples on scales $r > 3''$, is therefore consistent with these populations being part of this hierarchy. The velocity dispersion will cause an overall decrease of the amount of clustering of the star clusters with time (Bate et al. 1998), consistent with Fig. 4.14.

For a hierarchical, or fractal, distribution of stars or clusters, the autocorrelation function will show a power-law dependency with radius of the form $1 + \xi(r) \propto r^{\eta}$ (Gomez et al. 1993). For such a distribution, the total number of clusters (N) within an aperture increases with radius as $N \propto r^{\eta} \cdot r^2 = r^{\eta+2}$, which shows that η is related to the (two-dimensional or projected) fractal dimension D_2 as $D_2 = \eta + 2$ (Mandelbrot 1983, Larson 1995). The distribution of star formation and interstellar gas over a large range of environments is observed to show a (three-dimensional) fractal dimension of $D_3 \sim 2.3$ (e.g. Elmegreen & Falgarone 1996, Elmegreen & Elmegreen 2001) Projecting this three-dimensional fractal on a plane will result in a two-dimensional fractal dimension $D_2 \approx D_3 - 1 = 1.3$ (Mandelbrot 1983, Beech 1992, Elmegreen & Elmegreen 2001). In the spiral galaxy NGC 628, Elmegreen et al. (2006) observe star-forming regions with $D_2 = 1.5$.

If we fit power laws to the straight parts of the autocorrelation functions in Fig. 4.14 ($4'' < r < 50''$), we find that the decreasing trend of sample 1 and 2 can be approximated with a power-law index of around -0.4 (fractal $D_2 = 1.6$). Sample 3 has a lower index of around -0.8 ($D_2 = 1.2$), but as mentioned before, this index depends strongly on the stellar isochrones used: using the Padova isochrones, some clusters from sample 2 are fitted with older ages (see Fig. 4.4) and move to sample 3, flattening the autocorrelation function to a power law with an index of around -0.4. Interestingly, an index of -0.4 is similar to the index Zhang et al. (2001) find for candidate young stars in the Antennae galaxies (namely an index of -0.41), while the same authors find steeper slopes for the autocorrelation functions of young (5–160 Myr) star clusters (namely indices between -0.74 and -1.06). In an attempt to minimise the possible bias due to crowding of the youngest clusters, we also determined the autocorrelation function of all clusters in sample 1 with $\log(M/M_{\odot}) > 3.7$. This sample will have a higher completeness in the densest star forming regions. For this mass-limited sample we find a power-law index of -0.8 ($D_2 = 1.2$, Geneva) or -0.7 ($D_2 = 1.3$, Padova), similar to the indices of Zhang et al. (2001) and consistent with the fractal dimension of ~ 1.3, mentioned above. This suggest that the flatter slope of the full sample 1 population of clusters is indeed biased, and that the unbiased

index of the autocorrelation function of young clusters is similar for different galaxies. In other words, this hints towards a universal fractal dimension of hierarchical star formation. More studies in different galaxies and of different nature are necessary to strengthen this point.

4.5.4 Spatial correlation between star clusters and star formation

The crosscorrelation function (Eq. 4.1) can also be used to study the correlation between star clusters and the flux from any image. We can rewrite Eq. 4.1 as:

$$1 + \xi(r) = \frac{1}{\bar{f}N} \sum_{i=1}^{N} f_i(r), \tag{4.3}$$

following Zhang et al. (2001, their Eq. 2), where $f_i(r)$ is now the intensity (i.e. flux per pixel) in an aperture with radius r centred on cluster i, and $\bar{f}$ is the mean intensity over the whole image. For both the calculation of $f_i(r)$ and $\bar{f}$ the areas not covered by *U*-band imaging are masked out. To study the crosscorrelation between star clusters and star formation, we used the 20 cm RC map (Patrikeev et al. 2006), and the *HST*/*ACS* Hα mosaic image of M51 (Mutchler et al. 2005), which we continuum subtracted using a combination of the *ACS* V_{F555W} and I_{F814W} images. The 20 cm RC map was also used by Schuster et al. (2007) to derive the radial SFR distribution (shown in Fig. 4.9). The SFRs from the apertures of Kennicutt et al. (2007) (Fig. 4.8) are not suitable for direct use in Eq. 4.3 due to their incomplete spatial sampling.

The 20 cm RC traces star formation through the synchrotron radiation from cosmic rays, emitted by supernova explosions of massive stars. The exact relation between SFR and RC emission, however, is not well defined. It depends on the scaling between RC and far-infrared dust continuum emission, of which the general form and radial dependencies are still under debate (see e.g. Helou et al. 1985, Marsh & Helou 1995, Niklas & Beck 1997, Niklas 1997, Murgia et al. 2005, Murphy et al. 2006, 2008). For our current study, however, we are not interested in the exact scaling between RC or Hα flux and SFR. We simply use the RC and Hα flux to study how star clusters and two spatially complete tracers of star formation correlate for differently aged cluster samples.

Before we applied the crosscorrelation function (Eq. 4.3) to the 20 cm RC image (shown in Fig. 4.15), the image was cropped to match the *ACS* mosaic frame and resampled to a pixel scale of 1″ (the original image had a pixel scale of 2″ and a beam size of 15″). Due to computational issues the Hα image, with a resolution of 0.05″ was binned by a factor of 10 to a pixel scale of 0.5″. For the uncertainty in $1 + \xi(r)$ we again followed Zhang et al. (2001), adopting only the statistical uncertainty in the number of clusters per sample (N), leading to:

$$\delta(r) = N^{-1/2}(1 + \xi(r)). \tag{4.4}$$

In Fig. 4.16 we show the resulting crosscorrelation functions between the three cluster samples and the RC flux. The crosscorrelation functions are flat on scales

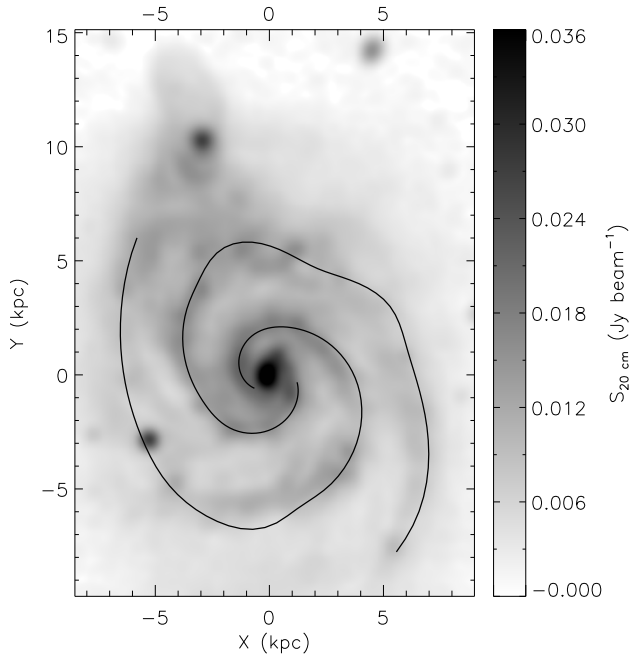

Figure 4.15: Radio continuum (20 cm) image of M51, with the spiral arms of Fig. 4.7 overplotted for reference.

$< 10''$, which is very likely a result of the beam size of the radio data. It is evident that the youngest cluster sample is most correlated (i.e. largest $\xi(r)$) with the RC emission on all scales smaller than $\sim 100''$ (i.e. ~ 4 kpc), and that the correlation drops with the age of the cluster population. A random distribution of clusters would have a constant $\xi(r) + 1 = 1$. In other words, most of the radio flux is concentrated around the youngest clusters, as expected.

The crosscorrelation function between the 20 cm RC emission and the youngest cluster sample drops to half its peak value at $R \approx 2$ kpc. This shows that the RC emission traces star formation in a very diffuse way, consistent with the long path length of the cosmic rays, before they stop emitting RC emission.

In Fig. 4.17 we show the crosscorrelation functions between the three cluster samples and the (continuum subtracted) Hα flux. The youngest clusters are strongly correlated to the Hα flux. The correlation peaks at the resolution limit of $R = 0.5'' \approx 20$ pc and drops to half the peak value at $R \approx 100$ pc. This radius is consistent with the typical expansion speed ($\sim$10 km s^{-1}) of the ionised bubbles of hot stars (e.g. Lamers & Cassinelli 1999, p. 369). At a radius larger than the typical travel distance of an Hα bubble in 10 Myr (i.e. $\sim$100 pc) the correlation is expected to level off. For sample

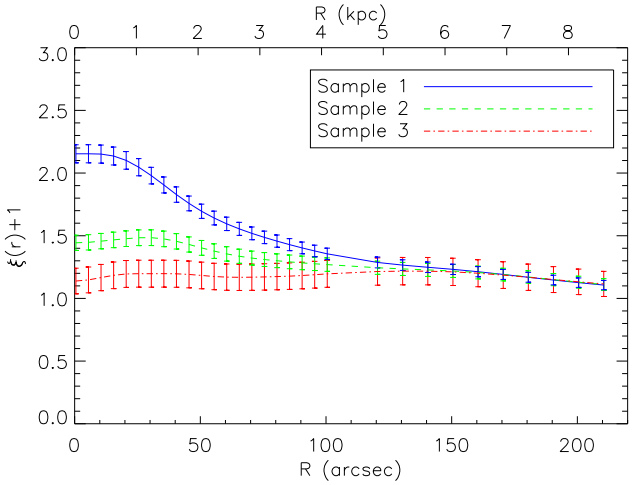

Figure 4.16: Crosscorrelation function between the three cluster samples and the 20 cm radio continuum image.

2 clusters the correlation with Hα is considerably less and the sample 3 clusters shows a crosscorrelation function with Hα consistent with a random distribution (i.e. $\xi(r) + 1 = 1$, although a slight offset from 1 is expected due the large scale structure of M51, see below).

As a consistency check, we also derived the crosscorrelation functions between the star clusters and the flux from the *2MASS H*-band image, which we used to define the spiral arms (Fig. 4.7). Since this near-infrared data is mostly tracing older stellar populations, no enhanced correlation with young star clusters is expected. In Fig. 4.18 the crosscorrelation functions are indeed shown to be indistinguishable. All three clusters samples, however, show an increased correlation towards smaller radii. This is likely an effect of the large scale structure of M51. Both the cluster and *H*-band flux density are higher in the disc and spiral arms of M51, while the observations (and thus the normalisation factor $\bar{f}$ in Eq. 4.3) cover a larger area. This leads to some degree of correlation towards smaller scales. The fact that this correlation is similar for all cluster ages confirms that the *H*-band flux is a good tracer of stellar density and not of current star formation.

4.6 Summary and conclusions

We have studied the spatial correlations between star clusters and star formation across the spiral galaxy M51. We combined published data of the resolved star formation law in M51 (SFR and gas surface densities, Kennicutt et al. 2007) with the star cluster data of Scheepmaker et al. (2007). We combined the star cluster data

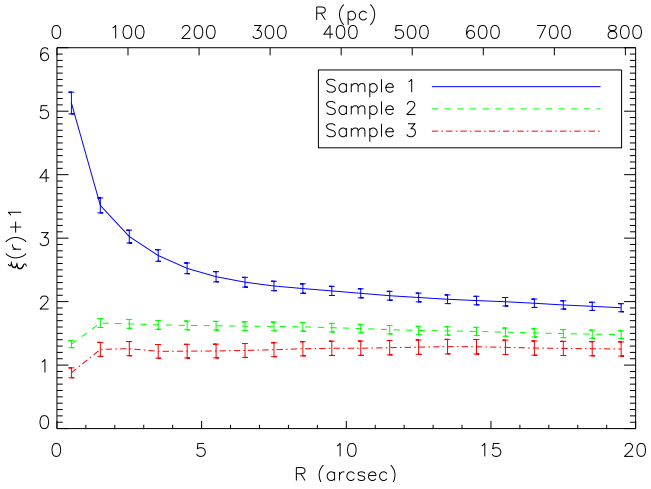

Figure 4.17: Crosscorrelation function between the three cluster samples and the (continuum subtracted) Hα image. Note the difference in X- and Y-scaling compared to Figs. 4.16 & 4.18. On a larger scale, the three curves would converge to $\xi + 1 = 1.1$ at $R \approx 120'' \approx 5$ kpc, similarly to Fig. 4.16.

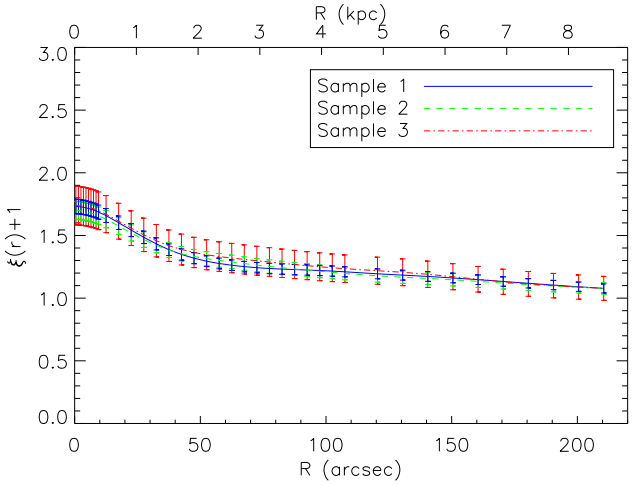

Figure 4.18: Crosscorrelation function between the three cluster samples and the *2MASS* *H*-band image of M51.

with new *HST/WFPC2* U_{F336W} data of 1580 clusters in order to estimate ages, masses and extinctions of these clusters using *SSP* models. We used radial and azimuthal distributions and cross-correlation functions to study the spatial correlation between

star formation, star clusters and spiral structure. We used auto-correlation functions to study how the clustering of star clusters depends on age and spatial scale. The main conclusions of this chapter can be summarised as follows:

1. We find that age determinations of young ($\lesssim$ 100 Myr) star clusters based on broad-band UBVI photometry can depend strongly on the adopted stellar isochrones used in the SSP models. Using models based on the Padova isochrones, we generally find older, and therefore more massive, clusters compared to the same models based on the Geneva isochrones (Fig. 4.4).

2. The radially averaged distributions of star formation and gas surface density in M51 peak in the centre and subsequently at $\sim$ 2.5 and $\sim$ 5 kpc. These distributions are matched by the number surface density distribution of our youngest star cluster sample (ages < 10 Myr, Fig. 4.9), while for the older clusters the distributions are more flat. We note that the location of the peaks coincide approximately with the locations where the spiral arms meet the 4:1 resonance and the co-rotation radius.

3. The distributions of azimuthal distances from the spiral arms show that most of the young *and old* star clusters are located at the centre of the spiral arms, with the youngest star clusters showing the most smooth distribution (Fig. 4.12). In terms of kinematic age and for $R_{\rm G}$ < 4 kpc, the azimuthal distribution of the oldest clusters peaks at the largest separation downstream of the spiral arms (10–15 Myr), while the majority of the younger clusters are within 0–5 Myr downstream of the arms. This indicates that the majority of the clusters formed $\sim$ 5–20 Myr before their parental gas cloud would have reached the centre of the spiral arm.

4. We find that the amount of clustering of star clusters decreases both with spatial scale and age (Fig. 4.14), consistent with hierarchical star formation. The slope of the autocorrelation functions of the youngest clusters (log(age) < 7.5) is consistent with a projected fractal dimension of 1.6. We find a lower fractal dimension of 1.2 for the clusters with log(age) < 7.0, if we use a higher mass limit and thus, for this smaller mass range, a more complete sample. On spatial scales smaller than 400 pc, the amount of clustering of the *oldest* cluster samples is very uncertain due to uncertainties in the assumed SSP model parameters.

5. The locations of the youngest star clusters are highly correlated with the flux from 20 cm radio-continuum emission and continuum subtracted Hα emission, but not with near-infrared *H*-band emission. The correlation with the radio emission is more diffuse compared to the correlation with Hα, and both correlations decreases with the age of the cluster population.

In the following chapter we will focus on the *quantitative* comparison between star and cluster formation, discussing the fraction of total star formation taking place in optically visible star clusters.

Acknowledgements We thank Rainer Beck, Arnold Rots and Karl Schuster for help with obtaining the radio data. Christian Struve and Alicia Berciano Alba are thanked for some helpful discussions. We thank the anonymous referee for helpful comments that improved this paper. This research has made use of observations made with the NASA/ESA *Hubble Space Telescope*, obtained from the data archive at the Space Telescope Institute. STScI is operated by the association of Universities for Research in Astronomy, Inc., under the NASA contract NAS 5-26555. This research has also made use of the NASA/IPAC Extragalactic Database (NED) which is operated by the Jet Propulsion Laboratory, California Institute of Technology, under contract with the National Aeronautics and Space Administration.

Chapter 5

The star cluster formation efficiency in M51

R. A. Scheepmaker, H. J. G. L. M. Lamers, S. S. Larsen, and P. Anders

Astronomy & Astrophysics, submitted

Abstract *Context.* It is still unclear whether or not all star formation takes place in star clusters and how many clusters disperse immediately after formation. *Aims.* We study the fraction of star formation in optically visible star clusters in M51 and how this fraction depends on environmental conditions such as galactocentric radius, the local star formation rate and spiral arm distance. *Methods.* We combine star cluster ages and masses based on *UBVI Hubble Space Telescope WFPC2* and *ACS* imaging with information on the spatially resolved star formation rates in M51 from the literature. The locations of the star clusters are matched with 200 apertures for which we have star formation rates. We define the cluster formation efficiency as the fraction of star formation taking place in clusters younger than 10 Myr. We further determine the cluster initial mass function of 437 clusters above our mass limit of $\log(M/M_\odot) = 3.2$. *Results.* The cluster initial mass function resembles a Schechter function, although the current data does not allow us to draw firm conclusions on its exact functional form. It is estimated that 49% of the total mass in clusters formed will be below our mass limit. We find that 5% of the star formation is taking place in optically visible star clusters above our mass limit, and this fraction does *not* depend on the local star formation rate, galactocentric distance or spiral arm distance. This suggests that the cluster and star formation efficiency are constant throughout M51. The relation between the mass of the most massive cluster and the resolved star formation rate can be approximated by a power law with an index of 0.70 ± 0.03, similar to what is found for complete galaxies. If we correct for selection effects we find that $\approx 20\%$ of the current star formation in M51 is taking place in star clusters. *Conclusions.* Our

results suggest that the star formation efficiency is constant throughout M51 and that $\approx 80\%$ of the star formation takes place in a either a dispersed way or in star clusters which disperse within 10 Myr.

5.1 Introduction

Star clusters are exploited extensively to study the evolution of galaxies. The prime reason for this is that important steps in this evolution are traced by star formation, and star formation leads to the formation of star clusters (e.g. Lada & Lada 2003, and references therein). Combining this with the high intrinsic brightness of star clusters, compared to most single stars, and the fact that generally they can be considered as *simple* stellar populations with a single age and metallicity, makes star clusters ideal chronometers in the evolution of galaxies.

For a complete picture, however, it is not only important to know *when* clusters, and thus stars were formed, but we also need to *how much* star formation takes place in star clusters. It is widely assumed that most, or even all, star formation takes place in an embedded, clustered form. This embedded phase is thought to last for 3–5 Myr, until the strong winds and ionizing fluxes of the first O- and B-stars, combined with the first supernovae (SNe), have expelled the residual gas (e.g. Kroupa 2002, Lada & Lada 2003, Bastian & Goodwin 2006, Goodwin & Bastian 2006). A large fraction of clusters will consequently lose so much binding energy that they disperse into field stars, a process which is dubbed "infant mortality" (Lada & Lada 2003, Whitmore 2004). The initial fraction of star formation that went into star clusters, and the fraction which is immediately lost during infant mortality are obviously important parameters to understand, if one uses star clusters as markers of star formation.

Besides, the fraction of clustered star formation and the amount of dispersion, but also their timescales and the environmental dependencies across and within galaxies can give us important insights into the process of star formation itself. For example, the mass fraction of giant molecular clouds (GMCs) that is turned into stars (i.e. the star formation efficiency, SFE) and its dependence on local gas density, pressure or galactocentric radius, is still debated (Kennicutt et al. 2007, Bigiel et al. 2008, Leroy et al. 2008). Yet the local[1] SFE puts important constraints on the form of the local star formation law, which is widely used in models of galaxy evolution to relate star formation to gas density (Mihos & Hernquist 1994, Kennicutt 1998b). Because the SFE sets the amount of residual gas which can leave the star cluster, it is correlated to the fraction of star clusters surviving infant mortality (Hills 1980). The fraction of star formation observed in the youngest star clusters (i.e. the *cluster formation efficiency*, CFE) is therefore an important tracer of the SFE (Parmentier & Fritze 2008).

Meurer et al. (1995) find that on average 20% of the UV flux of starburst galaxies comes from star clusters. de Grijs et al. (2003) find a lower limit of $\approx 35\%$ of the flux in active star forming regions in the Mice galaxies coming from star clusters. Fall et al.

[1] In this context "local" refers to a specific location in the galaxy and not solely to a location within a GMC, such as its core.

(2005) find a lower limit of 20% of the Hα flux in the Antennae galaxies associated with star clusters and/or associations. There is also evidence that in certain environments the amount of star formation taking place in star clusters is increased. Van den Bergh (1998) sees evidence in the LMC that strong shocks can enhance cluster formation relative to the rate of star formation, and that within a galaxy this can depend on position. This suggests enhanced cluster formation, or infant mortality survival, in higher density regions. Although the central regions of spiral galaxies generally show a higher gas density, Leroy et al. (2008) find a constant SFE in the centres of spiral galaxies.

In this chapter, we set out to measure the fraction of star formation in M51, taking place in optically visible star clusters. Since M51 is covered by a large set of multi wavelength data with good spatial resolution and almost full spatial sampling of the disc, it is possible to make a quantitative comparison between the resolved star formation and the mass observed in young star clusters. We then study the fraction of star formation taking place in clusters as a function of environmental conditions in M51, such as the local star formation rate, galactocentric radius and azimuthal spiral arm distance. In Chapter 4 the datasets used in this chapter were introduced, cluster ages and masses were derived and the *spatial* correlations between star and cluster formation were studied. Here we extend that work, also by presenting the cluster initial mass function derived from the new data, which we need to estimate the mass in clusters below our detection limit.

The structure of this chapter is as follows. We start with a short description of the data used in Sect. 5.2. The process of matching star formation to star clusters is described in Sect. 5.3, where we also give our definition of the CFE and the selection biases involved. The cluster initial mass function is the topic of Sect. 5.4. In Sect. 5.5 we study the CFE as a function of local star formation rate, galactocentric distance and spiral arm distance. There we also study what our results mean for the mass of the most massive observed clusters. Accounting for selection biases, we discuss the implications of our work in Sect. 5.6. We finish with our summary and main conclusions in Sect. 5.7.

5.2 Description of the data

5.2.1 Star cluster data

The star cluster data we use are described in detail in Scheepmaker et al. (2007, Chapter 2 in this thesis) and Scheepmaker et al. (2009a, Chapter 4 in this thesis). In Chapter 2 we used the *HST*/*ACS* mosaic image of M51 in B_{F435W}, V_{F555W} and I_{F814W} to select star clusters based on size measurements. In Chapter 4 these data were complemented with *HST*/*WFPC2* U_{F336W} data, and the ages, masses and extinctions of the clusters were estimated by means of *Simple Stellar Population* (SSP) model fitting, assuming Geneva stellar isochrones and a metallicity between 0.4 and 2.5 $Z_{\odot}$. For the details of the techniques used we refer the reader to the two above mentioned

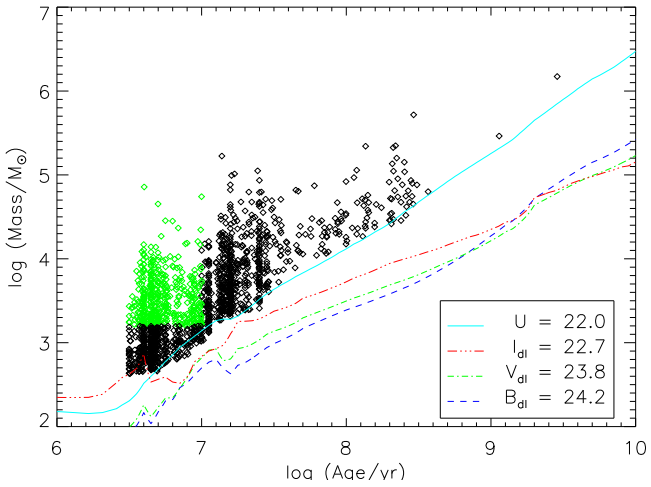

Figure 5.1: Log(initial mass) versus log(age) diagram of the 1580 clusters from Chapter 4. The mass limits (corresponding to the magnitude limits indicated in the lower-right corner) as a function of age are indicated by the coloured lines. The green (greyscale: light grey) diamonds indicate the mass limited sample of 437 young clusters with log(age/yr) < 7 and $\log(M/M_{\odot}) > 3.2$.

chapters. The resulting ages and masses of a luminosity limited sample of 1580 clusters are shown in Fig. 5.1. The data of these 1580 clusters are available in the form of an electronic table at the CDS. To give an impression of the content and the format of this table, we show the header and the first 10 rows of the table in Appendix A.

In Chapter 4 we have shown that the clusters with ages < 10 Myr are spatially correlated with the local current star formation sites throughout the disk of M51. This is also the timescale on which Hα line emission (see Sect. 5.2.2) traces star formation (Calzetti et al. 2005). For our quantitative comparison between total star formation and the mass in newly formed star clusters, we therefore select only the clusters with ages < 10 Myr. As can be seen in Fig. 5.1, the mass limit corresponding to the most limiting magnitude limit (i.e. U_{F336W} after log(age/yr) $\approx$ 6.6) is not constant, but increases with age. Therefore, in order to select a complete sample up to 10 Myr, we further selected only the clusters with $\log(M/M_{\odot}) > 3.2$. This mass limit is used in Sect. 5.4 to calculate the fraction of the total mass in young star clusters missed due to this selection limit. In the remainder of this work we will use the sample of 437 clusters with log(age/yr) < 7 and $\log(M/M_{\odot}) > 3.2$, indicated by the green diamonds in Fig. 5.1.

The spatial distribution of this cluster sample is shown in Fig. 5.2 (right). This figure (and also the figure on the left) is a reproduced version of Fig. 4.8 of Chapter 4, and shows the entire field of view of the *HST/ACS* mosaic image in grey, with the footprints of the additional *WFPC2* U_{F336W} pointings in white. The solid curves

outline the orientation of the spiral arms, as derived in Chapter 4.

5.2.2 Star formation data

For our star formation data we use the locally resolved SFRs in M51 from Kennicutt et al. (2007), which is the same data as used in Chapter 4 to study the spatial correlations between star and cluster formation in M51. This data consists of a list of 257 circular apertures with a diameter of 13'' (~530 pc for a distance to M51 of 8.4 ± 0.6 Mpc, Feldmeier et al. 1997), for which extinction-corrected SFR surface densities were derived, based on Hα, Paα and *Spitzer Space Telescope* 24μm imaging. Kennicutt et al. (2007) used the transformation from Kennicutt (1998a) to transform the Hα line emission into SFRs. The locations of the apertures are shown in Fig. 5.2 (left), in which the area-normalised SFRs are shown in greyscale.

5.3 Cluster formation efficiency

5.3.1 Matching apertures with clusters

In order to relate the amount of total star formation to the amount of star formation we observe in star clusters, we follow the straightforward approach of matching the 13'' apertures of Fig. 5.2 (left) that also have *UBVI* coverage (i.e. 200 apertures in total) with all star clusters of Fig. 5.2 (right) that are located within the apertures. For every aperture we can then define an area-normalised CFR by adding the mass of all clusters within the aperture and dividing by the age interval of 10 Myr and the area of the aperture.

We note that Kennicutt et al. (2007) based their SFR measurements on the calibration of Kennicutt (1998a), who assumed a Salpeter stellar IMF. Our clusters, however, have estimated masses based on assuming a Kroupa IMF. This underestimates the cluster masses, and therefore also the CFRs, compared to measurements that would assume a Salpeter IMF. In order to compare the SFRs and CFRs for the same underlying stellar IMF, we multiplied the cluster masses by a factor 1.38. This factor is found by calculating for both IMFs the mass fraction below $0.5 M_{\odot}$ and assuming that the mass above $0.5 M_{\odot}$ is the same for both IMFs, ignoring the slight difference in the slope of the Kroupa and Salpeter IMFs above $0.5 M_{\odot}$.

We sort the apertures in 10 bins of 20 apertures each, so that every bin has a reasonable amount of young star clusters covered to improve our statistics. Depending on the correlation studied, we sort the apertures either in SFR, galactocentric radius ($R_{\rm G}$) or kinematic age ($T_{\rm kin}$, i.e. "travel time" from the nearest spiral arm, see Sect. 5.5.2). Finally, we derive for every bin the mean area-normalised SFR, CFR, $R_{\rm G}$ or $T_{\rm kin}$.

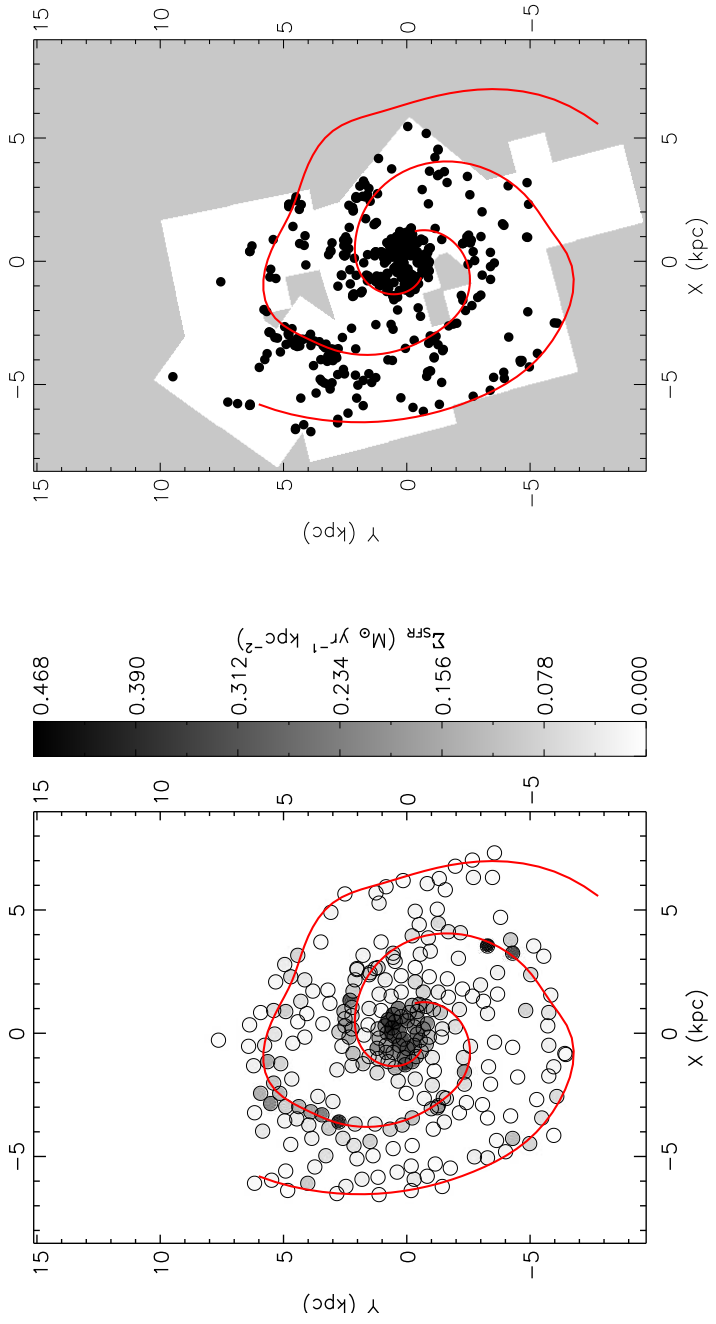

Figure 5.2: Left: Locations of the Kennicutt et al. (2007) 13″ apertures used to trace the SFR surface density in M51 (indicated in greyscale). **Right:** Distribution of the mass limited young cluster sample (i.e. log(age/yr) < 7 and $\log(M/M_{\odot}) > 3.2$ on the same scale as the figure on the left. The regions not covered by the *WFPC2* fields, i.e. for which we have no age and mass estimation of the clusters, are indicated in grey. The spiral arms, as derived in Chapter 4, are overplotted for reference.

5.3.2 The CFE

To study the fraction of total star formation taking place in visually observable star clusters, we define the *Cluster Formation Efficiency* (CFE) as

$$\mathrm{CFE} \equiv \frac{\mathrm{CFR}}{\mathrm{SFR}}. \tag{5.1}$$

Our definition of the CFE is equivalent to the parameter Γ in Bastian (2008). Note that in other work this terminology can slightly differ. Parmentier & Fritze (2008) use e.g. the term CFE to describe the ratio of total mass in stars bound to the clusters over the total mass in the parental cloud core (their ϵ_{cl}), while their cluster-to-star mass ratio M_{cl}/M_{st} is equivalent to our definition of the CFE (Eq. 5.1).

There is an important difference between the true fraction of star formation that initially takes place in the form of embedded clusters, which we refer to as $\mathrm{CFE}_{\mathrm{true}}$, and the fraction of these embedded clusters that is actually observed as clusters "immediately" after the embedded phase (e.g. our selected clusters with ages < 10 Myr). We refer to this latter fraction as $\mathrm{CFE}_{\mathrm{obs}}$, and this will always be lower than $\mathrm{CFE}_{\mathrm{true}}$ since:

1. A certain fraction of clusters will immediately disperse together with the expulsion of residual gas. We refer to the fraction of clusters observable as a "bound" cluster immediately after the embedded phase as f_{bound}.

2. Only a certain fraction of these remaining clusters will be above our detection limit. We refer to this fraction as f_{lim}.

3. Due to extinction, confusion and crowding effects, and limitations in the cluster selection techniques, even some clusters that would intrinsically lie above the detection limit, will be missed in the detection. We will refer to the fraction of clusters above the detection limit that is actually detected as f_{det}.

We therefore find that

$$\mathrm{CFE}_{\mathrm{obs}} = \mathrm{CFE}_{\mathrm{true}} \cdot f_{\mathrm{bound}} \cdot f_{\mathrm{lim}} \cdot f_{\mathrm{det}}. \tag{5.2}$$

Ultimately, one would like to constrain both $\mathrm{CFE}_{\mathrm{true}}$ and f_{bound}. However, using visually observable star clusters it is impossible to measure both parameters independently, since we cannot observe the fraction of star formation taking place in embedded clusters. As a first step, however, we can constrain the product $\mathrm{CFE}_{\mathrm{true}} \cdot f_{\mathrm{bound}}$ by measuring $\mathrm{CFE}_{\mathrm{obs}}$ and estimating both f_{lim} and f_{det}.

Tests with artificial cluster samples provide us with a good estimate of f_{det}. Such tests by Scheepmaker et al. (2007, Chapter 2 in this thesis) have shown that due to crowding and confusion effects alone ∼ 30% of the visually observable clusters are lost in the high background regions (i.e. close to the spiral arms where most young star clusters reside), and it is expected that this fraction is even higher if one includes extinction and visual inspection. These results suggest an upper limit for f_{det} of ∼ 70%. If we also consider that about 30% of the clusters in the first 10 Myr are still

in their embedded phase (which lasts $\sim$ 3 Myr, Lada & Lada 2003), an optimistic estimate for $f_{\rm det} \approx 49\%$.

The fraction of mass in star clusters above a mass limit, $f_{\rm lim}$, depends on the shape of the cluster mass function and will be derived in Sect. 5.4. In Sect. 5.5 we study the $\mathrm{CFE_{obs}}$. We combine these with our estimated $f_{\rm det}$ and $f_{\rm lim}$ in Sect. 5.6 in order to draw conclusions on the product $\mathrm{CFE_{true}} \cdot f_{\rm bound}$.

5.4 The cluster initial mass function

In a comparison between the *total* current star formation and the star formation taking place in *visually observable* young star clusters, one has to take into account that a certain fraction of the mass in clusters will be formed below the detection limit. This fraction depends on the shape of the cluster initial mass function (CIMF) and the applied lower mass limit. For a wide range of galaxy environments, the CIMF can be approximated by a power law of the form

$$\frac{\mathrm{d}N}{\mathrm{d}M} = CM^{-\alpha}, \tag{5.3}$$

with C being a constant and an index $\alpha \approx 2$ (e.g. Zhang & Fall 1999, de Grijs et al. 2003c, Bik et al. 2003, Gieles et al. 2006a), which is also expected from theoretical considerations (Elmegreen & Efremov 1997). In Fig. 5.3 we show the CIMF of 437 clusters with ages < 10 Myr and $\log(M/M_\odot) > 3.2$ (the green sample in Fig. 5.1). Below this mass limit incompleteness effects start to affect the lower end of the mass function. We find that the overall shape of the CIMF can *not* be well fitted with a single power law with $\alpha = 2$. Although the slope of the CIMF below $\log(M/M_\odot) \approx 3.8$ resembles a power law with $\alpha = 2.0 \pm 0.2$, above this mass the CIMF falls off steeper, approaching a power law with $\alpha = 3.0 \pm 0.2$. In Fig. 5.3 these power laws are shown, intersecting at $\log M/M_\odot = 3.8$ but with an arbitrary shift in the y-direction. This suggests that such a broken power law is a reasonable approximation of the CIMF. In their study of the luminosity function, Gieles et al. (2006b) have shown that a Schechter function (Schechter 1976) appears very similar to a broken power law, with the advantage that a Schechter function only has two free parameters (not considering the normalisation), while a broken power law has three (namely two indices and the location of the "knee"). A Schechter function can be considered as a power law with an exponentially decreasing high-mass end, and has the form

$$\frac{\mathrm{d}N}{\mathrm{d}M} = CM^{-\beta}e^{-M/M_\star}. \tag{5.4}$$

$M_\star$ is the mass at which the function decreases to a fraction of $1/e$ compared to a power law with an index of $-\beta$.

A maximum-likelihood fit to our data of the form of Eq. 5.4 results in $M_\star = 2.2 \pm 1.8 \times 10^4 M_\odot$ and $\beta = 1.9 \pm 0.3$. In Fig. 5.3 this best fit is overplotted, and in Fig. 5.4 we also show a cumulative CIMF with this best-fitting Schechter function

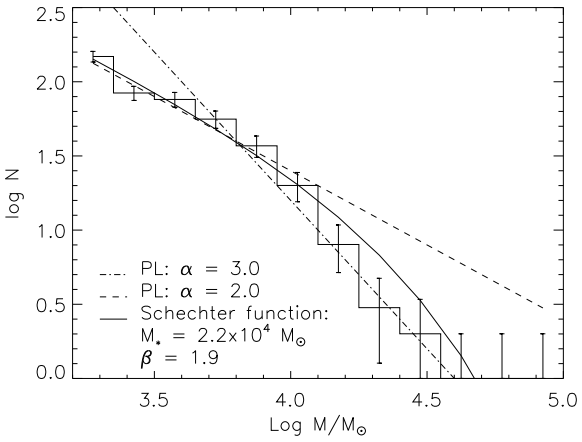

Figure 5.3: Initial mass function (assuming a Kroupa stellar IMF) of 437 clusters with ages < 10 Myr and $\log(M/M_\odot) > 3.2$. The curve is the best-fitting Schechter function, which has $M_\star = 2.2 \times 10^4$ and $\beta = 1.9$.

overplotted. A K-S test for this fit gives a probability statistic (P-value) of 0.66, meaning that the probability of observing a deviation from this Schechter function at least as large as our data, purely due to stochasticity, is 66%. A single power law with an index of -2.0 resulted in a P-value of 0.0002, which means it is not consistent with the data. However, a power law with an index of -2.2 resulted in a P-value of 0.16, which means that formally such a steeper power law cannot be rejected. As an additional check we also fitted a Schechter function to the CIMF based on Padova isochrones, which did not lead to significantly different results compared to using Geneva isochrones.

Our best-fitting Schechter function has an $M_\star$ which is considerably smaller than the results from modelling the luminosity function of M51 (which give $M_\star \approx 1 \times 10^5 M_\odot$, Gieles et al. 2006b). Part of this discrepancy can be explained by the difference in the adopted IMF, as we already mentioned in Sect. 5.3.1. For Fig. 5.3 and our maximum-likelihood fit we adopted a Kroupa IMF, which underestimates all masses by a factor of 1.38 compared to a Salpeter IMF. If we would adopt a Salpeter IMF, our best-fitting Schechter function would have $M_\star = 0.3 \times 10^5 M_\odot$ and a K-S test for a Schechter function with an $M_\star = 1 \times 10^5 M_\odot$ would give a P-value of 0.19. This formally means that such a higher $M_\star$ Schechter function can *not* be rejected based on the current data.

From Fig. 5.1 we see that a Schechter function with $M_\star = 2.2 \times 10^4$ cannot be a good representation of the complete cluster mass function in M51, as there are many clusters with higher masses at ages > 10 Myr. If we increase our age limit to $\log(\text{age/yr}) = 7.5$ and our mass limit to $\log(M/M_\odot) = 3.6$ to have a mass limited sam-

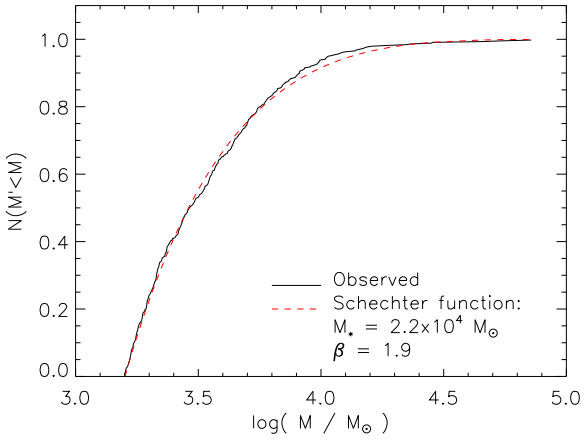

Figure 5.4: Normalised cumulative cluster initial mass function (assuming a Kroupa stellar IMF) of 437 clusters with ages < 10 Myr and $\log(M/M_\odot) > 3.2$. The dashed curve is the best-fitting Schechter function, which has $M_\star = 2.2 \times 10^4$ and $\beta = 1.9$.

ple, we find a best-fitting Schechter function with $M_\star = 7.7 \pm 0.2 \times 10^4 M_\odot$ (assuming a Kroupa IMF, for a Salpeter IMF $M_\star = 1.1 \pm 0.3 \times 10^5 M_\odot$) and $\beta = 1.9 \pm 0.2$. This shows that the mass function up to ~30 Myr is consistent with the higher $M_\star$ values from Gieles et al. (2006b).

These results suggest that, although a Schechter function is a better description of the CIMF in M51 compared to a single power law, there are possibly some selection effects present which lead to an underabundance of clusters between $\log(M/M_\odot) \approx$ 4.0–5.0 in the first 10 Myr. Although we checked the robustness of the CIMF against the use of different isochrones, additional systematic uncertainties in the assumed SSP model parameters could be present. Due to the fading of clusters with age, an overestimation of the age of a cluster also means an overestimation of its mass, and vice versa. Also the visual inspection of the initial resolved cluster sample in Chapter 2 could have introduced some selection biases. Future detailed studies on the CIMF in M51 might shed more light on these issues. At this point we conclude that a Schechter function with $M_\star = 2.2 \pm 1.6 \times 10^4 M_\odot$ and $\beta = 1.9 \pm 0.2$ is the best simple approximation of the CIMF in M51, but that a value of $M_\star = 1 \times 10^5 M_\odot$ (derived from the luminosity function) cannot be excluded.

Assuming such a Schechter CIMF, we calculate the fraction of the total mass of a star cluster population above our mass limit of $\log(M_{\rm lim}/M_\odot) = 3.2$. This depends on the minimum mass $M_{\rm min}$, since for the total mass of the population we have

$$M_{\rm tot} = \int_{M_{\rm min}}^{\infty} C M^{1-\beta} e^{-M/M_\star} {\rm d}M$$

$$= \quad CM_{\rm min}^{2-\beta} E_{\beta-1}\left(\frac{M_{\rm min}}{M_\star}\right), \tag{5.5}$$

in which $E_n(x)$ is the exponential integral, defined as

$$E_n(x) = \int_1^\infty \frac{e^{-xt}}{t^n}{\rm d}t. \tag{5.6}$$

Unless mentioned otherwise, we will use $M_{\rm min} = 100 M_\odot$, considered to be the canonical value for the lower limit of the CIMF. The same integration gives us for the mass above $M_{\rm lim}$:

$$M(> M_{\rm lim}) = CM_{\rm lim}^{2-\beta} E_{\beta-1}\left(\frac{M_{\rm lim}}{M_\star}\right). \tag{5.7}$$

For $\log(M_{\rm lim}/M_\odot) = 3.2$ and the best-fitting values from above, $\beta = 1.9$ and $M_\star = 2.2 \times 10^4 M_\odot$, this gives us for the mass fraction *above* our mass limit

$$f_{\rm lim} \equiv \frac{M(> M_{\rm lim})}{M_{\rm tot}} = 0.51, \tag{5.8}$$

indicating that 49% of the total mass formed in clusters will be below our mass limit. If one would use $M_{\rm min} = 5 M_\odot$, $f_{\rm lim} = 0.36$ and respectively 64% of the cluster mass will be below our mass limit. For a Schechter function with $\beta = 2.0$ and $M_\star = 1 \times 10^5 M_\odot$, $f_{\rm lim} = 0.57$. The fraction $f_{\rm lim}$ will be used in Sect. 5.6 to correct $\Gamma_{\rm obs}$ for selection effects. First, however, we will study $\Gamma_{\rm obs}$ itself.

5.5 Correlations between SFR and CFR: the observed CFE

5.5.1 Cluster formation vs. star formation

In Fig. 5.5 we show the area-normalised CFR ($\Sigma_{\rm CFR}$) versus the area-normalised SFR ($\Sigma_{\rm SFR}$), for the (binned) apertures sorted in SFR. The correlation is very tight and can be approximated by a power law of the form $\Sigma_{\rm CFR} \propto \Sigma_{\rm SFR}^{\eta}$ with $\eta = 0.94 \pm 0.06$. We note that this is for the mass limited sample (green diamonds in Fig. 5.1) and only for the mass in clusters we observe.

Fig. 5.6 shows the corresponding $\Gamma_{\rm obs}$ versus SFR relation, which can be approximated by

$$\Gamma_{\rm obs} = (0.046 \pm 0.006) \times \Sigma_{\rm SFR}^{-0.07 \pm 0.06}. \tag{5.9}$$

This shows that the observed CFE marginally decreases with SFR, but is practically constant at a weighted mean of $\Gamma_{\rm obs} \approx 5.0 \pm 0.2\%$. However, theory (e.g. Elmegreen & Efremov 1997, Elmegreen 2008) predicts that the local *star* formation efficiency (SFE) in the cloud cores should increase with ambient pressure and thus with gas density ($\Sigma_{\rm gas}$) and SFR. Simply applying the resolved Schmidt-Kennicutt law for M51 ($\Sigma_{\rm SFR} \propto \Sigma_{\rm gas}^{1.56}$,

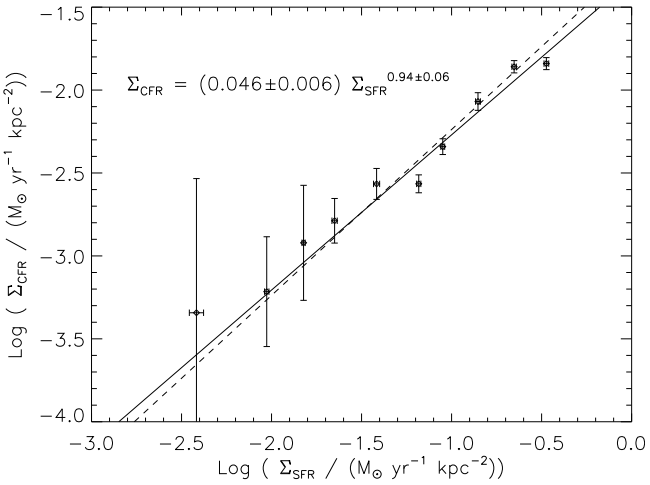

Figure 5.5: CFR surface density versus SFR surface density. The solid line is the best-fitting power law. The dashed line is for reference and has a slope of 1.

Kennicutt et al. 2007) would predict SFE $\propto \Sigma_{SFR}/\Sigma_{gas} \propto \Sigma_{SFR}^{0.36}$. With a higher star formation efficiency in regions with more star formation, less residual gas can be expelled from the star formation site and one might expect to find more star clusters and thus a higher CFE. However, this is *not* what we observe in Fig 5.6. This suggests that either the theory has to be improved and that the SFE is constant over roughly two orders of magnitude in SFR, or there is a mechanism at work which decouples the observed CFE from the SFE, in other words, which leads to less clusters being detected in the regions with higher SFR.

We note that in a recent study Leroy et al. (2008) find evidence that in the central few kpc's of a sample of 7 nearby spiral galaxies, including M51, the SFE is constant with gas surface density, which in those regions is dominated by H_2 gas. In fact, this can be considered as a consequence of the power law relation between Σ_{SFR} and Σ_{H2} with an index of 1.0 ± 0.2 found by Bigiel et al. (2008) using the same data as Leroy et al. (2008). With this index of 1.0, the local SFE will not only be constant with gas density, but also with Σ_{SFR}. Under the assumption that the CFE should follow the SFE, the results of Leroy et al. (2008) and Bigiel et al. (2008) are therefore more consistent with our data than the resolved Schmidt-Kennicutt law of Kennicutt et al. (2007). This is quite remarkable considering that the datasets used are the same, the only difference being the methods applied (pixel-by-pixel comparison by Bigiel et al. 2008 and Leroy et al. 2008 and apertures by Kennicutt et al. 2007).

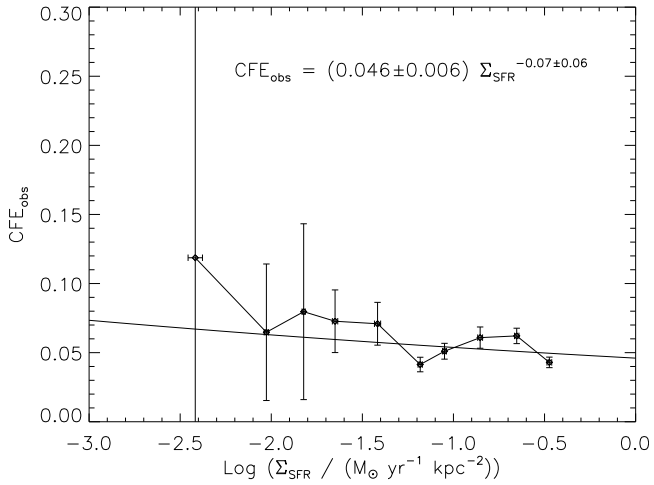

Figure 5.6: The Cluster Formation Efficiency ($\mathrm{CFE_{obs}}$) versus SFR surface density, for the observed (mass limited) cluster sample. The solid line is the best-fitting power law.

5.5.2 Galactocentric radius and spiral arm distance

In Fig. 5.7 we show how the CFR and SFR vary with galactocentric radius (R_G). The top curve shows an enhanced star formation activity towards the centre and two peaks at $\sim$ 2.5 and $\sim$ 5 kpc. This was also found in Chapter 4 using the same data, but by averaging over circular annuli around the centre of M51 instead of over the apertures themselves. In Chapter 4 we also found that the youngest (magnitude limited) sample of star clusters is following a similar distribution in terms of number density, and in Fig. 5.7 we find that also in terms of CFR of a mass limited sample (the dashed curve) the clusters follow a similar distribution, although the peaks are less pronounced (or even absent at $R_\mathrm{G} \sim 2.5$ kpc). This translates into a $\mathrm{CFE_{obs}}$ distribution, shown in Fig. 5.8, which is practically flat with R_G within the rather large errors. The SFR peaks being less pronounced in CFR causes the $\mathrm{CFE_{obs}}$ to be slightly lower at the locations of the peaks and at the centre of M51, locations where the background and the level of crowding are relatively high. So possibly the slight anti-correlation between SFR and $\mathrm{CFE_{obs}}$ is a bias due to an increased amount of confusion. However, since the "dips" in $\mathrm{CFE_{obs}}$ are only significant at a ~1–2 sigma level, *we conclude that there is no strong dependence of* $\mathrm{CFE_{obs}}$ *on* R_G.

In order to study the SFR and CFR as a function of the azimuthal spiral arm distance we determined for every aperture the azimuthal separation from its closest spiral arm. For this we assumed circular orbits and we used the spiral arms shown in Fig. 5.2. We express the azimuthal separation in terms of the kinematic age (T_kin) by dividing the azimuthal distance by the relative drift velocity at the galactocentric radius of every aperture by assuming a constant rotational velocity of $V = 200\,\mathrm{km\,s^{-1}}$

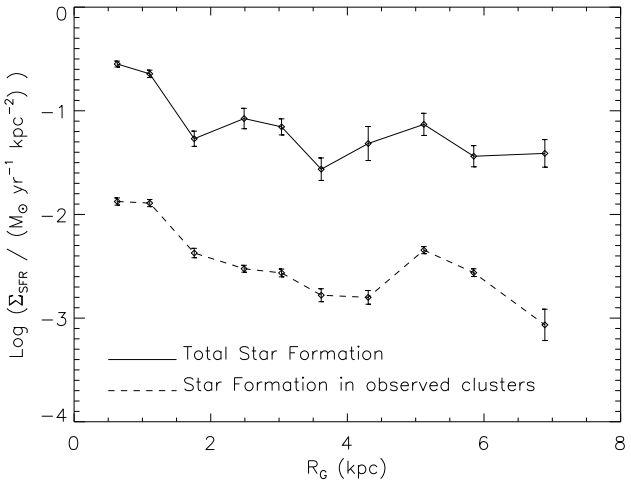

Figure 5.7: SFR and CFR versus galactocentric radius.

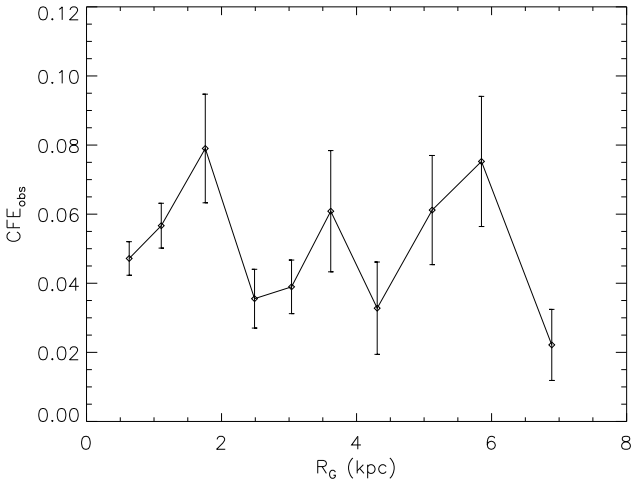

Figure 5.8: CFE_{obs} versus galactocentric radius.

(García-Burillo et al. 1993) and a pattern speed of Ω_p = 37 km s^{-1} kpc^{-1} (Zimmer et al. 2004). The kinematic age can be negative, indicating that the material in the aperture is actually approaching its closest spiral arm, instead of drifting away from it.

In Chapter 4 it was found that the number distribution of young star clusters within the co-rotation radius peaks at a T_{kin} between 0–5 Myr. In Fig. 5.9 we show the SFR and CFR as a function of T_{kin} for the apertures with R_G between 1.17–5 kpc.

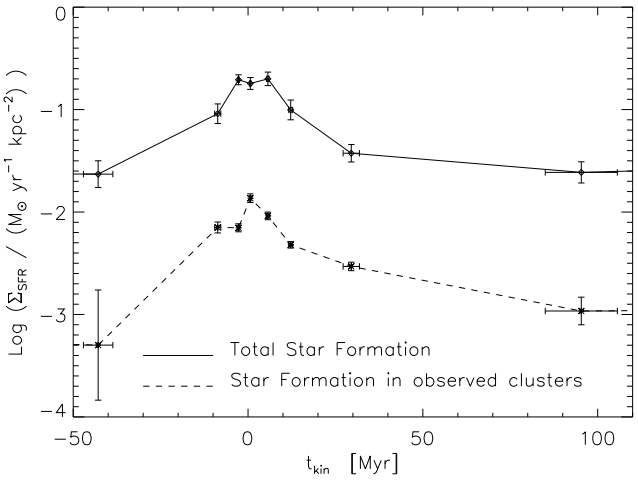

Figure 5.9: SFR (top) and CFR (bottom) versus the (binned) kinematic age $T_{\rm kin}$, for apertures between 1.17–5 kpc. A negative kinematic age means that the apertures are approaching their closest spiral arm.

Outside this range the spiral arms are either not defined or nearly circular, causing $T_{\rm kin}$ to be poorly defined in those areas. The figure shows that both the SFR and the CFR peak at $T_{\rm kin} \approx 0$ Myr, which is at the centre of the spiral arms, and that the circular distributions are reasonably symmetrical around their peaks, with the tails decreasing more slowly towards positive $T_{\rm kin}$. This is consistent with the azimuthal number distribution of young clusters of Chapter 4, and it indicates that most star and cluster formation is triggered while the material is still approaching the central, densest region of the spiral arms. *Since both curves for the SFR and CFR are similar, the* $\mathrm{CFE_{obs}}$ *does not depend on the azimuthal arm distance.*

In order to quantify the decrease of the SFR and CFR with $T_{\rm kin}$, we plot both curves again in Fig. 5.10, but now only for apertures with a positive $T_{\rm kin}$ from their closest arm (note that on the abscissa is now $\log(T_{\rm kin})$). Both SFR and CFR show a decreasing trend with $T_{\rm kin}$ that can reasonably be approximated by power laws with an index of, respectively, -0.57 ± 0.10 and -0.54 ± 0.06. A similar power-law index, namely -0.63 ± 0.07 is found (but not shown) if one would use the gas surface density instead of the SFR from the data of Kennicutt et al. (2007). This is somewhat remarkable, since according to the local resolved Schmidt-Kennicutt law derived from this data ($\Sigma_{\rm SFR} \propto \Sigma_{\rm gas}^{1.56}$, Kennicutt et al. 2007) the gas density should show a flatter distribution with a power-law index of around $-0.57/1.56 = -0.37$. However, the local Schmidt-Kennicutt law for M51 shows a significant scatter, and possibly it breaks down during the sorting, binning and averaging that we performed on the data. Also, as we already noted in Sect. 5.5.1, Bigiel et al. (2008) apply a pixel-by-pixel method to the same data, resulting in a much flatter Schmidt-Kennicutt law

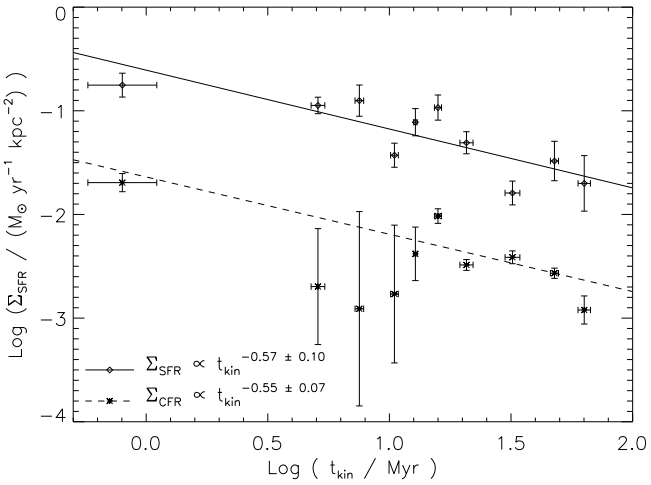

Figure 5.10: SFR (top) and CFR (bottom) versus log($T_{\rm kin}$) for apertures between 1.17–5 kpc which are downstream of their (azimuthally) closest spiral arm. The best-fitting power laws to both decreasing trends are indicated.

compared to Kennicutt et al. (2007) and one which is more consistent with our data.

5.5.3 The maximum cluster mass

The mass of the most massive cluster ($M_{\rm max}$) has proven to be a valuable tool in studies concerning the shape of the CIMF (Larsen 2002, Weidner et al. 2004, Larsen 2008), the star formation history of galaxies (Maschberger & Kroupa 2007) and star cluster disruption (Gieles & Bastian 2008). These studies are all based on relations between $M_{\rm max}$ and either the galaxy's global SFR or the age range sampled. In this work we have a fixed age range of Δt = 10 Myr, and in the following we study if $M_{\rm max}$ is also correlated with SFR on *local* scales within a single galaxy.

We first sorted the apertures in SFR and then binned these in 10 bins of 20 apertures each. For every bin we find the *total* SFR by adding all area-normalised SFRs of the apertures in the bin, and multipliying this by the total area of these apertures. This total SFR is related to the total mass in star clusters through

$$M_{\rm tot} = {\rm CFR} \cdot \Delta t = \frac{{\rm CFE}_{\rm obs}}{f_{\rm lim}} \cdot {\rm SFR} \cdot \Delta t \approx 0.098 \cdot {\rm SFR} \cdot \Delta t, \tag{5.10}$$

where we used the mean observed ${\rm CFE}_{\rm obs}$ = 5% from Sect. 5.5.1, corrected for the fraction of cluster mass below our mass limit (i.e. $f_{\rm lim}$ = 0.51, see Sect. 5.4). Since we do not correct ${\rm CFE}_{\rm obs}$ for $f_{\rm det}$ or $f_{\rm bound}$, Eq. 5.10 gives the total mass in star clusters which are *not embedded or blended, nor immediately dispersed after gas expulsion* (the total mass including such star clusters would be a factor $(f_{\rm det} \cdot f_{\rm bound})^{-1}$ higher).

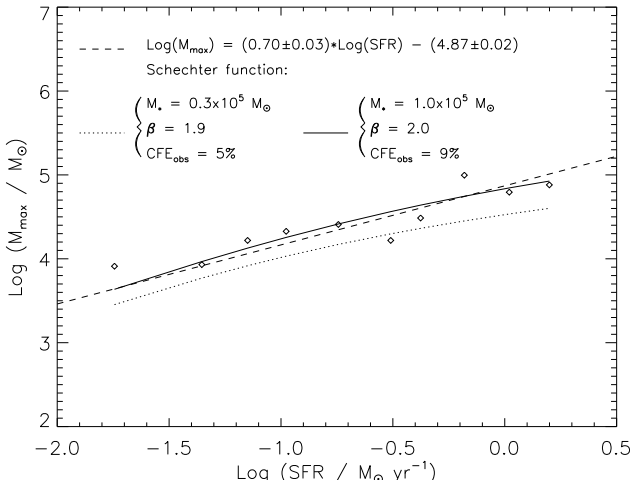

Figure 5.11: The mass of the most massive cluster versus the local SFR. The dashed line is the best-fitting power law through the data (diamonds). The dotted line is the predicted $M_{\rm max}$(SFR) relation for the best-fitting Schechter CIMF and assuming Eqs. 5.10 & 5.13. The solid line is the prediction for a Schechter function with a higher value for $M_\star$ and $\mathrm{CFE_{obs}}$. Note that the cluster masses (and thus the best-fitting $M_\star$) were multiplied by 1.38 to be consistent with the assumed Salpeter IMF used in the calculation of the SFR.

In Fig. 5.11 the mass of the most massive cluster in every bin is plotted against the SFR. We find that $M_{\rm max}$ is correlated with the SFR (and thus $M_{\rm tot}$) *within a single galaxy*, consistent with the result of Larsen (2002) and Weidner et al. (2004) for a large sample of galaxies. The best-fitting power law is of the form $M_{\rm max} \propto {M_{\rm tot}}^{0.70\pm0.03}$.

If we know the total mass in star clusters which are not embedded or blended with other sources, we can predict the mass of the most massive cluster observed if we assume a CIMF. If we assume a Schechter CIMF (Eq. 5.4) we can find the constant C from the equality

$$1 = \int_{M_{\rm max}}^{\infty} C M^{-\beta} e^{-M/M_\star} \mathrm{d}M, \tag{5.11}$$

which gives

$$C = \frac{1}{{M_{\rm max}}^{1-\beta} E_\beta\left(\frac{M_{\rm max}}{M_\star}\right)}. \tag{5.12}$$

This gives us for the total mass (see Eq. 5.5)

$$M_{\rm tot} = \frac{{M_{\rm min}}^{2-\beta} E_{\beta-1}\left(\frac{M_{\rm min}}{M_\star}\right)}{{M_{\rm max}}^{1-\beta} E_\beta\left(\frac{M_{\rm max}}{M_\star}\right)}. \tag{5.13}$$

By calculating $M_{\rm tot}$ for a large number of $M_{\rm max}$, this expression can be inverted numerically to find $M_{\rm max}\,(M_{\rm tot})$, and by using Eq. 5.10, $M_{\rm max}\,({\rm SFR})$. In Fig. 5.11 (dotted line) we show $M_{\rm max}\,({\rm SFR})$ expected for a Schechter function with $\beta = 1.9$ and $M_\star = 0.3{\times}10^5 M_\odot$, which is the best-fitting Schechter function from Sect. 5.4 (adjusted to a Salpeter stellar IMF to be consistent with the IMF used for the calculation of the SFRs).

We find that with such a Schechter function the predicted maximum cluster masses are slightly lower compared to the observed values. The curve also shows that for a Schechter function and a constant ${\rm CFE_{obs}}$, $M_{\rm max}\,({\rm SFR})$ flattens towards higher values of the SFR (and thus $M_{\rm tot}$), when more and more cluster masses are sampled close to the turnover mass. Towards lower values of the SFR the slope steepens and approaches the slope for a power law with an index of -1.9.

There are two effects that might explain why the predicted $M_{\rm max}\,({\rm SFR})$ curve is lower than the observed relation. First, it could be argued that, due to their higher brightness, the most massive clusters are less likely to be lost in the detection due to embeddedness or blends with less massive clusters. This would mean that the fraction 0.098 in Eq. 5.10, which is found by adding up *all* cluster masses, could actually be too low if we use Eq. 5.10 to predict the mass of the most massive clusters. Second, as was already mentioned in Sect. 5.4, there might be some selection effects present in our data which lead us to underestimate $M_\star$, and that we observe relatively too many clusters with masses above the best-fitting $M_\star$. We note that when we would use a higher $M_\star = 1 \times 10^5 M_\odot$ and an observed cluster mass fraction of ~ 0.18 (i.e. ${\rm CFE_{obs}} = 9\%$), the predicted $M_{\rm max}\,({\rm SFR})$ curve would follow the observed relation more closely. This is shown in Fig. 5.11 by the solid line. We therefore conclude that the clusters in M51 show a locally resolved $M_{\rm max}$ versus SFR relation consistent with a Schechter CIMF, although the current data does not allow us to draw firm conclusions on its exact functional form, nor on the mass dependence of the observed ${\rm CFE_{obs}}$.

5.6 Correction for selection effects: the true CFE

In the previous sections we have found that the fraction of mass in observed star clusters above our mass limit of $\log(M/M_\odot) = 3.2$ is ${\rm CFE_{obs}} = 5\%$. We also estimated the mass fraction above our mass limit ($f_{\rm lim} = 51\%$) and the fraction which is detected accounting for the embedded phase and confusion effects ($f_{\rm det} \approx 49\%$). Substituting all these in Eq. 5.2 we find that

$$ {\rm CFE_{true}} \cdot f_{\rm bound} = \frac{{\rm CFE_{obs}}}{f_{\rm lim} \cdot f_{\rm det}} \approx 20\%. \tag{5.14} $$

Due to the uncertainty in $f_{\rm det}$, which is actually an upper limit, this value of 20% should be considered a lower limit. For example, in an extreme case of missing half the clusters in our detection due to e.g. visual inspection and size criteria, $f_{\rm det}$ could be as low as 25% and ${\rm CFE_{true}} \cdot f_{\rm bound} \approx 40\%$. As already mentioned in Sect. 5.3.2, with

the current data we cannot separately determine the values of $\mathrm{CFE}_{\mathrm{true}}$ and f_{bound}. *If* we assume that star clusters cannot disperse within 10 Myr after formation (i.e. $f_{\mathrm{bound}} = 100\%$), Eq. 5.14 shows that $\sim 80\%$ *of the current star formation is taking place in a dispersed mode (*$\mathrm{CFE}_{\mathrm{true}} = 20\%$*). If*, on the other hand, we assume that all star formation is taking place in clusters ($\mathrm{CFE}_{\mathrm{true}} = 100\%$), we find that *80% of the clusters formed disperse into field stars within 10 Myr*.

In the following we will compare our observed mass fractions to the results of other studies. In such a comparison one has to bear in mind that for different techniques and different galaxies, one can be dealing with different detection limits and selectional biases due to different amounts of confusion, for which not all studies are necessarily corrected for.

Gieles & Bastian (2008) find that 2–4% of the star formation in the Small Magellanic Cloud (SMC) is observed in star clusters, leading to $\sim 97\%$ of either dispersed star formation or infant mortality in the SMC. This is similar to the CFE of 5% for the solar neighbourhood (Lamers & Gieles 2006b, 2008), but these values are considerably smaller than our results for M51 (after we have corrected our $\mathrm{CFE}_{\mathrm{obs}}$ for the mass limit and selection effects). Although this could suggest that the CFE in M51 is higher compared to the SMC or the solar neighbourhood, we have to bear in mind that our age interval of 0–10 Myr is shorter than the age interval used in the SMC and solar neighbourhood studies. The dispersion of star clusters will not stop abruptly at 10 Myr, which means that our derived CFE would likely be lower if we would average over a larger age interval.

In a recent study, Bastian (2008) finds that $\sim 8 \pm 3\%$ of the total star formation in a galaxy takes place in star clusters which survive the initial phase of gas expulsion. This is very similar to the 9.8% we find, after correcting $\mathrm{CFE}_{\mathrm{obs}} = 5\%$ for the mass below our mass limit. The approach of Bastian (2008), of modelling the observed relation between the total SFR of a galaxy and the luminosity of its brightest cluster, is very similar to our approach in Sect. 5.5.3 of predicting the relation between M_{max} and the local SFR (Fig. 5.11). We showed that with $\sim 10\%$ of the star formation taking place in clusters which are not dispersed immediately after gas expulsion, nor being embedded or blended, the predicted relation is lower than the observations. If we only use the masses of the most massive clusters we find better agreement with a fraction of $\sim 18\%$. This value is more uncertain, however, since it depends on the value of $M_{\star}$ used, and as we discussed in Sect. 5.4, this value is difficult to constrain accurately with our current data. Bastian (2008) shows that the fraction of "bound" star clusters is independent of the SFR of the parent galaxy. Similarly, we show (Fig. 5.6) that it is also independent of the *resolved* SFR *within* a single galaxy.

In another recent study, Parmentier & Fritze (2008) use the N-body grid of Baumgardt & Kroupa (2007) to model how the CFE, corrected for undetected clusters, depends on the star formation efficiency in cluster-forming cores.[2] Parmentier & Fritze (2008) show that a constant CFE, as observed by Bastian (2008) and in this

[2]We note that the CFE in our terminology corresponds to the ratio M_{cl}/M_{st} used in Parmentier & Fritze (2008), while these authors use the term cluster formation efficiency (ϵ_{cl}) for the ratio between the total mass in stars bound to the cluster and the total mass in core gas.

work, suggests a constant star formation efficiency.

Since Parmentier & Fritze (2008) make use of the output of dynamical *N*-body models, their results address only the initial dispersion (infant mortality) of clusters with time and not the formation of clusters. In other words, their results can only be used to constrain $f_{\rm bound}$ in Eq. 5.14 under the assumption of a certain $\mathrm{CFE}_{\rm true}$. Their model further assumes a weak tidal field, which also implies that the time interval after which infant mortality is over is $\gtrsim 50$ Myr. In a weak tidal field $f_{\rm bound}$ is still close to unity after 10 Myr. In this respect, the fact that we find that $\mathrm{CFE}_{\rm true} \cdot f_{\rm bound} \approx 20\%$ for clusters with ages < 10 Myr seems to suggest that this cannot be due to cluster dispersion on these short timescales, and thus that $\mathrm{CFE}_{\rm true} \sim 20\%$ instead. However, the tidal field for the majority of star clusters in M51 is much stronger than the weak tidal field used by Parmentier & Fritze (2008), the latter being typical of the Galactic halo at a distance of 35–40 kpc. For a stronger tidal field the time interval after which infant mortality is over can be of the order of 10 Myr or less, still leaving cluster dispersion within the first 10 Myr as a possibility (Parmentier 2009). Unfortunately, due to this difference in tidal field strength, it is not very meaningful to use the current models of Parmentier & Fritze (2008) to constrain the resolved *star* formation efficiency in M51, based on our observed *cluster* formation efficiency. New models that incorporate stronger tidal fields, however, could be exploited for this purpose. Currently, we can conclude that the results of Bastian (2008) and Parmentier & Fritze (2008) not only suggest that the local star formation efficiency does not vary among different galaxies, but combined with our observation that the CFE is practically constant, and under the assumption that the $\mathrm{CFE}_{\rm true}$ is constant, it is also suggested that the *resolved* star formation efficiency is constant throughout a single galaxy.

5.7 Summary and conclusions

We have made a quantitative comparison between the total resolved star formation rate (SFR) in M51 and the star formation taking place in visually observable star clusters (CFR). We matched published data of the resolved star formation law in M51 (i.e. SFR and gas surface densities, Kennicutt et al. 2007) with the star cluster data (masses, ages and extinctions) of Chapters 2 and 4. The fraction of star formation taking place in clusters younger than 10 Myr, which we defined as the cluster formation efficiency (CFE), was studied as a function of the total star formation rate, galactocentric radius and kinematic age with respect to the spiral arms. We also determined the cluster initial mass function (CIMF) of 437 clusters above our mass limit of $\log(M/M_{\odot}) = 3.2$. This allowed us to correct the observed mass in star clusters, and thus the CFE, for the missing star clusters below our detection limit. We further corrected the CFE for the selection bias against embedded clusters and clusters in crowded regions. The main conclusions of this chapter can be summarised as follows:

1. We find that a Schechter function with $M_{\star} = 2.2 \pm 1.6 \times 10^4 M_{\odot}$ and $\beta = 1.9 \pm 0.2$ is a good and simple approximation of the CIMF for clusters younger than 10 Myr and with $\log(M/M_{\odot}) > 3.2$ (Fig. 5.3). For a lower limit of $M_{\rm min} = 100 M_{\odot}$,

this means that 49% of the total mass formed in clusters will be below our mass limit. The best-fitting value of $M_\star$ is significantly lower compared to the results of other cluster studies, which could indicate a bias against clusters with a mass in the range $\log(M/M_\odot) = 4.0$–5.0 and age < 10 Myr. K-S tests show that a Schechter function with a higher $M_\star$ of $1 \times 10^5 M_\odot$ cannot be rejected based on the current data.

2. We find a tight correlation between the area normalised CFR and SFR of the form $\Sigma_{\rm CFR} = 0.046 \pm 0.006 \Sigma_{\rm SFR}^{0.94\pm0.06}$. This results in a CFE of optically visible star clusters above our mass limit of $\log(M/M_\odot) = 3.2$ of the form

$$\mathrm{CFE}_{\rm obs} = (0.046 \pm 0.006) \times \Sigma_{\rm SFR}^{-0.07\pm0.06}. \tag{5.15}$$

Thus we find that the $\mathrm{CFE}_{\rm obs}$ is nearly constant with SFR at a weighted mean of $5.0 \pm 0.2\%$ (Fig. 5.6).

3. The $\mathrm{CFE}_{\rm obs}$ of 5% does not depend strongly on galactocentric distance ($R_{\rm G}$, Fig. 5.8) or azimuthal distance from the spiral arms (Figs. 5.9 & 5.10). This suggests that the CFE is constant with environment throughout the disc of an entire spiral galaxy. Since the CFE is expected to be correlated to the *star* formation efficiency (SFE), this result suggests that the SFE is *constant throughout a single galaxy*. This is *inconsistent* with star formation laws which predict a higher SFE in denser environments, unless there is a mechanism which leads to fewer clusters being detected in regions with higher SFRs.

4. The mass of the locally most massive young cluster, $M_{\rm max}$, is correlated with the *local* SFR in M51 (Fig. 5.11). This is consistent with previous studies, where this correlation was found on the scale of entire galaxies. The best-fitting power law relation has an index of 0.70 ± 0.03, which is consistent with a Schechter function CIMF. Our best-fitting Schechter function, however, predicts slightly lower values for $M_{\rm max}$ than are observed. This suggests that the $\mathrm{CFE}_{\rm obs}$ is higher for the most massive clusters ($\mathrm{CFE}_{\rm obs} \approx 9\%$) and thus that the most massive clusters are less likely to be lost in the detection due to embeddedness or blends. If we combine this higher $\mathrm{CFE}_{\rm obs}$ with a higher $M_\star = 1 \times 10^5 M_\odot$ the predictions follow the observed relation more closely.

5. Correcting the CFE in observed clusters for our mass limit (i.e. a factor 2) and a reasonable amount of extinction and crowding (another factor of ~ 2), we find that $\approx 20\%$ of the current star formation in M51 is in the form of star clusters with ages < 10 Myr. This implies that either $\approx 80\%$ of the star clusters formed dispersed *immediately* following their embedded phase within the first 10 Myr, *or*, if the initial dispersion ("infant mortality") of star clusters takes place on a longer timescale, our results suggest that $\approx 80\%$ of the star formation takes place in a dispersed mode.

Acknowledgements We thank Genevieve Parmentier, Mark Gieles and Thomas Maschberger for helpful discussions. This research has made use of observations made with the NASA/ESA *Hubble Space Telescope*, obtained from the data archive at the Space Telescope Institute. STScI is operated by the association of Universities for Research in Astronomy, Inc., under the NASA contract NAS 5-26555.

Hoofdstuk 6

Nederlandse samenvatting

Sterrenhopen zijn de kraamkamers van sterren. Vrijwel alle sterren worden geboren in een sterrenhoop. Dit gebeurt wanneer een grote wolk van gas en stof zich samentrekt onder de invloed van de zwaartekracht. De meeste sterren die we zien bevinden zich echter niet meer in een sterrenhoop. Sterrenhopen hebben dus blijkbaar niet het eeuwige leven, maar ze vallen uit elkaar. Het merendeel doet dit al direct na de geboorte. Over deze vroege fase in het leven van sterren en sterrenhopen bestaan nog veel vragen. Hoeveel gas en stof wordt er bijvoorbeeld omgezet in nieuwe sterren? Hoe groot is de fractie sterrenhopen die direct uit elkaar valt? Hoe snel gebeurt dit? Hangt dit alles misschien af van bepaalde eigenschappen van de sterrenhoop, of van hun omgeving? En wat gebeurt er met de sterrenhopen die niet direct uit elkaar vallen? Dit soort vragen staan centraal in dit proefschrift over sterrenhopen in het melkwegstelsel met de naam "De Draaikolknevel". In dit hoofdstuk geef ik een korte introductie over sterrenhopen en de Draaikolknevel. Tevens geef ik een samenvatting van het onderzoek dat gepresenteerd wordt in dit proefschrift.

6.1 Sterrenhopen in de Melkweg

Een sterrenhoop is een groepje sterren die bijeengehouden wordt door hun onderlinge zwaartekracht. Een sterrenhoop kan uit tientallen tot enkele miljoenen sterren bestaan. Het bekendste voorbeeld van een sterrenhoop is te zien in Figuur 6.1 en wordt het "Zevengesternte" of ook wel de "Pleiaden" genoemd. Aan de blauw-witte kleur van de sterren valt af te lezen dat het hier gaat om relatief jonge en hete sterren. Net als bij de kleur van gloeiend metaal is een blauw-witte ster ("witheet") namelijk heter dan een gele ster, zoals de zon, die weer heter is dan een rode ster ("roodgloeiend"). Omdat een hete ster minder zuinig met zijn brandstof omspringt dan een koelere ster, leven blauwe sterren minder lang dan gele of rode sterren. Een

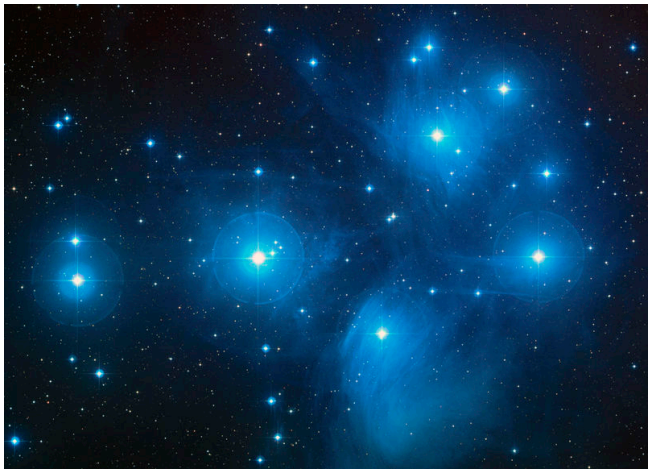

Figuur 6.1: Foto van "de Pleiaden", de bekendste open sterrenhoop in ons eigen melkwegstelsel. De zeven tot tien helderste sterren zijn op een heldere winteravond makkelijk met het blote oog te zien in het sterrenbeeld Stier. *Copyright:* NASA/ESA/AURA/Caltech.

sterrenhoop die gedomineerd wordt door blauwe sterren moet dus jonger zijn dan een sterrenhoop met alleen nog maar gele en rode sterren. De beste schattingen van de leeftijd van de Pleiaden geven aan dat de sterrenhoop ongeveer 100 miljoen jaar oud is.

Vanwege de open structuur worden sterrenhopen zoals de Pleiaden "open sterrenhopen" genoemd, in tegenstelling tot de meer symmetrische "bolvormige sterrenhopen". In Figuur 6.2 is het verschil tussen een open en bolvormige sterrenhoop goed te zien. Links zien we de open sterrenhoop NGC 346 en rechts de bolvormige sterrenhoop M80. Een bolvormige sterrenhoop kan wel uit honderd duizenden of een miljoen sterren bestaan en is over het algemeen dan ook zwaarder dan een open sterrenhoop, die vaak maar uit enkele duizenden sterren bestaat. De geel-oranje kleur van M80 komt overeen met een leeftijd van ongeveer 13 *miljard* jaar, bijna net zo oud als het heelal zelf! De blauwe, open sterrenhoop NGC 346 is daarentegen erg jong met een leeftijd van "slechts" 5 miljoen jaar. Dit is zó jong dat de overblijfselen van het gas en stof waaruit de sterrenhoop is ontstaan nog aanwezig zijn in de sterrenhoop. We zien de sterrenhoop nu in een fase waarin dit gas en stof wordt weggeblazen door de felle straling en de sterke winden van de jonge sterren. Figuur 6.3 (op pagina 130) is een ander voorbeeld van een jonge sterrenhoop waarin dit proces goed te zien is. Dit is een bewijs dat sterren in groepjes ontstaan uit wolken van gas en stof, en ook dat niet al dit gas en stof wordt gebruikt voor de vorming van sterren. Als het overgebleven gas en stof is verwijderd kunnen er geen nieuwe sterren meer ontstaan in de sterrenhoop. Dit betekent ook dat alle sterren in een sterrenhoop relatief snel moeten zijn ontstaan. Alle sterren in een sterrenhoop hebben dus ongeveer dezelfde leeftijd, met een verschil van maximaal een paar miljoen jaar.

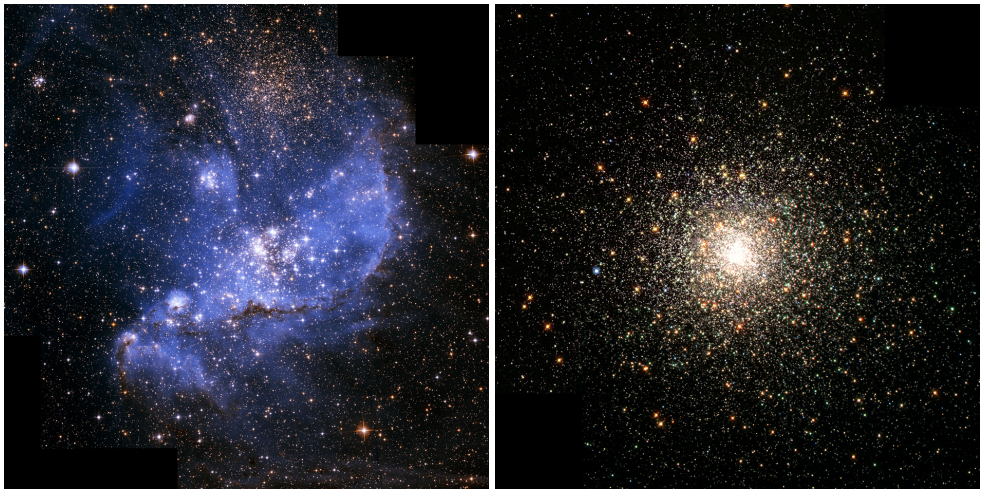

Figuur 6.2: Links: Foto van NGC 346, een jonge open sterrenhoop met een leeftijd van 5 miljoen jaar. *Copyright:* NASA, ESA en A. Nota (ESA/STScI). **Rechts:** Foto van M80 (NGC 6093), een oude bolvormige sterrenhoop met een leeftijd van ongeveer 13 miljard jaar. *Copyright:* Hubble Heritage Team (AURA/STScI/NASA).

Voor astronomische begrippen is dat een erg klein verschil.

Het feit dat sterren in groepjes ontstaan met allemaal dezelfde leeftijd is erg nuttig in de sterrenkunde. Groepjes van sterren zijn bijvoorbeeld makkelijker te zien dan sterren die alleen staan. Hier werd aan het begin van de 20e eeuw al dankbaar gebruik van gemaakt door de sterrenkundige Harlow Shapley, die de posities van bolvormige sterrenhopen gebruikte om een eerste redelijke schatting te maken van de afmeting van de Melkweg. De Melkweg is ons eigen *sterrenstelsel* (ook wel melkwegstelsel genoemd), oftewel een verzameling van ongeveer 200 miljard sterren in een afgeplatte schijf met spiraalarmen, met daarin ook gas en stof. Onze zon is slechts één van deze miljarden sterren. Sterrenhopen zijn veel kleiner dan sterrenstelsels en bevinden zich ook binnen een sterrenstelsel. Open sterrenhopen bevinden zich vooral in de schijf met sterren waar ook het meeste gas en stof zit, terwijl bolvormige sterrenhopen zich vooral buiten de schijf met sterren ophouden. Dit verschil heeft waarschijnlijk te maken met de ontstaansgeschiedenis van de Melkweg. De bolvormige sterrenhopen zijn vrijwel net zo oud als de Melkweg zelf, en zijn waarschijnlijk gevormd toen de Melkweg nog niet zo afgeplat was. De open sterrenhopen zijn veel jonger, en zijn dan ook later gevormd op de enige plek waar er genoeg gas en stof voorhanden was: in de schijf.

6.2 Sterrenhopen in andere melkwegstelsels

Sinds de lancering van de *Hubble Ruimtetelescoop* in 1990 beschikken we over de scherpste foto's die ooit gemaakt zijn van melkwegstelsels buiten onze eigen Melkweg. Vanuit de ruimte heeft de Hubble namelijk geen last van de verstorende effecten van de aardatmosfeer. Met behulp van zulke foto's zijn er inmiddels talloze sterrenhopen ontdekt in andere melkwegstelsels. Het blijkt dat vrijwel alle melkwegstelsels omgeven zijn door oude, bolvormige sterrenhopen. Bij sommige melkwegstelsels zijn sterrenhopen in de schijf ontdekt die net zo jong zijn als de open sterrenhopen in onze Melkweg, maar net zo zwaar als de bolvormige sterrenhopen. Dit lijkt te betekenen dat bolvormige sterrenhopen ook nu nog steeds gevormd worden, als de omgevingsfactoren maar gunstig zijn, of als je maar genoeg sterrenhopen vormt. Het staat in ieder geval vast dat in veel andere melkwegstelsels de verschillen tussen open en bolvormige sterrenhopen niet meer zo duidelijk zijn als in Figuur 6.2.

De scherpe foto's van de Hubble bieden ons nu de mogelijkheid om de ontwikkeling van melkwegstelsels te bestuderen aan de hand van de sterrenhopen. Het blijkt immers dat de meeste sterren geboren worden in sterrenhopen en dat de sterren in een sterrenhoop allemaal dezelfde leeftijd hebben. Als we dus de leeftijden van sterrenhopen in een melkwegstelsel bepalen weten we wanneer er daar veel nieuwe sterren zijn gevormd. Dit vertelt ons dan iets over de ontstaansgeschiedenis van dat melkwegstelsel.

In Figuur 6.2 zagen we al dat we de leeftijd van een sterrenhoop kunnen schatten aan de hand van de kleur. De laatste decennia zijn er veel sterrenkundigen actief geweest om dit gegeven heel precies uit te werken. Zij hebben nauwkeurige modellen gemaakt die voorspellen hoe de helderheid en de kleur van sterrenhopen verandert met hun leeftijd. Voor dit soort modellen is het erg belangrijk om te begrijpen hoe losse sterren zich ontwikkelen. Hier komen veel ingewikkelde theorieën aan te pas over het inwendige van sterren. Om dit soort theorieën te testen worden de modellen op hun beurt weer vergeleken met waarnemingen van sterrenhopen. Sterrenhopen zijn dus belangrijk om de evolutie van sterren beter te begrijpen. De modellen die hier uit voort komen zijn op hun beurt weer belangrijk om de leeftijden van sterrenhopen te bepalen. Deze leeftijden zijn ten slotte weer belangrijk om de ontwikkeling van melkwegstelsels te bestuderen.

Als we eenmaal weten wanneer er in een melkwegstelsel veel nieuwe sterrenhopen zijn gevormd, blijven er echter nog veel vragen onbeantwoord. We willen bijvoorbeeld ook weten hoeveel sterren er in totaal zijn gevormd. Vinden we alle nieuw gevormde sterren terug in sterrenhopen? Of slechts een klein percentage? Hoeveel sterrenhopen vallen er direct weer uit elkaar? Hoe snel gebeurt dit en waar hangt dit allemaal van af? Hoe lang blijven de overige sterrenhopen leven? Kunnen jonge sterrenhopen net zo oud worden als de bolvormige sterrenhopen in onze Melkweg? Pas als we dit allemaal begrijpen kunnen we aan de hand van de waargenomen sterrenhopen "terug gaan rekenen" naar de hoeveelheid sterren die op bepaalde momenten zijn gevormd. Pas dan kunnen we de sterrenhopen gebruiken om tot een gedetailleerd en volledig beeld te komen van de ontwikkeling en

ontstaansgeschiedenis van melkwegstelsels. In dit proefschrift probeer ik dit soort vragen te beantwoorden, waarbij ik me concentreer op de vorming en ontwikkeling van jonge sterrenhopen. Ik gebruik hiervoor waarnemingen gemaakt met de Hubble Ruimtetelescoop van het melkwegstelsel met de naam M51, oftewel de Draaikolknevel.

6.3 De Draaikolknevel M51

De Draaikolknevel is eigenlijk geen nevel maar een sterrenstelsel, net zoals onze eigen Melkweg. M51 is te vinden in het sterrenbeeld "de Jachthonden" en is al in een kleine telescoop zichtbaar. De naam "nevel" komt nog uit de tijd dat men niet goed wist wat al die wazige vlekjes aan de hemel (sterrenstelsels en echte nevels) nu precies waren. In een kleine telescoop lijken sterrenstelsels namelijk erg veel op nevels. Figuur 6.4 laat goed zien waar de naam "draaikolk" vandaan komt: M51 heeft twee grote spiraalarmen en is dus een spiraalstelsel. De spiraalarmen zijn waarschijnlijk versterkt door twee passages van een ander sterrenstelsel, met de naam NGC 5195, ongeveer 60 en 400–500 miljoen jaar geleden. Dit sterrenstelsel is rechts op de foto te zien als een gele vlek zonder duidelijke spiraalstructuur. De sterke getijdekrachten die vrijkomen als twee sterrenstelsels elkaar zo dicht naderen verklaren ook waarom er zoveel jonge sterrenhopen te vinden zijn in M51. Getijdekrachten veroorzaken namelijk dichtheidsverstoringen in de gas- en stofwolken, waardoor deze eerder instorten onder de invloed van de zwaartekracht en vervolgens sterrenhopen vormen. De foto laat ook goed zien dat de meeste sterrenhopen zich in de spiraalarmen bevinden, waar de dichtheid van het gas en stof het hoogst is.

M51 is, net als de Melkweg waarin wij met onze zon langzaam rondjes draaien, een grote platte schijf van sterren. Toevallig kijken we vanuit de Melkweg vrijwel recht van boven neer op de schijf van M51 (de exacte hoek is 20°). Dit zorgt ervoor dat alle structuren in de schijf goed zichtbaar zijn. Dit is één van de redenen waarom de Hubble opname van M51 zo geschikt is om de vorming en ontwikkeling van sterrenhopen te bestuderen: de jonge sterrenhopen in de schijf zijn goed te zien. Daarnaast is het beeld van Hubble zó scherp, dat we sterrenhopen kunnen onderscheiden van de helderste losse sterren. Omdat de opname een combinatie is van zes afzonderlijke foto's, is het beeldveld groot genoeg om de gehele schijf van M51 in beeld te brengen. Op deze manier kunnen we onderzoeken of sterrenhopen aan de rand van de schijf zich op een andere manier ontwikkelen als sterrenhopen dichtbij het centrum, waar de druk van de omgeving en de getijdekrachten veel hoger zijn. Een laatste voordeel van M51 boven andere melkwegstelsels is dat er van M51 erg veel andere foto's gemaakt zijn, in andere golflengtegebieden zoals radiostraling, het infrarood en het röntgen. Dit heeft ons bijvoorbeeld informatie opgeleverd over de hoeveelheid gas en stof in M51, en over de snelheid waarmee er nu nieuwe sterren worden gevormd. We gaan er van uit dat de omstandigheden in M51 ook in andere sterrenstelsels voorkomen. Door de sterrenhopen in M51 te bestuderen komen we dus meer te weten over hoe sterren ontstaan en over hoe sterrenstelsels zich ontwikkelen.

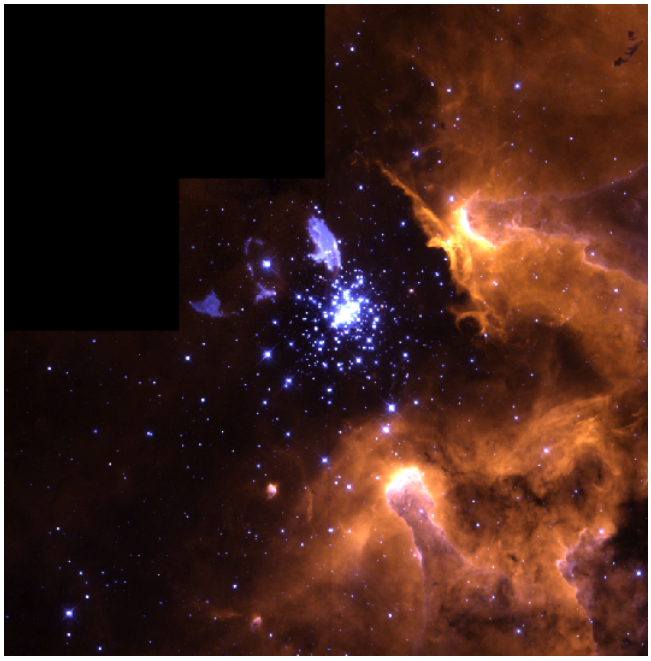

Figuur 6.3: Foto van NGC 3603, een open sterrenhoop met een leeftijd tussen de 1 en 4 miljoen jaar. De hete, blauw-witte sterren in het centrum blazen het overgebleven geel-bruine gas en stof uit de sterrenhoop. De kleine, blauwe nevels nabij het centrum zijn het resultaat van botsende winden van de zware ster die precies in het midden van de blauwe nevels staat. *Copyright:* W. Brandner (JPL/IPAC) en NASA.

6.4 Samenvatting van dit proefschrift

Dit proefschrift is een verzameling van artikelen over het onderzoek dat ik de laatste jaren heb verricht in samenwerking met mijn collega's. In deze artikelen bestuderen we de afmetingen, massa's, leeftijden en de posities van sterrenhopen in M51, met als doel deze eigenschappen te vergelijken met de eigenschappen van de gas- en stofwolken waaruit de sterrenhopen zijn ontstaan. Vervolgens leiden we af welk deel van de nieuwe stervorming er plaatsvindt in de sterrenhopen en we onderzoeken of dit afhangt van omgevingsfactoren.

6.4.1 Hoofdstuk 2: *ACS* opnamen van sterrenhopen in M51: identificatie en afmetingen

In hoofdstuk 2 beginnen we met de identificatie van de sterrenhopen. We gebruiken waarnemingen gemaakt met de *Advanced Camera for Surveys* (*ACS*) aan boord van de Hubble Ruimtetelescoop. Door de afmetingen te bepalen van alle stipjes op de

Figuur 6.4: Foto van M51 gemaakt met de Hubble Ruimtelescoop in januari 2005. De foto is een combinatie van zes afzonderlijke foto's, die op hun beurt weer gemaakt zijn door vier verschillende kleurfilters. In een computer zijn deze later samengevoegd tot één grote kleurenfoto met een resolutie van 105 megapixels. M51 is het grote spiraalstelsel. De gele vlek aan de rechterzijde is een begeleidend sterrenstelsel met de naam NGC 5195. De twee sterrenstelsels zijn met elkaar in interactie, met als gevolg de vorming van veel nieuwe sterrenhopen. De jonge sterrenhopen zijn te zien als kleine blauw-witte puntjes. De roze vlekjes zijn wolken met waterstofgas die opgewarmd worden door de straling van de sterrenhopen en daardoor in het rode deel van het spectrum oplichten. Het licht van M51 heeft er 27 miljoen jaar over gedaan om de aarde te bereiken. Met andere woorden, de afstand tot M51 is 27 miljoen lichtjaar. De foto zelf bestrijkt een afstand van 57×81 duizend lichtjaar. *Copyright:* Hubble Heritage Team (AURA/STScI/NASA).

originele opname van Figuur 6.4 vinden we 7698 sterrenhopen. Sterrenhopen zijn op deze opname namelijk net iets groter dan de helderste losse sterren en op deze manier kunnen ze dus van elkaar onderscheiden worden. We bestuderen de best bepaalde afmetingen van 1284 sterrenhopen in meer detail.

We vinden dat rode sterrenhopen iets groter zijn dan blauwe sterrenhopen en dat de rode sterrenhopen zich vooral tussen de spiraalarmen ophouden. De blauwe en dus jongere sterrenhopen bevinden zich vooral in de spiraalarmen. Dit lijkt te betekenen dat sterrenhopen na hun geboorte steeds groter worden. Door naar de verdeling van afmetingen te kijken en deze te vergelijken met de verdeling van de

afmetingen van gaswolken, vinden we dat ook bij de vorming van sterrenhopen de afmetingen moeten veranderen. Verschillende theorieën hierover komen echter niet overeen met onze waarnemingen en deze theorieën moeten dus aangepast worden.

We ontdekken ook een erg vreemd, wazig en groot object vlakbij het centrum van M51. Wat dit object precies is beschrijven we in hoofdstuk 3.

6.4.2 Hoofdstuk 3: een vreemd object in M51: is het een wazige cluster of een sterrenstelsel op de achtergrond?

In hoofdstuk 3 onderzoeken we in meer detail wat het vreemde object uit hoofdstuk 2 nu precies kan zijn. We voegen gegevens toe van waarnemingen in het nabije infrarood, zodat we meer informatie hebben over de kleur van het object.

Gebaseerd op het helderheidsverloop en de kleur van het object vinden we dat het erg onwaarschijnlijk is dat het object een sterrenstelsel is dat veel verder weg staat dan M51. Het object is namelijk te blauw vergeleken met andere sterrenstelsels en het helderheidsverloop van het centrum naar de rand van het object is minder steil.

Als we aannemen dat het object een sterrenhoop is kunnen we de massa en de leeftijd schatten. Hieruit blijkt dat als het object in de schijf van M51 zou zitten, het op het punt moet staan om uit elkaar te vallen. Hoewel dit zeker zou kunnen, denken we dat het waarschijnlijker is dat het hier om een sterrenhoop gaat die zich boven de schijf van M51 bevindt. Het is dan wel een grote, wazige sterrenhoop, maar het bevindt zich dan niet in een hele speciale fase van zijn leven.

6.4.3 Hoofdstuk 4: de ruimtelijke verdeling van stervorming in M51

In hoofdstuk 4 onderzoeken we in hoeverre sterrenhopen zelf weer in groepjes bij elkaar ontstaan. Het is namelijk waargenomen dat gaswolken, waaruit sterrenhopen ontstaan, een bepaalde *hiërarchie* vertonen: kleine "klonten" of verdichtingen in een gas- en stofwolk vormen samen een grotere wolk, die weer deel uit maakt van een nog grotere wolk, totdat de grootste wolk ongeveer de afmeting heeft van de doorsnede van een spiraalarm. Objecten die zulk gedrag vertonen staan ook wel bekend als *fractals* en bij een gaswolk wordt het veroorzaakt door de turbulente bewegingen in de wolk. De mate van hiërarchie vertelt iets over de fysische processen die zich in de wolken afspelen en dus over hoe sterren en sterrenhopen ontstaan. Het is nog de vraag of pas gevormde sterrenhopen dezelfde hiërarchie vertonen en of de mate van hiërarchie overal in het heelal hetzelfde is. In hoofdstuk 4 bepalen we de mate van hiërarchie voor de jonge sterrenhopen in M51.

Eerst voegen we nieuwe gegevens toe van waarnemingen van de ultra-violette (UV) straling van de sterrenhopen. Dit helpt ons om nauwkeurig de leeftijden en massa's van 1580 sterrenhopen te bepalen. Hiervoor gebruiken we de modellen die ik heb beschreven in paragraaf 6.2. Vervolgens gebruiken we een wiskundige techniek om de mate van hiërarchie te bepalen, waarbij de posities van alle sterrenhopen gebruiken.

We vinden dat de mate van hiërarchie van de jongste sterrenhopen in M51 overeenkomt met wat is waargenomen voor gaswolken en jonge sterrenhopen in andere melkwegstelsels. Dit suggereert dat de fysische processen die zich afspelen tijdens het vormen van sterren overal in het heelal hetzelfde zijn.

Verder vinden we dat de jongste sterrenhopen zich vooral in het midden van de spiraalarmen bevinden, terwijl oudere sterrenhopen meer gelijkmatig over de schijf verdeeld zijn. Omdat sterrenhopen niet stilzitten, maar zich langzaam door de spiraalarmen bewegen, betekent dit dat de sterrenhopen al ongeveer 5 tot 20 miljoen jaar eerder gevormd zijn, voordat de oorspronkelijke gaswolk het midden van de spiraalarm zou bereiken.

Tot slot kijken we in hoofdstuk 4 hoe de posities van de sterrenhopen jonger dan 10 miljoen jaar oud overeenkomen met de locaties waar op dit moment nieuwe sterren worden gevormd. Deze overeenkomst is erg goed. Dit bevestigt nogmaals dat de meeste sterren inderdaad ontstaan in sterrenhopen. Hoeveel nieuw gevormde sterren we precies kunnen waarnemen in de vorm van jonge sterrenhopen onderzoeken we in hoofdstuk 5.

6.4.4 Hoofdstuk 5: hoe efficiënt is de vorming van sterrenhopen in M51?

In hoofdstuk 5 onderzoeken we hoe efficiënt de vorming van sterrenhopen is. Als we weten welk percentage van de nieuw gevormde sterren te zien is in een sterrenhoop, kunnen we schatten hoeveel sterrenhopen direct na hun geboorte uit elkaar gevallen zijn en hoe snel dit is gebeurd. Dit is belangrijk voor ons begrip over stervorming en als we de sterrenhopen willen gebruiken om de ontwikkeling van melkwegstelsels te bestuderen.

In hoofdstuk 5 tellen we de massa's bij elkaar op van alle sterrenhopen jonger dan 10 miljoen jaar oud. Ook doen we een schatting van de hoeveelheid massa in sterrenhopen die te zwak zijn om nog met Hubble te kunnen zien. Zo kunnen we als het ware bepalen hoeveel sterren er per jaar in een sterrenhoop gevormd worden. Dit vergelijken we met informatie over de hoeveelheid sterren die ieder jaar in totaal in M51 ontstaan.

Op deze manier vinden we dat slechts 20% van de stervorming plaatsvindt in sterrenhopen. De overige 80% van de sterren kan wel gevormd zijn in sterrenhopen, maar deze zijn waarschijnlijk binnen 10 miljoen jaar alweer uit elkaar gevallen, vlak nadat de eerste sterren het overgebleven gas uit de sterrenhopen hebben geblazen. We vinden ook dat deze fractie niet sterk afhangt van de omgevingsfactoren in M51. Hier kunnen we nu rekening mee houden als we sterrenhopen gebruiken om te bestuderen hoe sterren en melkwegstelsels onstaan.

Dankwoord

Zo, toen zat het er alweer op. Het boekje is klaar. Het doet mij een groot genoegen om iedereen hier te bedanken die dat mede mogelijk heeft gemaakt.

Allereerst wil ik mijn promotor Henny bedanken. Ook al zagen we elkaar misschien niet al te vaak, je hebt me wel altijd alle vrijheid en mogelijkheden geboden om me tot zelfstandig en kritisch wetenschapper te ontwikkelen.

Søren, I thank you for being a good co-promotor. Your thorough comments never missed a weak spot and helped me to always stay with "both feet on the ground". Anticipating your comments on every new sentence I wrote reduced my typing speed with at least 50%, but that's okay.

De leden van de beoordelingscommissie, Christoph Keller, Norbert Langer, Bram Achterberg, Richard de Grijs en Alex de Koter, wil ik bedanken voor het grondig lezen van het manuscript.

I want to thank Mark and Nate for always inspiring me. Your guidance, already during my master's research, has been important during the first steps of this thesis. Now you guys can go back to work to get another paper out next week.

Alle collega's van het Sterrekundig Instituut en de stercluster groep worden bedankt voor de gezellige werksfeer. Hierbij wil ik ook zeker enkele ex-collega's (Arend-Jan, Cees, Axel, Evert, Marc, Alfred), (ex-)studenten (Marcel, Ernst, Gregal, Steven, Nick) en lotgenoten bij het SRON (Jelle, Laurens, Peter) niet vergeten.

Ed en Sake worden bedankt voor alle technische steun en hun geduld. Ik had er alle vertrouwen in als ik keer op keer weer mijn nieuwe laptops binnen twee weken op zwart wist te krijgen.

Thijs Krijger wordt bedankt voor het planten van een "IDL zaadje" in een grijs verleden. Het is inmiddels een plantje, want nu weten collega's mij te vinden voor hun IDL vragen.

And no, I am not too gierig to thank Rob Izzard for all his knowledge, fun, laughs, footy games and good wines!

My office mate Peter is thanked for all his wisdom, skills and supply of GALEV models on-demand. I have yet to find another person who is always in such a good mood and willing to help out no matter what.

Het instituut zou een stuk minder levendig zijn zonder (ex-office mate) Martijn. Ik geniet nog dagelijks van je complete Depeche Mode collectie van kasper, en ook de geluiden die je zelf wist te produceren waren af en toe erg nuttig om de aandacht

erbij te houden.

Ik wil Rob Detmers bedanken voor de gezelligheid in Nederland, maar ook daarbuiten, tijdens onze zware trips in Zwitserland en Schotland (al is "zwaar" natuurlijk een relatief begrip).

Ana, thanks for the personal discussions and for being a nice person. You bring an extra "human touch" to the group, which is greatly appreciated.

Daniel, Peter, Sietse, Arjan en Edo bedank ik voor alle vriendschap in Twente en de gezelligheid op en via de sterrenwacht in Lattrop. Het blijft toch altijd lekker om tot rust te komen daar. Ook al is het waarnemen, fotograferen en storm chasen om praktische redenen soms wat minder, de gezamenlijke passie blijft en is toch wel erg bijzonder.

Theodora, bedankt voor alles wat we samen hebben mogen beleven. Ik hoop dat we nog veel meer samen zullen gaan beleven.

Ik wil Wendy en Mark bedanken voor al het begrip en de "mentale coaching". Wendy, ik had me geen betere zus kunnen wensen. Als laatste bedank ik mijn ouders voor de jarenlange steun en interesse, ook al begrepen jullie niet altijd waar ik mee bezig was. Het heeft me mijn hele leven aan niets ontbroken dankzij jullie, met als resultaat dat ik heb kunnen bereiken wat ik het liefste wilde.

Curriculum Vitae

I was born on October 4th 1980 in Rijssen, The Netherlands. I grew up in Almelo, where I started my education at the primary school *De Hobbitstee*. In 1993 I went to the secondary school *R.-K. Scholengemeenschap St.-Canisius*, from which I received my *VWO* diploma in 1999.

I started the study *Physics and Astronomy* at Utrecht University in 1999. My master thesis was on *The radii of star clusters in M51 and M101* in the group of prof. dr. H.J.G.L.M. (Henny) Lamers at the Astronomical Institute Utrecht and co-supervised by dr. M. (Mark) Gieles. For this research I derived the radii of star clusters using *Hubble Space Telescope WFPC2* data, and I developed a Monte-Carlo (toy) model to study how different processes during star cluster formation change the mass and radius distribution. During this work I stayed one week at the Observatoire de Marseille in France. On January 24th 2005 I received my *Doctoraal diploma Natuur- en Sterrenkunde* (Master's degree in physics and Astronomy) "cum laude".

In June 2005 I started my PhD research in the same group of Henny Lamers, and later in the group of dr. S.S. (Søren) Larsen. This book is the result of the work performed in the past four years. During this research I presented my work at conferences, schools and workshops in Tenerife, Concepción, Bern, Seeon, Garching and Sheffield. I will defend my thesis on June 16th 2009.

List of publications

Published in refereed journals

1. Scheepmaker, Lamers, Anders & Larsen 2009, A&A, 494, 81, *The spatial distribution of star and cluster formation in M51*
2. Haas, Gieles, Scheepmaker, Larsen & Lamers 2008, A&A, 487, 937, *ACS imaging of star clusters in M51: II. The luminosity function and mass function across the disk*
3. Scheepmaker, Lamers, Larsen & Anders 2008, A&A, 477, 117, *A peculiar object in M51: fuzzy star cluster or a background galaxy?*
4. Bastian, Ercolano, Gieles, Rosolowsky, Scheepmaker, Gutermuth & Efremov 2007, MNRAS, 379, 1302, *Hierarchical star formation in M33: fundamental properties of the star-forming regions*
5. Scheepmaker, Haas, Gieles, Bastian, Larsen & Lamers 2007, A&A, 469, 925, *ACS imaging of star clusters in M51: I. Identification and radius distribution*
6. Gieles, Larsen, Scheepmaker, Bastian, Haas & Lamers 2006, A&A, 446, L9, *Observational evidence for a truncation of the star cluster initial mass function at the high mass end*
7. Bastian, Gieles, Lamers, Scheepmaker & de Grijs 2006, A&A, 431, 905, *The Star Clusters Population of M51: II. Age distribution and relation between structural parameters*

Submitted to refereed journals

1. Scheepmaker, Lamers, Larsen & Anders 2009, A&A, *The star cluster formation efficiency in M51*

Published in conference proceedings

1. Scheepmaker, Gieles, Haas, Bastian & Lamers 2008, ASPC, 388, 417, Workshop held in honour of H.J.G.L.M. Lamers, ed. A. de Koter, L. Smith & R. Waters, *Thousands of Star Clusters in M51 with HST/ACS*

2. Haas, Gieles, Scheepmaker, Larsen, Lamers & Bastian 2008, ASPC, 388, 405, Workshop held in honour of H.J.G.L.M. Lamers, ed. A. de Koter, L. Smith & R. Waters, `astro-ph/060918`, *Variation of the cluster luminosity function across the disk of M51*

3. Scheepmaker, Gieles, Haas, Bastian, Larsen & Lamers 2006, Globular clusters - Guides to Galaxies, ed. T. Richtler & S.S. Larsen, `astro-ph/0605022`, *The radii of thousands of star clusters in M51 with HST/ACS*

4. Gieles, Larsen, Haas, Scheepmaker & Bastian 2006, Globular clusters - Guides to Galaxies, ed. T. Richtler & S.S. Larsen, `astro-ph/0604578`, *The maximum mass of star clusters*

Bibliography

Anders, P., Bissantz, N., Fritze-v. Alvensleben, U., & de Grijs, R. 2004, MNRAS, 347, 196 (cited on pages 59, 65, 74, and 78)

Anders, P. & Fritze-v. Alvensleven, U. 2003, A&A, 401, 1063 (cited on pages 5, 59, and 78)

Anders, P., Gieles, M., & de Grijs, R. 2006, A&A, 451, 375 (cited on page 24)

Anderson, S., Hodge, P., & Kennicutt, Jr., R. C. 1983, ApJ, 265, 132 (cited on page 93)

Ashman, K. M. & Zepf, S. E. 2001, AJ, 122, 1888 (cited on pages 18, 19, 40, 41, and 50)

Barden, M., Rix, H.-W., Somerville, R. S., et al. 2005, ApJ, 635, 959 (cited on page 64)

Barmby, P., Kuntz, K. D., Huchra, J. P., & Brodie, J. P. 2006, AJ, 132, 883 (cited on page 46)

Bash, F. N. 1979, ApJ, 233, 524 (cited on page 93)

Bastian, N. 2008, MNRAS, 390, 759 (cited on pages 109, 121, and 122)

Bastian, N., Ercolano, B., Gieles, M., et al. 2007, MNRAS, 379, 1302 (cited on page 73)

Bastian, N., Gieles, M., Efremov, Y. N., & Lamers, H. J. G. L. M. 2005a, A&A, 443, 79 (cited on pages 18 and 78)

Bastian, N., Gieles, M., Lamers, H. J. G. L. M., Scheepmaker, R. A., & de Grijs, R. 2005b, A&A, 431, 905 (B05) (cited on pages 10, 18, 57, 58, and 88)

Bastian, N. & Goodwin, S. P. 2006, MNRAS, 369, L9 (cited on pages 72 and 104)

Bate, M. R., Clarke, C. J., & McCaughrean, M. J. 1998, MNRAS, 297, 1163 (cited on page 95)

Baumgardt, H. & Kroupa, P. 2007, MNRAS, 380, 1589 (cited on page 121)

Baumgardt, H. & Makino, J. 2003, MNRAS, 340, 227 (cited on pages 5 and 67)

Beech, M. 1992, Ap&SS, 192, 103 (cited on page 95)

Bertelli, G., Bressan, A., Chiosi, C., Fagotto, F., & Nasi, E. 1994, A&AS, 106, 275 (cited on page 78)

Bertin, E. & Arnouts, S. 1996, A&AS, 117, 393 (cited on pages 20, 21, and 73)

Bicker, J., Fritze-v. Alvensleben, U., Möller, C. S., & Fricke, K. J. 2004, A&A, 413, 37 (cited on page 63)

Bigiel, F., Leroy, A., Walter, F., et al. 2008, ArXiv e-prints (cited on pages 104, 114, and 117)

Bik, A., Lamers, H. J. G. L. M., Bastian, N., Panagia, N., & Romaniello, M. 2003, A&A, 397, 473 (cited on pages 9, 18, 40, 82, and 110)

Binney, J. & Tremaine, S. 1987, Galactic dynamics, Princeton series in astrophysics (Princeton University Press) (cited on page 48)

Boeshaar, G. O. & Hodge, P. W. 1977, ApJ, 213, 361 (cited on page 91)

Boily, C. M. & Kroupa, P. 2003, MNRAS, 338, 665 (cited on page 43)

Bonnor, W. B. 1956, MNRAS, 116, 351 (cited on pages 47 and 50)

Boutloukos, S. G. & Lamers, H. J. G. L. M. 2003, MNRAS, 338, 717 (cited on pages 5 and 67)

Brand, J. & Wouterloot, J. G. A. 1995, A&A, 303, 851 (cited on pages 18 and 40)

Bruzual, G. & Charlot, S. 2003, MNRAS, 344, 1000 (cited on page 5)

Calzetti, D., Kennicutt, Jr., R. C., Bianchi, L., et al. 2005, ApJ, 633, 871 (cited on pages 10, 72, 85, and 106)

Cardelli, J. A., Clayton, G. C., & Mathis, J. S. 1989, ApJ, 345, 245 (cited on pages 59, 60, 63, and 78)

Charbonnel, C., Meynet, G., Maeder, A., Schaller, G., & Schaerer, D. 1993, A&AS, 101, 415 (cited on page 78)

Chita, S. M., Langer, N., van Marle, A. J., García-Segura, G., & Heger, A. 2008, A&A, 488, L37 (cited on page 7)

Condon, J. J. 1992, ARA&A, 30, 575 (cited on page 72)

Contopoulos, G. & Grosbøl, P. 1986, A&A, 155, 11 (cited on page 90)

Contopoulos, G. & Grosbøl, P. 1988, A&A, 197, 83 (cited on page 90)

de Grijs, R. & Anders, P. 2006, MNRAS, 366, 295 (cited on page 78)

de Grijs, R., Anders, P., Bastian, N., et al. 2003a, MNRAS, 343, 1285 (cited on page 9)

de Grijs, R., Anders, P., Lamers, H. J. G. L. M., et al. 2005, MNRAS, 359, 874 (cited on page 78)

de Grijs, R., Bastian, N., & Lamers, H. J. G. L. M. 2003b, MNRAS, 340, 197 (cited on pages 18 and 40)

de Grijs, R., Fritze-v. Alvensleben, U., Anders, P., et al. 2003c, MNRAS, 342, 259 (cited on page 110)

de Grijs, R., Lee, J. T., Mora Herrera, M. C., Fritze-v. Alvensleben, U., & Anders, P. 2003, New Astronomy, 8, 155 (cited on pages 72 and 104)

de Vaucouleurs, G. 1948, Annales d'Astrophysique, 11, 247 (cited on pages 61 and 63)

Diaz, A. I., Terlevich, E., Vilchez, J. M., Pagel, B. E. J., & Edmunds, M. G. 1991, MNRAS, 253, 245 (cited on pages 56 and 78)

Dolphin, A. E. 2000, PASP, 112, 1397 (cited on page 76)

Dowell, J. D., Buckalew, B. A., & Tan, J. C. 2006, ArXiv Astrophysics e-prints (cited on page 18)

Ebert, R. 1955, Zeitschrift fur Astrophysik, 37, 217 (cited on pages 47 and 50)

Efremov, Y. N. 1995, AJ, 110, 2757 (cited on page 88)

Efremov, Y. N. & Elmegreen, B. G. 1998, MNRAS, 299, 588 (cited on pages 73 and 88)

Eisenhardt, P. R., De Propris, R., Gonzalez, A. H., et al. 2007, ApJS, 169, 225 (cited on pages 62 and 63)

Elmegreen, B. G. 1989, ApJ, 338, 178 (cited on pages 18 and 50)

Elmegreen, B. G. 2008, ApJ, 672, 1006 (cited on page 113)

Elmegreen, B. G. & Efremov, Y. N. 1996, ApJ, 466, 802 (cited on page 88)

Elmegreen, B. G. & Efremov, Y. N. 1997, ApJ, 480, 235 (cited on pages 2, 8, 110, and 113)

Elmegreen, B. G. & Elmegreen, D. M. 2001, AJ, 121, 1507 (cited on pages 19, 40, 88, and 95)

Elmegreen, B. G., Elmegreen, D. M., Chandar, R., Whitmore, B., & Regan, M. 2006, ApJ, 644, 879 (cited on page 95)

Elmegreen, B. G., Elmegreen, D. M., & Seiden, P. E. 1989, ApJ, 343, 602 (cited on page 90)

Elmegreen, B. G. & Falgarone, E. 1996, ApJ, 471, 816 (cited on pages 2, 9, 18, 19, 40, and 95)

Elmegreen, D. M., Kaufman, M., Elmegreen, B. G., et al. 2001, AJ, 121, 182 (cited on page 18)

Elmegreen, D. M. & Salzer, J. J. 1999, AJ, 117, 764 (cited on page 18)

Elson, R. A. W., Fall, S. M., & Freeman, K. C. 1987, ApJ, 323, 54 (cited on pages 25, 58, 61, 74, and 147)

Fall, S. M., Chandar, R., & Whitmore, B. C. 2005, ApJ, 631, L133 (cited on pages 72 and 104)

Feldmeier, J. J., Ciardullo, R., & Jacoby, G. H. 1997, ApJ, 479, 231 (cited on pages 9, 20, 62, 78, and 107)

Fellhauer, M. & Kroupa, P. 2005, ApJ, 630, 879 (cited on page 18)

Freeman, K. C. 1970, ApJ, 160, 811 (cited on page 64)

Fruchter, A. S. & Hook, R. N. 2002, PASP, 114, 144 (cited on pages 20 and 22)

Fukugita, M., Shimasaku, K., & Ichikawa, T. 1995, PASP, 107, 945 (cited on page 63)

Fukui, Y., Mizuno, N., Yamaguchi, R., Mizuno, A., & Onishi, T. 2001, PASJ, 53, L41 (cited on pages 18 and 40)

García-Burillo, S., Combes, F., & Gerin, M. 1993, A&A, 274, 148 (cited on pages 45, 67, 90, and 116)

Geyer, M. P. & Burkert, A. 2001, MNRAS, 323, 988 (cited on page 41)

Gieles, M., Athanassoula, E., & Portegies Zwart, S. F. 2007, MNRAS, 376, 809 (cited on pages 5, 43, and 67)

Gieles, M. & Bastian, N. 2008, A&A, 482, 165 (cited on pages 82, 118, and 121)

Gieles, M., Bastian, N., Lamers, H. J. G. L. M., & Mout, J. N. 2005, A&A, 441, 949 (cited on pages 56, 67, and 78)

Gieles, M., Larsen, S. S., Bastian, N., & Stein, I. T. 2006a, A&A, 450, 129 (cited on page 110)

Gieles, M., Larsen, S. S., Scheepmaker, R. A., et al. 2006b, A&A, 446, L9 (cited on pages 18, 30, 110, 111, and 112)

Gieles, M., Portegies Zwart, S. F., Baumgardt, H., et al. 2006c, MNRAS, 371, 793 (cited on pages 5, 41, 56, and 67)

Girardi, L., Bertelli, G., Bressan, A., et al. 2002, A&A, 391, 195 (cited on page 2)

Girardi, L., Bressan, A., Bertelli, G., & Chiosi, C. 2000, A&AS, 141, 371 (cited on page 78)

Gomez, M., Hartmann, L., Kenyon, S. J., & Hewett, R. 1993, AJ, 105, 1927 (cited on pages 94 and 95)

Goodwin, S. P. 1997, MNRAS, 284, 785 (cited on pages 7 and 43)

Goodwin, S. P. & Bastian, N. 2006, MNRAS, 373, 752 (cited on pages 4, 8, 41, 72, and 104)

Haas, M. R., Gieles, M., Scheepmaker, R. A., Larsen, S. S., & Lamers, H. J. G. L. M. 2008, ArXiv e-prints, 806 (cited on pages 30 and 32)

Haşegan, M., Jordán, A., Côté, P., et al. 2005, ApJ, 627, 203 (cited on page 18)

Harris, W. E. 1996, AJ, 112, 1487 (cited on pages 25, 46, and 62)

Harris, W. E. & Pudritz, R. E. 1994, ApJ, 429, 177 (cited on pages 18, 40, 47, and 50)

Helou, G., Soifer, B. T., & Rowan-Robinson, M. 1985, ApJ, 298, L7 (cited on page 96)

Hesser, J. E., Harris, H. C., Van den Bergh, S., & Harris, G. L. 1984, ApJ, 276, 491 (cited on page 47)

Hill, J. K., Waller, W. H., Cornett, R. H., et al. 1997, ApJ, 477, 673 (cited on pages 56 and 78)

Hills, J. G. 1980, ApJ, 225, 986 (cited on pages 41 and 104)

Hodge, P. W. 1962, PASP, 74, 248 (cited on page 47)

Holtzman, J. A., Faber, S. M., Shaya, E. J., et al. 1992, AJ, 103, 691 (cited on page 72)

Holwerda, B. W. 2005, Source Extractor for Dummies v5 (cited on page 21)

Hunter, D. A., Elmegreen, B. C., Dupuy, T. J., & Mortonson, M. 2003, AJ, 126, 1836 (cited on pages 18, 40, and 82)

Hwang, N. & Lee, M. G. 2006, ApJ, 638, L79 (cited on pages 33 and 35)

Hwang, N. & Lee, M. G. 2008, AJ, 135, 1567 (cited on pages 85 and 90)

Jarrett, T. H., Chester, T., Cutri, R., Schneider, S. E., & Huchra, J. P. 2003, AJ, 125, 525 (cited on pages 84 and 88)

Jensen, J. B., Tonry, J. L., & Luppino, G. A. 1999, ApJ, 510, 71 (cited on page 63)

Jog, C. J. & Solomon, P. M. 1992, ApJ, 387, 152 (cited on page 8)

Jordán, A., Côté, P., Blakeslee, J. P., et al. 2005, ApJ, 634, 1002 (cited on pages 18, 46, and 62)

Kennicutt, Jr., R. C. 1998a, ARA&A, 36, 189 (cited on pages 85 and 107)

Kennicutt, Jr., R. C. 1998b, ApJ, 498, 541 (cited on pages 72 and 104)

Kennicutt, Jr., R. C., Calzetti, D., Walter, F., et al. 2007, ApJ, 671, 333 (cited on pages 72, 73, 85, 87, 89, 96, 98, 104, 107, 108, 114, 117, 118, and 122)

King, I. 1962, AJ, 67, 471 (cited on pages 25 and 61)

Kissler-Patig, M., Jordán, A., & Bastian, N. 2006, A&A, 448, 1031 (cited on page 18)

Koekemoer, A. M., Fruchter, A. S., Hook, R. N., & Hack, W. 2002, in HST Calibration Workshop, ed. S. Arribas, A. Koekemoer, & B. Whitmore, STScI, 337–340 (cited on page 20)

Kroupa, P. 2001, MNRAS, 322, 231 (cited on page 78)

Kroupa, P. 2002, MNRAS, 330, 707 (cited on page 104)

Lada, C. J. & Lada, E. A. 2003, ARA&A, 41, 57 (cited on pages 6, 8, 45, 72, 104, and 110)

Lamers, H. J. G. L. M. & Cassinelli, J. P. 1999, Introduction to Stellar Winds (Cambridge University Press) (cited on page 97)

Lamers, H. J. G. L. M. & Gieles, M. 2006a, A&A, 455, L17 (cited on page 5)

Lamers, H. J. G. L. M. & Gieles, M. 2006b, A&A, 455, L17 (cited on page 121)

Lamers, H. J. G. L. M. & Gieles, M. 2008, in Astronomical Society of the Pacific Conference Series, Vol. 388, Astronomical Society of the Pacific Conference Series, ed. A. de Koter, L. J. Smith, & L. B. F. M. Lamers, 367–+ (cited on page 121)

Lamers, H. J. G. L. M., Gieles, M., Bastian, N., et al. 2005, A&A, 441, 117 (cited on pages 5 and 67)

Larsen, S. S. 1999, A&A Suppl. Ser., 139, 393 (cited on pages 23, 25, 26, 57, 61, and 74)

Larsen, S. S. 2002, AJ, 124, 1393 (cited on pages 118 and 119)

Larsen, S. S. 2004, A&A, 416, 537 (cited on pages 9, 18, 22, 23, 25, 46, 51, 57, 61, 72, and 74)

Larsen, S. S. 2008, ArXiv e-prints (cited on page 118)

Larsen, S. S. & Richtler, T. 1999, A&A, 345, 59 (cited on page 72)

Larsen, S. S. & Richtler, T. 2000, A&A, 354, 836 (cited on pages 33, 69, and 72)

Larson, R. B. 1981, MNRAS, 194, 809 (cited on pages 2, 8, 18, and 50)

Larson, R. B. 1995, MNRAS, 272, 213 (cited on pages 94 and 95)

Lee, M. G., Chandar, R., & Whitmore, B. C. 2005, AJ, 130, 2128 (cited on pages 18, 19, 45, and 46)

Leitherer, C., Schaerer, D., Goldader, J. D., et al. 1999, ApJS, 123, 3 (cited on page 5)

Leroy, A. K., Walter, F., Brinks, E., et al. 2008, ArXiv e-prints (cited on pages 104, 105, and 114)

Mac Low, M.-M. & Klessen, R. S. 2004, Reviews of Modern Physics, 76, 125 (cited on page 2)

Mackey, A. D. & Gilmore, G. F. 2003, MNRAS, 338, 85 (cited on pages 18 and 51)

Maíz Apellániz, J. 2009, ArXiv e-prints (cited on page 14)

Mandelbrot, B. B. 1983, The fractal geometry of nature (Freeman, San Francisco) (cited on pages 19, 40, and 95)

Maraston, C. 2005, MNRAS, 362, 799 (cited on page 5)

Marsh, K. A. & Helou, G. 1995, ApJ, 445, 599 (cited on page 96)

Maschberger, T. & Kroupa, P. 2007, MNRAS, 379, 34 (cited on page 118)

Mateo, M. 1987, ApJ, 323, L41 (cited on page 47)

McKee, C. F. & Ostriker, E. C. 2007, ARA&A, 45, 565 (cited on page 2)

McQuinn, K. B. W., Skillman, E. D., Cannon, J. M., et al. 2009, ApJ, 695, 561 (cited on page 14)

Meurer, G. R., Heckman, T. M., Leitherer, C., et al. 1995, AJ, 110, 2665 (cited on pages 72 and 104)

Mihos, J. C. & Hernquist, L. 1994, ApJ, 437, 611 (cited on pages 72 and 104)

Moffat, A. F. J. 1969, A&A, 3, 455 (cited on page 23)

Murgia, M., Helfer, T. T., Ekers, R., et al. 2005, A&A, 437, 389 (cited on page 96)

Murphy, E. J., Helou, G., Braun, R., et al. 2006, ApJ, 651, L111 (cited on pages 72 and 96)

Murphy, E. J., Helou, G., Kenney, J. D. P., Armus, L., & Braun, R. 2008, ApJ, 678, 828 (cited on pages 72 and 96)

Mutchler, M., Beckwith, S. V. W., Bond, H. E., et al. 2005, BAAS, 37 (cited on pages 10, 20, 57, 73, and 96)

Niklas, S. 1997, A&A, 322, 29 (cited on pages 72 and 96)

Niklas, S. & Beck, R. 1997, A&A, 320, 54 (cited on pages 72 and 96)

Parmentier, G. 2009, ArXiv e-prints (cited on pages 8 and 122)

Parmentier, G. & Fritze, U. 2008, ArXiv e-prints (cited on pages 4, 8, 104, 109, 121, and 122)

Patrikeev, I., Fletcher, A., Stepanov, R., et al. 2006, A&A, 458, 441 (cited on page 96)

Pavlovsky, C., Koekemoer, A., & Mack, J. 2005, ACS Data Handbook, STScI, Baltimore, version 4.0 (cited on page 20)

Peebles, P. J. E. 1980, The large-scale structure of the universe (Research supported by the National Science Foundation. Princeton, N.J., Princeton University Press, 1980. 435 p.) (cited on page 93)

Rix, H.-W. & Rieke, M. J. 1993, ApJ, 418, 123 (cited on page 49)

Roberts, W. W. 1969, ApJ, 158, 123 (cited on pages 91 and 93)

Rosolowsky, E. 2005, PASP, 117, 1403 (cited on page 18)

Salo, H. & Laurikainen, E. 2000, MNRAS, 319, 377 (cited on page 10)

Sanders, D. B., Scoville, N. Z., & Solomon, P. M. 1985, ApJ, 289, 373 (cited on pages 18 and 40)

Schaerer, D., Meynet, G., Maeder, A., & Schaller, G. 1993, A&AS, 98, 523 (cited on page 78)

Schechter, P. 1976, ApJ, 203, 297 (cited on page 110)

Scheepmaker, R. A., Haas, M. R., Gieles, M., et al. 2007, A&A, 469, 925 **(Chapter 2)** (cited on pages 56, 57, 58, 62, 73, 94, 98, 105, 109, and 147)

Scheepmaker, R. A., Lamers, H. J. G. L. M., Anders, P., & Larsen, S. S. 2009a, A&A, 494, 81 (cited on page 105)

Scheepmaker, R. A., Lamers, H. J. G. L. M., Larsen, S. S., & Anders, P. 2009b, A&A (submitted, **Chapter 5**) (cited on page 84)

Schlegel, D. J., Finkbeiner, D. P., & Davis, M. 1998, ApJ, 500, 525 (cited on pages 24, 58, 74, and 76)

Schulz, J., Fritze-v. Alvensleven, U., Möller, C. S., & Fricke, K. J. 2002, A&A, 392, 1 (cited on pages 27 and 78)

Schuster, K. F., Kramer, C., Hitschfeld, M., Garcia-Burillo, S., & Mookerjea, B. 2007, A&A, 461, 143 (cited on pages 72, 88, 89, and 96)

Shapley, H. 1918, PASP, 30, 42 (cited on page 1)

Sirianni, M., Jee, M. J., Benítez, N., et al. 2005, PASP, 117, 1049 (cited on pages 24 and 29)

Solomon, P. M., Rivolo, A. R., Barrett, J., & Yahil, A. 1987, ApJ, 319, 730 (cited on pages 9, 18, 40, and 50)

Spitzer, L. 1958, ApJ, 127, 17 (cited on pages 5 and 67)

Spitzer, L. 1987, Dynamical evolution of globular clusters, Princeton Series in Astrophysics (Princeton University Press) (cited on pages 7 and 67)

Tamburro, D., Rix, H.-W., Walter, F., et al. 2008, AJ, 136, 2872 (cited on page 92)

Tinsley, B. M. 1971, Ap&SS, 12, 394 (cited on pages 62 and 64)

Tonry, J. L., Dressler, A., Blakeslee, J. P., et al. 2001, ApJ, 546, 681 (cited on pages 62, 63, and 64)

Trumpler, R. J. 1930, Lick Observatory Bulletin, 14, 154 (cited on page 1)

Tully, R. B. 1974, ApJS, 27, 449 (cited on pages 9, 88, and 91)

Van den Bergh, S. 1998, ApJ, 507, L39 (cited on page 105)

Van den Bergh, S., Morbey, C., & Pazder, J. 1991, ApJ, 375, 594 (cited on pages 18, 47, and 51)

Weidner, C., Kroupa, P., & Larsen, S. S. 2004, MNRAS, 350, 1503 (cited on pages 118 and 119)

Whitmore, B. C. 2004, in Astronomical Society of the Pacific Conference Series, Vol. 322, The Formation and Evolution of Massive Young Star Clusters, ed. H. J. G. L. M. Lamers, L. J. Smith, & A. Nota, 419–+ (cited on page 104)

Whitmore, B. C., Gilmore, D., Leitherer, C., et al. 2005, AJ, 130, 2104 (cited on page 95)

Whitmore, B. C., Zhang, Q., Leitherer, C., et al. 1999, AJ, 118, 1551 (cited on page 72)

Williams, J. P., Blitz, L., & Stark, A. A. 1995, ApJ, 451, 252 (cited on page 18)

Xin, Y., Deng, L., de Grijs, R., Mackey, A. D., & Han, Z. 2008, MNRAS, 384, 410 (cited on page 4)

Yun, M. S., Reddy, N. A., & Condon, J. J. 2001, ApJ, 554, 803 (cited on page 72)

Zepf, S. E., Ashman, K. M., English, J., Freeman, K. C., & Sharples, R. M. 1999, AJ, 118, 752 (cited on pages 18, 19, and 51)

Zhang, Q. & Fall, S. M. 1999, ApJL, 527, L81 (cited on pages 9, 18, 40, and 110)

Zhang, Q., Fall, S. M., & Whitmore, B. C. 2001, ApJ, 561, 727 (cited on pages 72, 93, 95, and 96)

Zimmer, P., Rand, R. J., & McGraw, J. T. 2004, ApJ, 607, 285 (cited on pages 45, 90, and 116)

Appendix A

Description of the online dataset

Table A.1 shows the first 10 rows of the dataset discussed in chapter 5, available electronically at the CDS (http://cdsweb.u-strasbg.fr/). The description of the columns is as follows:

1. **ID** – The ID number of the cluster.
2. **RA** – Right ascension (J2000.0) in h:m:s.
3. **DEC** – Declination (J2000.0) in d:m:s.
4. $M_{\rm U}$ – Absolute magnitude in U_{F336W}, corrected for foreground extinction and assuming $m - M = 29.62$.
5. $\mathbf{d}M_{\rm U}$ – Error in the absolute magnitude in U_{F336W}.
6. $M_{\rm B}$ – Absolute magnitude in B_{F435W}, corrected for foreground extinction and assuming $m - M = 29.62$.
7. $\mathbf{d}M_{\rm B}$ – Error in the absolute magnitude in B_{F435W}.
8. $M_{\rm V}$ – Absolute magnitude in V_{F555W}, corrected for foreground extinction and assuming $m - M = 29.62$.
9. $\mathbf{d}M_{\rm V}$ – Error in the absolute magnitude in V_{F555W}.
10. $M_{\rm I}$ – Absolute magnitude in I_{F814W}, corrected for foreground extinction and assuming $m - M = 29.62$.
11. $\mathbf{d}M_{\rm I}$ – Error in the absolute magnitude in I_{F814W}.
12. $R_{\rm eff}$ – Effective (i.e. half-light) radius (in pc) from Scheepmaker et al. (2007), measured on the *HST*/*ACS* B_{F435W} image assuming an EFF15 (Elson et al. 1987) surface brightness profile.
13. **log(age$_{\rm min}$/yr)** – Logarithm of the age (in yr), lower limit.
14. **log(age/yr)** – Logarithm of the age (in yr).
15. **log(age$_{\rm max}$/yr)** – Logarithm of the age (in yr), upper limit.

16. **log(**$M_{\rm min}/M_{\odot}$**)** – Logarithm of the mass (in $M_{\odot}$), lower limit.
17. **log(**$M/M_{\odot}$**)** – Logarithm of the mass (in $M_{\odot}$).
18. **log(**$M_{\rm max}/M_{\odot}$**)** – Logarithm of the mass (in $M_{\odot}$), upper limit.
19. **E(B−V)**$_{\rm min}$ – Extinction E(B−V), lower limit.
20. **E(B−V)** – Extinction E(B−V).
21. **E(B−V)**$_{\rm max}$ – Extinction E(B−V), upper limit.

Table A.1: First 10 rows of the electronic dataset.

1	2	3	4	5	6	7	8	9	10	11
ID	RA	DEC	M_U	dM_U	M_B	dM_B	M_V	dM_V	M_I	dM_I
103696	13:30:00.41	47:09:06.49	-8.802	0.050	-8.303	0.004	-8.443	0.005	-8.986	0.005
103942	13:29:58.63	47:09:10.21	-8.542	0.080	-6.900	0.023	-6.939	0.027	-7.543	0.020
104103	13:30:01.36	47:09:12.01	-7.902	0.110	-7.088	0.013	-7.168	0.018	-7.570	0.022
104203	13:29:56.61	47:09:12.78	-8.012	0.100	-6.333	0.018	-6.438	0.023	-7.494	0.018
104269	13:29:59.55	47:09:13.15	-7.852	0.120	-6.552	0.018	-6.682	0.020	-7.034	0.026
104331	13:29:58.76	47:09:13.52	-10.572	0.030	-9.015	0.009	-8.880	0.010	-8.865	0.014
104359	13:29:59.03	47:09:13.90	-9.442	0.050	-8.029	0.010	-7.961	0.013	-8.154	0.016
104466	13:30:01.31	47:09:12.86	-9.072	0.040	-8.727	0.004	-8.851	0.004	-9.233	0.005
104515	13:29:58.46	47:09:15.08	-8.932	0.060	-7.218	0.037	-7.184	0.040	-7.327	0.044
104582	13:29:59.07	47:09:15.93	-8.012	0.120	-6.233	0.057	-6.136	0.063	-7.058	0.037
⋮	⋮	⋮	⋮	⋮	⋮	⋮	⋮	⋮	⋮	⋮

Table A.1 continued...

12	13	14	15	16	17	18	19	20	21
$R_{\rm eff}$ (pc)	— log(age/yr) —			— log($M/M_\odot$) —			— E(B−V) —		
4.04	6.73	7.81	8.10	3.28	4.43	4.56	0.00	0.05	0.30
0.58	7.00	7.05	7.06	3.29	3.33	3.35	0.00	0.00	0.00
0.81	6.60	6.96	7.61	2.74	2.99	3.76	0.00	0.00	0.20
1.25	6.92	6.94	6.97	3.00	3.03	3.08	0.00	0.00	0.00
0.70	6.60	6.65	6.71	2.65	2.78	2.84	0.00	0.10	0.15
2.29	6.46	6.60	6.61	3.27	3.55	3.63	0.00	0.00	0.05
0.77	6.59	6.63	6.65	3.09	3.16	3.18	0.00	0.00	0.00
7.30	6.74	7.20	8.32	3.41	4.08	4.85	0.00	0.15	0.25
1.50	6.48	6.61	6.62	2.64	2.86	3.03	0.00	0.00	0.10
3.69	6.96	7.00	7.03	2.98	3.03	3.06	0.00	0.00	0.00
⋮	⋮	⋮	⋮	⋮	⋮	⋮	⋮	⋮	⋮